

## REVIEW

View Article Online  
View Journal | View Issue



Cite this: *Nanoscale Horiz.*, 2021, 6, 939

## ABO<sub>3</sub> multiferroic perovskite materials for memristive memory and neuromorphic computing

Bai Sun,<sup>†\*ab</sup> Guangdong Zhou,<sup>†c</sup> Linfeng Sun,<sup>†d</sup> Hongbin Zhao,<sup>e</sup> Yuanzheng Chen,<sup>†a</sup> Feng Yang,<sup>b</sup> Yong Zhao<sup>ab</sup> and Qunliang Song<sup>†\*c</sup>

The unique electron spin, transfer, polarization and magnetoelectric coupling characteristics of ABO<sub>3</sub> multiferroic perovskite materials make them promising candidates for application in multifunctional nanoelectronic devices. Reversible ferroelectric polarization, controllable defect concentration and domain wall movement originated from the ABO<sub>3</sub> multiferroic perovskite materials promotes its memristive effect, which further highlights data storage, information processing and neuromorphic computing in diverse artificial intelligence applications. In particular, ion doping, electrode selection, and interface modulation have been demonstrated in ABO<sub>3</sub>-based memristive devices for ultrahigh data storage, ultrafast information processing, and efficient neuromorphic computing. These approaches presented today including controlling the dopant in the active layer, altering the oxygen vacancy distribution, modulating the diffusion depth of ions, and constructing the interface-dependent band structure were believed to be efficient methods for obtaining unique resistive switching (RS) behavior for various applications. In this review, internal physical dynamics, preparation technologies, and modulation methods are systemically examined as well as the progress, challenges, and possible solutions are proposed for next generation emerging ABO<sub>3</sub>-based memristive application in artificial intelligence.

Received 28th May 2021,  
Accepted 22nd September 2021

DOI: 10.1039/d1nh00292a

rsc.li/nanoscale-horizons

<sup>a</sup> School of Physical Science and Technology, Key Laboratory of Advanced Technology of Materials (Ministry of Education of China), Southwest Jiaotong University, Chengdu, Sichuan 610031, China. E-mail: bsun@swjtu.edu.cn

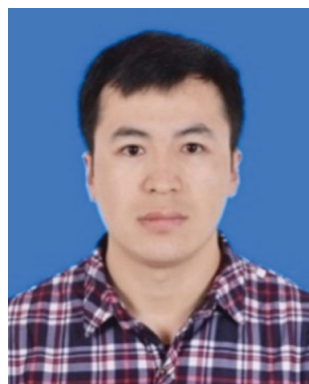
<sup>b</sup> Superconductivity and New Energy R&D Center, Southwest Jiaotong University, Chengdu, Sichuan 610031, China

<sup>c</sup> School of Artificial Intelligence and School of Materials and Energy, Southwest University, Chongqing 400715, China. E-mail: qlsong@swu.edu.cn

<sup>d</sup> Centre for Quantum Physics, Key Laboratory of Advanced Optoelectronic Quantum Architecture and Measurement (MOE), School of Physics, Beijing Institute of Technology, Beijing 100081, China

<sup>e</sup> State Key Laboratory of Advanced Materials for Smart Sensing, General Research Institute for Nonferrous Metals, Beijing, 100088, China

<sup>†</sup> Authors equally contribute to this work.



Bai Sun

Dr Bai Sun received his PhD degree from the Faculty of Materials and Energy from Southwest University (China) in 2015, and conducted postdoctoral research in the University of Waterloo (Canada). Currently, he is an associate professor at Southwest Jiaotong University. His research interests include multifunctional application of nanomaterials, physical devices (memristors and multiferroic devices), the preparation of photocatalytic materials

and exploration of new energy storage materials. Dr Sun has published more than 100 peer-reviewed papers.



Guangdong Zhou

Dr Guangdong Zhou received his PhD degree from the Faculty of Materials and Energy of Southwest University (China) in 2018. He conducted his postdoctoral research in Southwest University during July 2018 to July 2020. His research focuses on the physical mechanism of memristors and memristor-based functions including the memory logics, displays and synapses. His memristor related research is supported by the Postdoctoral Program for Innovative Talent Support of Chongqing. During the past 10 years, he

has published more than 80 peer-reviewed papers.

# 1. Introduction

The RS phenomenon was first observed in various binary metal oxides in the 1960s,<sup>1</sup> but the physical mechanism was not discovered. In 1971, Chua proposed four fundamental passive circuit elements described by the relationship among four basic circuit variables: voltage ( $v$ ), current ( $i$ ), charge ( $q$ ), and magnetic flux ( $\phi$ ),<sup>2</sup> as shown in Fig. 1. Analogous with a resistor ( $R$ ), capacitor ( $C$ ), and inductor ( $L$ ), the existence of a memristor ( $M$ ) was symmetrically predicted based on the relationship between  $q$  and  $\phi$ .<sup>2</sup> However, the experimental realization of a memristor remained elusive until 2008, when the Hewlett-Packard (HP) laboratory reported that a memristor can be achieved using the RS effect in the  $\text{TiO}_2$  films sandwiched between two Pt electrodes,<sup>3</sup> which led to new research interests in the materials science, information technology and physical science.<sup>4–9</sup> Subsequently, it was recognized that a pinched (or zero-crossing) hysteretic

current–voltage ( $I$ – $V$ ) curve can represent the memristive effect.<sup>10</sup> Currently, a memristor demonstrates the ability of high-density information storage, ultra-fast logic operations, simulation of nerve synapses, efficient neuromorphic computing, *etc.* Therefore, the memristive devices present great potential for application in the fields of multifunctional devices, electronics, neurology, biomedicine, computer science, and artificial intelligence.

Resistance random access memory (RRAM) based on the memristive effect is considered to be the most promising next-generation data storage technology because it can break through the physical limitations of traditional memory devices.<sup>11–15</sup> The RRAM can achieve higher storage density, smaller storage unit volume, lower power consumption, faster reading and writing speed and other advantages compared with other existing memories. In particular, the memristor unit can ideally simulate the function of a biological synapse, as shown in Fig. 2. The top electrode (TE) and the bottom electrode (BE)



**Linfeng Sun**

*Dr Linfeng Sun is currently a professor in the School of Physics, Beijing Institute of Technology (China). He received his doctoral degree from the Department of Physics and Applied Physics of Nanyang Technological University (Singapore). His research interests focus on the device physics design, characterization, and applications, including 2D material-based transistors, photo-detectors, volatile and nonvolatile memory, synaptic electronics, and neuromorphic computing.*



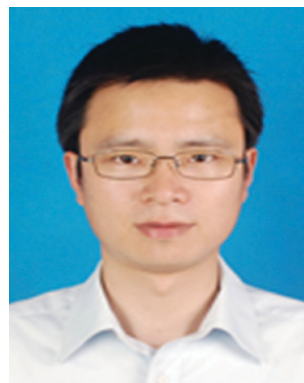
**Hongbin Zhao**

*Dr Hongbin Zhao is a materials researcher of the State Key Laboratory of Advanced Materials for Smart Sensing; he received his doctoral degree from the General Research Institute for Nonferrous Metals (China) in 2014. In recent years, his research interests mainly focus on materials preparation and device fabrication of memristors and novel sensing materials and devices. During the last 10 years, his research has been supported by the Ministry of Science and Technology of China, National Natural Science Foundation of China, *etc.* He has published over 70 peer-reviewed papers, and holds 15 authorized patents.*



**Yuanzheng Chen**

*Dr Yuanzheng Chen received his PhD degree from the State Key Lab of Superhard Materials of Jilin University (China) in 2014. Then he joined Southwest Jiaotong University (China) as an associate professor. Recently, he moved to Beijing Computational Science Research Center for postdoctoral research, as well as National University of Singapore as a visiting scholar. His research focuses on functional device design and the discovery of new chemical and physical properties using density functional theory (DFT) calculations.*



**Feng Yang**

*Dr Feng Yang received his Master's degree in Physics and Chemistry of Materials from Yanshan University in 2005 (China). Then, he entered the Department of Polymer Science & Engineering & State Key Laboratory of Silicon Materials at Zhejiang University and completed his PhD degree (2008). Afterwards, he became a Lecturer (2008–2011) and Associate Professor (since 2011) at Southwest Jiaotong University. His current research interests include surface photovoltage, photo-electronic, memristor, and resistive switching properties of metal oxide nanomaterials.*

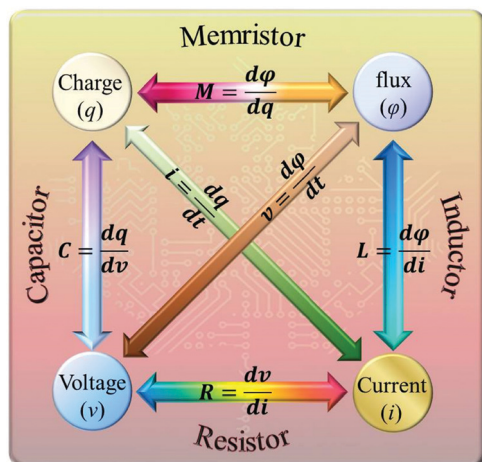


Fig. 1 The relationship among four basic circuit variables: voltage ( $v$ ), current ( $i$ ), charge ( $q$ ), and magnetic flux ( $\phi$ ).

of the memristive unit are just like the pre- and post-synaptic neurons, the carriers (ions or electrons) in the active material are like neurotransmitters, and the flow of electrical signals in the memristor unit is similar to the transmission of biological signals between neurons. Thus, the cross bar array based on the RRAM device structure could be beneficial to the integration of synaptic devices for complicated neuromorphic computing functions because the RRAM shares the same dynamics with the synapse.<sup>16–18</sup> For these reasons, the neuromorphic computing realized by memristive devices for artificial intelligence applications has attracted the attention of many researchers.<sup>19–25</sup> The hardware realization of this biological synapse function is also an important factor in promoting the development of robots. Therefore, the study of the memristive effect has become a current research focus in materials science, electronics, biology, computer science, *etc.*<sup>26–30</sup>

Compared with other electronic devices, memristors have obvious advantages in material selection and device structure.<sup>31–35</sup>

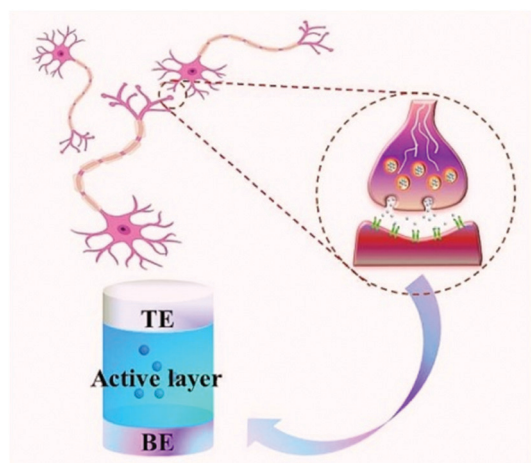


Fig. 2 The memristor can simulate the function of biological synapses because the sandwich structure of the memristor unit is similar to nerve synapses.

In the past ten years, the research on memristive functional materials has made great progress. It has been found that the materials like metal oxide semiconductors, insulators or polymers and biomaterials show a good memristive effect.<sup>36–40</sup> In particular, it has also been proved that many perovskite materials have excellent RS effects.<sup>4–9</sup> This diversified material selection not only speeds up the research process of the memristive device, but also effectively reduces the manufacturing cost of the device. In this review, we mainly discuss the research progress of the RS effect based on  $\text{ABO}_3$ -type multiferroic perovskite materials, the fabrication method of RS devices, the approaches of building a neural network, and the potential applications of  $\text{ABO}_3$ -type multiferroic perovskite materials in the hardware artificial intelligence systems. The research progress from  $\text{ABO}_3$ -type multiferroic perovskite materials to artificial intelligence is shown in Fig. 3. Finally, we point out the developmental trend and the advanced potential applications of  $\text{ABO}_3$ -type multiferroic perovskite materials based on the RS effect.

## 2. $\text{ABO}_3$ multiferroic perovskite materials

The multiferroic effect is a phenomenon in which a material with a single or composite-phase exhibits at least two ferroelectric parameters (ferromagnetism, ferroelectricity or ferroelasticity) under certain conditions.<sup>41,42</sup> Fig. 4a clearly shows the conceptual relationship among multiferroic/ferromagnetic/ferroelectric/ferroelastic properties. Based on the applied considerations, current research mainly focuses on multiferroic materials that simultaneously exhibit both magnetism and ferroelectricity. This type of multiferroic material is also called magnetoelectric material,<sup>43–45</sup> which has attracted the attention of researchers from the fields of physical and materials science, and it is expected to develop multistate memory devices due to the magnetoelectric coupling effect.<sup>46–48</sup> Fig. 4b shows the conceptual relationship among magnetoelectric coupling/ferromagnetism/ferroelectricity, which clearly displays their concept range and the corresponding hysteresis curves. Among the discovered single-phase multiferroic/magnetoelectric materials, it is generally considered that the most practically promising multiferroic materials are  $\text{TbMnO}_3$  and  $\text{BiFeO}_3$ .<sup>49,50</sup> Besides, the development of composite multiferroic materials has played a good supplement to the application of multiferroic materials.<sup>51,52</sup> It is well known that material composite technology can combine a variety of nanoparticles of materials with different properties through physical or chemical methods. It is a commonly used material synthesis and processing approach. Therefore, the material composite technology also shows strong effectiveness in the preparation of composite multiferroic materials.

In fact, the concept of multiferroic materials was proposed as early as 1994. Subsequently, several new physical phenomena were triggered due to the special physical properties of multiferroic materials. For example, the magnetoelectric coupling effect can induce a new ferroelectric polarization in a magnetic field or a new ferromagnetic magnetization in an



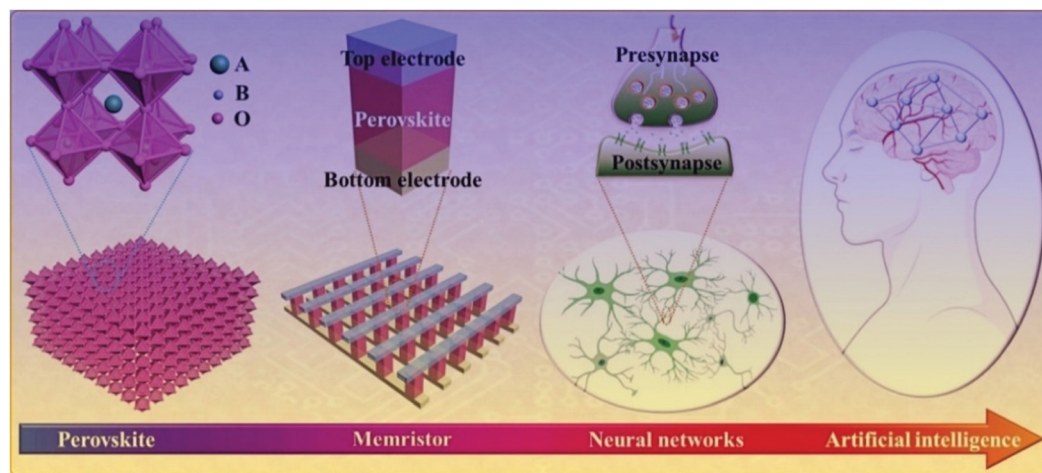


Fig. 3 The research progress from  $\text{ABO}_3$ -type multiferroic perovskite materials to the hardware realization of artificial intelligence.

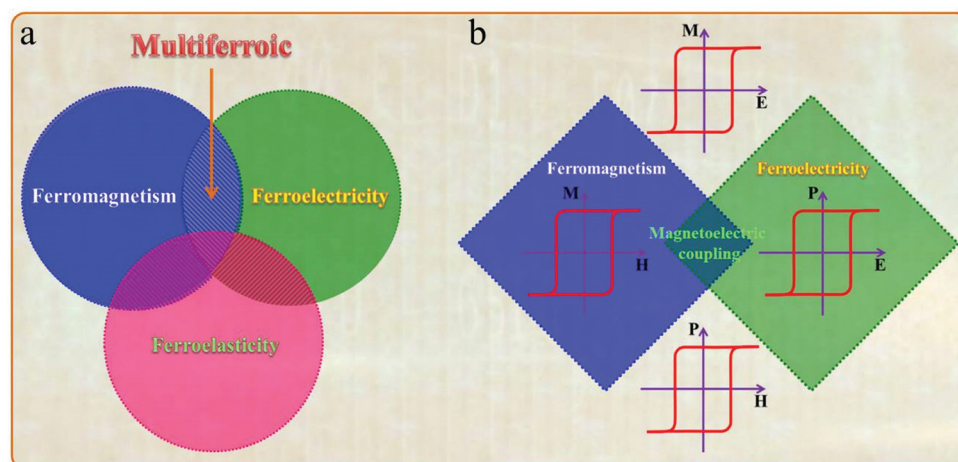


Fig. 4 (a) The relationship among multiferroic/ferromagnetic/ferroelectric/ferroelastic materials clearly shows their concept range. (b) The relationship among magnetolectric coupling/ferromagnetism/ferroelectricity clearly shows their concept range and the corresponding hysteresis curves.

electric field. At present, multiferroic materials have become a research focus in the field of materials science. It should be noted that N. A. Spaldin and R. Ramesh have summarized the multiferroic family tree based on recent development of multiferroic materials,<sup>43</sup> as shown in Fig. 5. This figure gives us an intuitive understanding of the evolution of multiferroic materials, including single-phase and composite multiferroic materials. It can be seen that the four roots of the multiferroic family tree combine and interweave in various complicated ways to organize the branches. The most obvious strategies for engineering new multiferroics are to combine one magnetic and one ferroelectric mechanism from these roots to make new branches in this tree. With the continuous discovery of new multiferroic materials, the multiferroic family tree will also grow new branches, and the application of multiferroic materials will also make rapid progress. It is expected to realize a new generation of multifunctional devices, such as new magnetoelectric sensors, spintronic devices, multistate memory devices, *etc.*<sup>53–62</sup>

Among the well-known multiferroic materials,  $\text{BiFeO}_3$  and  $\text{TbMnO}_3$  remain as the most seriously arguable.<sup>63,64</sup> The room temperature crystal structure of  $\text{BiFeO}_3$  is shown in Fig. 6. The displacement of these cations corresponds to the distortion of the ferroelectric phase, and the tilt of the octahedron is usually called the distortion rotation of the antiferromagnetic state. When the rotation direction of the adjacent oxygen octahedra along the crystal direction is reversed, it means the reverse of the antiferroelastic displacement and deformation, and the residual magnetization moment deviates from the  $b$ -axis direction at this time.<sup>65</sup> In fact, the change of the bond length plays a vital role in the stability of the ferroelectric phase. Based on the changeable structure of  $\text{BiFeO}_3$ , it can exhibit many special physical properties.

In particular,  $\text{BiFeO}_3$  as a typical  $\text{ABO}_3$  type multiferroic perovskite material has been widely studied with respect to photovoltaic, photoelectric, and magnetoelectric coupling effects,<sup>66,67</sup> as shown in Fig. 7. Such multiple properties make  $\text{BiFeO}_3$  a potential candidate to realize multifunctional devices.



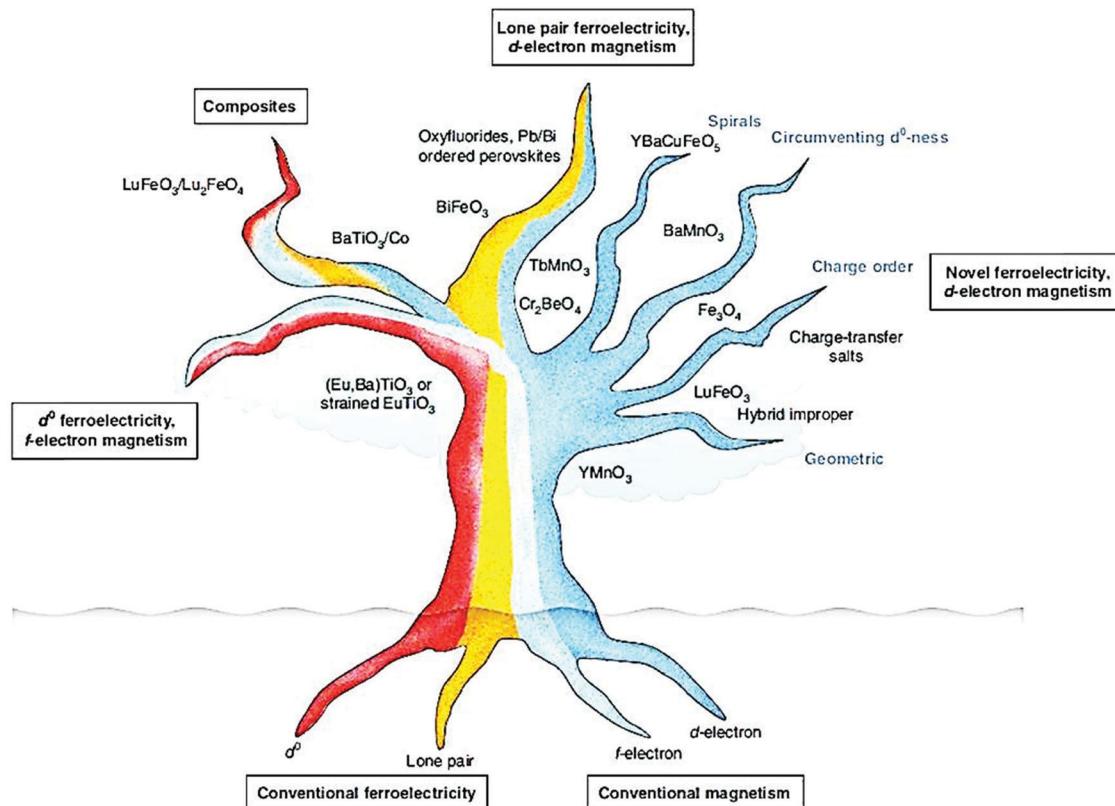


Fig. 5 The schematic diagram of the multiferroic family tree, which shows the mechanism of different types of multiferroic materials due to different combinations. Reproduced with permission.<sup>43</sup> Copyright 2019, Nature Publishing Group.

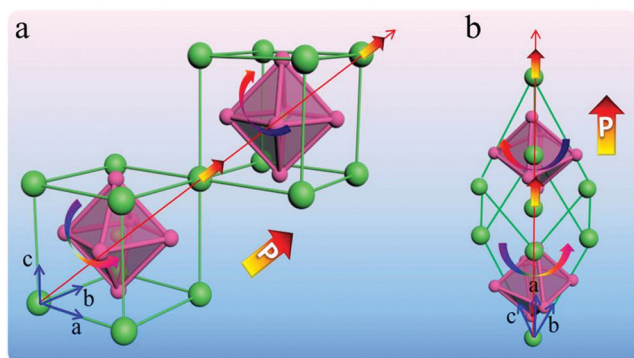


Fig. 6 (a) Pseudocubic unit cell including one unit cell. (b) Rhombohedral unit cell including two unit cells.

$\text{BiFeO}_3$  has a typical tripartite structure at room temperature, and its space group belongs to  $R3c$ . The ferroelectricity of the  $\text{BiFeO}_3$  crystal is caused by the lone pair of electrons from the Bi ion. At the same time,  $\text{BiFeO}_3$  has a G-type antiferromagnetic and spatially modulated magnetic structure. At present, there are many methods for preparing  $\text{BiFeO}_3$ , such as the sintering method, sol-gel method, hydrothermal method, etc.<sup>66,67</sup>

In addition, other perovskite materials with multiferroic properties have attracted the attention of many researchers.<sup>68–70</sup> For example, the multiferroic  $\text{TbMnO}_3$  has an orthogonal perovskite structure, which not only shows good multiferroicity, but also

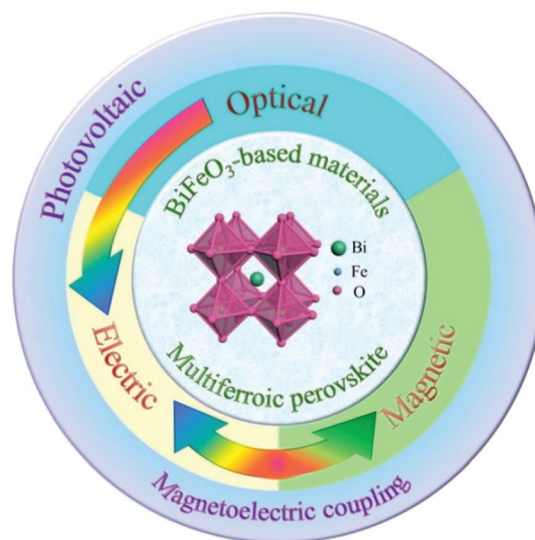


Fig. 7 The multiferroic  $\text{BiFeO}_3$  single crystal material has good photovoltaic, ferroelectric and magnetic properties.

excellent optical properties.<sup>43</sup> Thus,  $\text{TbMnO}_3$  is also a multifunctional material with ferroelectric, ferromagnetic and optical properties. Next, we will discuss the research progress of the RS effect and potential applications in artificial intelligence systems based on these  $\text{ABO}_3$ -type multiferroic perovskite materials.

### 3. RS effect of $\text{ABO}_3$ multiferroic perovskite materials

#### 3.1 Research progress

Utilizing the ferroelectric polarization to modify the electron transfer in an  $\text{ABO}_3$ -type function layer, a self-rectifying RS memory behaviour, which was desired for the ultra-large memristor array integration because the sneak current could be suppressed by this self-rectifying effect, was firstly observed in a  $\text{BiFeO}_3$ -based device.<sup>71</sup> During the experimental process, a highly oriented ferroelectric  $\text{BiFeO}_3$  nano-islands array was prepared

using a thin anodic aluminum oxide (AAO) nano-template on single-crystal  $\text{SrRuO}_3/\text{SrTiO}_3$  (100) substrates by the pulsed laser deposition (PLD) technique. The preparation process is shown in Fig. 8a. In order to deeply explore the polarization-related charge conduction process of  $\text{BiFeO}_3$  nano-islands, the periodic current-voltage ( $I$ - $V$ ) characteristics by conductive atomic force microscopy (CAFM) during piezo-response force microscopy (PFM) on  $\text{BiFeO}_3/\text{SrRuO}_3/\text{SrTiO}_3$  nano-islands were simultaneously measured. The schematic of the experimental measurement is shown in the inset of Fig. 8b. In the process of testing, an atomic force microscopy (AFM) tip coated with

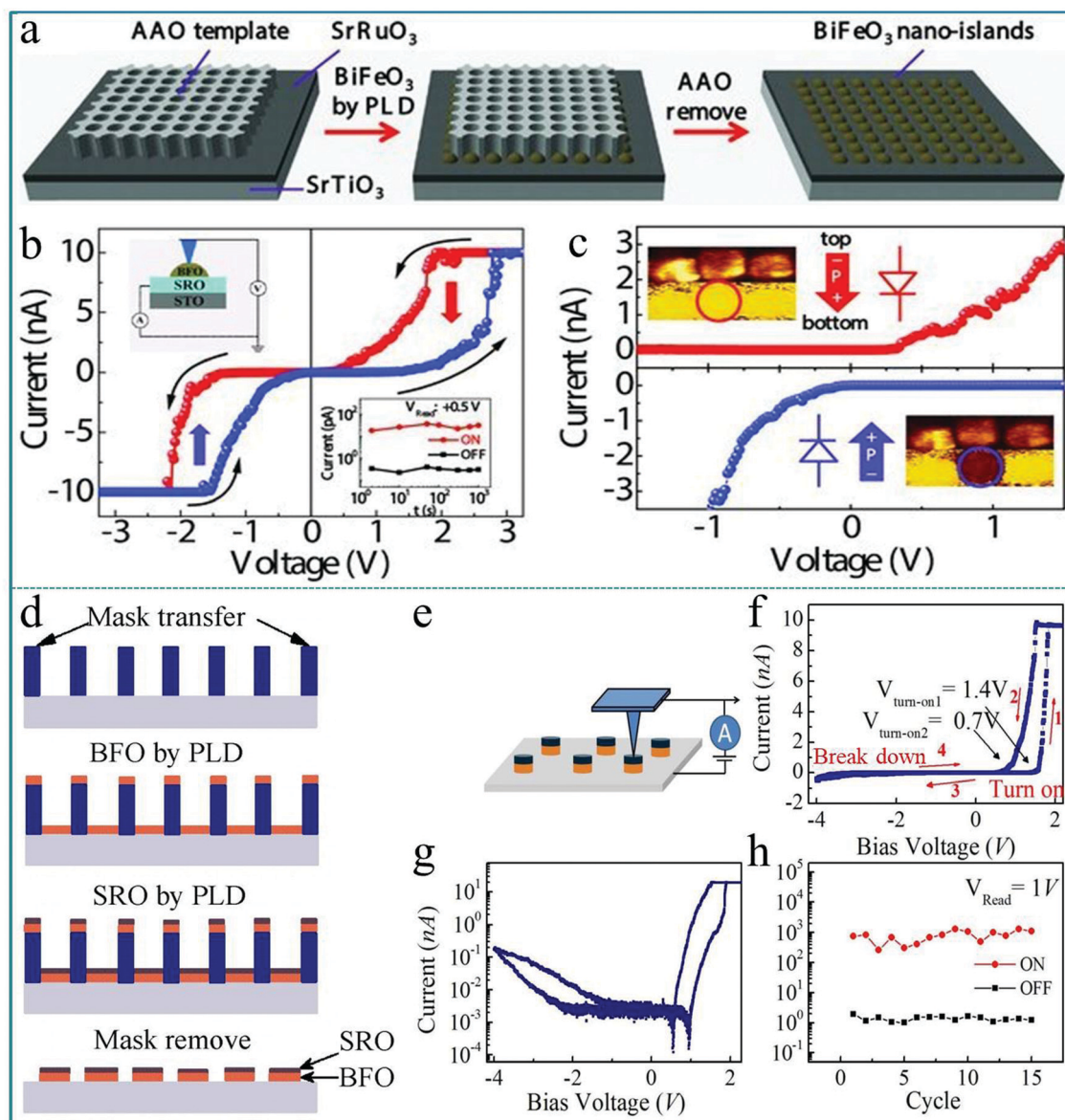


**Fig. 8** (a) Fabrication process of the  $\text{BiFeO}_3$  nano-islands array; (b)  $I$ - $V$  curves of the  $\text{Pt}/\text{BiFeO}_3/\text{SrRuO}_3/\text{SrTiO}_3$  device demonstrate the switchable ferroelectric diode effect in the voltage range of  $\pm 3.5$  V; (c)  $I$ - $V$  curves measured on a single  $\text{BiFeO}_3$  nano-island at down-polarization (positive-forward diode) and up-polarization (negative-forward diode) states below the coercive voltage, respectively. Panels a–c reproduced with permission.<sup>71</sup> Copyright 2013, Wiley-VCH. (d) Schematic flow chart illustrating the fabrication procedure of the  $\text{BiFeO}_3/\text{SrRuO}_3$  nanocapacitor arrays on a Nb-doped  $\text{SrTiO}_3$  substrate. (e) The schematic diagram of the device measurement. (f) Local  $I$ - $V$  curves show both a large rectification and a RS behavior at a maximum bias voltage of 4.0 V. (g) The replotted  $I$ - $V$  curve in a semi-logarithmic form. (h) The endurance test with 15 cycles under a readout voltage of 1.0 V. Panels d–h reproduced with permission.<sup>72</sup> Copyright 2015, Nature Publishing Group.

conductive Pt/Ir acts as the top electrode of the device and SrRuO<sub>3</sub> acts directly as the bottom electrode. Thus, this structure constitutes a typical sandwich device. The  $I$ - $V$  measurements were carried out repeatedly by sweeping the applied voltage in the sequence of  $0 \rightarrow 3.5 \text{ V} \rightarrow -3.5 \text{ V} \rightarrow 0 \text{ V}$ . One can clearly observe a large hysteresis behavior in the  $I$ - $V$  curve in Fig. 8b, reflecting the existence of a RS effect. Besides, the comparison between PFM amplitude/phase images and the obtained  $I$ - $V$  curve in the low voltage region of  $\pm 1.5 \text{ V}$  below transition voltages confirmed that the ferroelectric polarization reversal induced transitions of the forward-direction, and thus the down- and up-polarizations were accompanied by positive- and negative-forward, respectively, as shown in Fig. 8c. Taking into account the self-rectifying RS effect, low SET/RESET current and nanoscale cell size, the BiFeO<sub>3</sub>-based memristor exhibits great potential application in the neuromorphic computing system with low power consumption, reliable computing accuracy and considerable hashrate.

In previous reports, the preparation of nanomaterials using AAO nano-templates has shown many advantages, such as uniform distribution, good orientation, and controllable size and density.<sup>73–76</sup> The AAO template can usually be prepared by an electrochemical corrosion process, which has the advantage of being simple and easy to implement, and size of the hole diameter can be adjusted according to different experimental requirements. Currently, AAO templates have a wide range of applications in nano-assembly systems, including the assembly of quantum dots, nanowires, nanotubes, and “coaxial cable type” layered nanowire materials. Their use not only simplifies the preparation process of nanomaterials, but also provides good feasibility for industrialized production.

The method of preparing nanodevices using AAO templates has been adopted by many researchers. Lina Zhao *et al.* prepared well-ordered multiferroic BiFeO<sub>3</sub> nanocapacitor arrays on conductive Nb-doped SrTiO<sub>3</sub> (Nb-STO) substrates by a combination of PLD method and AAO template.<sup>72</sup> After the deposition was completed, the removal of the AAO template depends on its ability to be easily dissolved in acidic solutions. Then, an apparent current-rectification effect and RS behavior in the sandwich structure cells consisting of BiFeO<sub>3</sub>/SrRuO<sub>3</sub> (BFO/SRO) heterostructure nanodots have been observed. The RS device was obtained after four production steps, as illustrated in Fig. 8d. To further examine the RS memory behavior, the  $I$ - $V$  characteristics of a single BiFeO<sub>3</sub> nanodot were tested by using the CAFM tip as the top electrode and Nb-STO as the bottom electrode of the device. The schematic structure of the device is depicted in Fig. 8e. A hysteresis behavior in the  $I$ - $V$  curve can be observed in Fig. 8f, indicating an apparent RS effect with an obvious rectification property. Fig. 8g shows the corresponding non-zero-crossing  $I$ - $V$  curve based on logarithmic coordinates, indicating that a polarized internal electric field caused by the ferroelectric polarization effect was generated under an external electric field. Finally, to examine the stability of the RS behavior, the  $I$ - $V$  sweeps with 15 cycles under a reading bias of  $4.0 \text{ V}$  were performed. The ON/OFF currents at a reading voltage of  $1.0 \text{ V}$  are plotted in Fig. 8h, showing that the device has almost no

attenuation after 15 successive cycles. These experimental results indicate that the multiferroic BiFeO<sub>3</sub> nanodot arrays offer potential possibilities to utilize these simple sandwich structure arrays in high-density nonvolatile RRAM memories and other multifunctional nano-electronic devices.

Similar to the preparation method of the device in the above works, Zengxing Lu *et al.* prepared well-ordered and high-density isolated Pt nano electrode arrays on BiFeO<sub>3</sub> (BFO) ultrathin films grown on a SrTiO<sub>3</sub> substrate using the AAO nano-template, and observed a good ferroelectric RS characteristic.<sup>77</sup> The fabrication processes of the Pt/BiFeO<sub>3</sub>/SrRuO<sub>3</sub> device are shown in Fig. 9a. The nanocapacitor arrays are well-ordered, and the diameter of Pt nano electrodes observed from Fig. 9b is  $\sim 60 \text{ nm}$ . The thickness of Pt nano electrodes is  $\sim 8 \text{ nm}$  (Fig. 9c). Thus, the volume of each device unit is very small. The  $I$ - $V$  hysteresis loops were measured using the sweeping applied voltage with a sequence of  $0 \rightarrow 6.0 \text{ V} \rightarrow 0 \rightarrow -6.0 \text{ V} \rightarrow 0$ , as shown in Fig. 9d, showing a stable RS performance. It should be noted that there is a relatively small output current. This kind of device can be used in electronic devices requiring a small current. The corresponding  $I$ - $V$  curve in a logarithmic form is shown in the inset of Fig. 9d, in which we can see that this  $I$ - $V$  curve is almost completely symmetrical even though the structure of the device is asymmetrical. In particular, this device has a very large resistance window of approximately  $10^3$ . This large resistance window provides the possibility for high-density information storage. Fig. 9e shows that the ON/OFF current values only slightly deviate with the increasing number of cycles, indicating the good reproducibility of the RS behavior in the Pt/BiFeO<sub>3</sub>/SrRuO<sub>3</sub> device. These results suggest that the BiFeO<sub>3</sub> ultrathin film-based nanocapacitors are promising candidates for non-volatile ferroelectric RS memories with a small output current and ultrahigh integrated density. In addition, the use of AAO templates provides a reliable way for the preparation of high-density integrated RS memory devices. Furthermore, this preparation method using AAO template associated pulsed laser deposition is simple and easy to implement during the actual experiment, and thus it is easy for large-scale industrial production.

Furthermore, Lei Feng *et al.* investigated the ferroelectric RS effects of the Au/BiFeO<sub>3</sub>/La<sub>0.6</sub>Sr<sub>0.4</sub>MnO<sub>3</sub> (Au/BFO/LSMO) multiferroic heterostructure on a SrTiO<sub>3</sub> (001) single crystal substrate,<sup>78</sup> in which the Au top electrode with a diameter of  $0.3 \text{ mm}$  was sputtered on the BiFeO<sub>3</sub> thin film, as shown in Fig. 9f. For testing of the RS properties, the traditional current perpendicular to the film plane was employed, and the forward bias was defined as a positive voltage applied to the device unit. The cross section STEM-HAADF image of the interface of the BiFeO<sub>3</sub>/La<sub>0.6</sub>Sr<sub>0.4</sub>MnO<sub>3</sub> heterostructure by scanning transmission electron microscopy (STEM) using a high angle annular dark field (HAADF) detector is illustrated in Fig. 9g, in which the position of the BiFeO<sub>3</sub>/La<sub>0.6</sub>Sr<sub>0.4</sub>MnO<sub>3</sub> interface is labeled by a green line. The room temperature ferroelectric hysteresis loop ( $P$ - $V$ ) at  $5 \text{ kHz}$  is shown in Fig. 9h. It exhibits a large coercive force and residual ferroelectric polarization, and no leakage current is observed. To study the RS behaviors of the



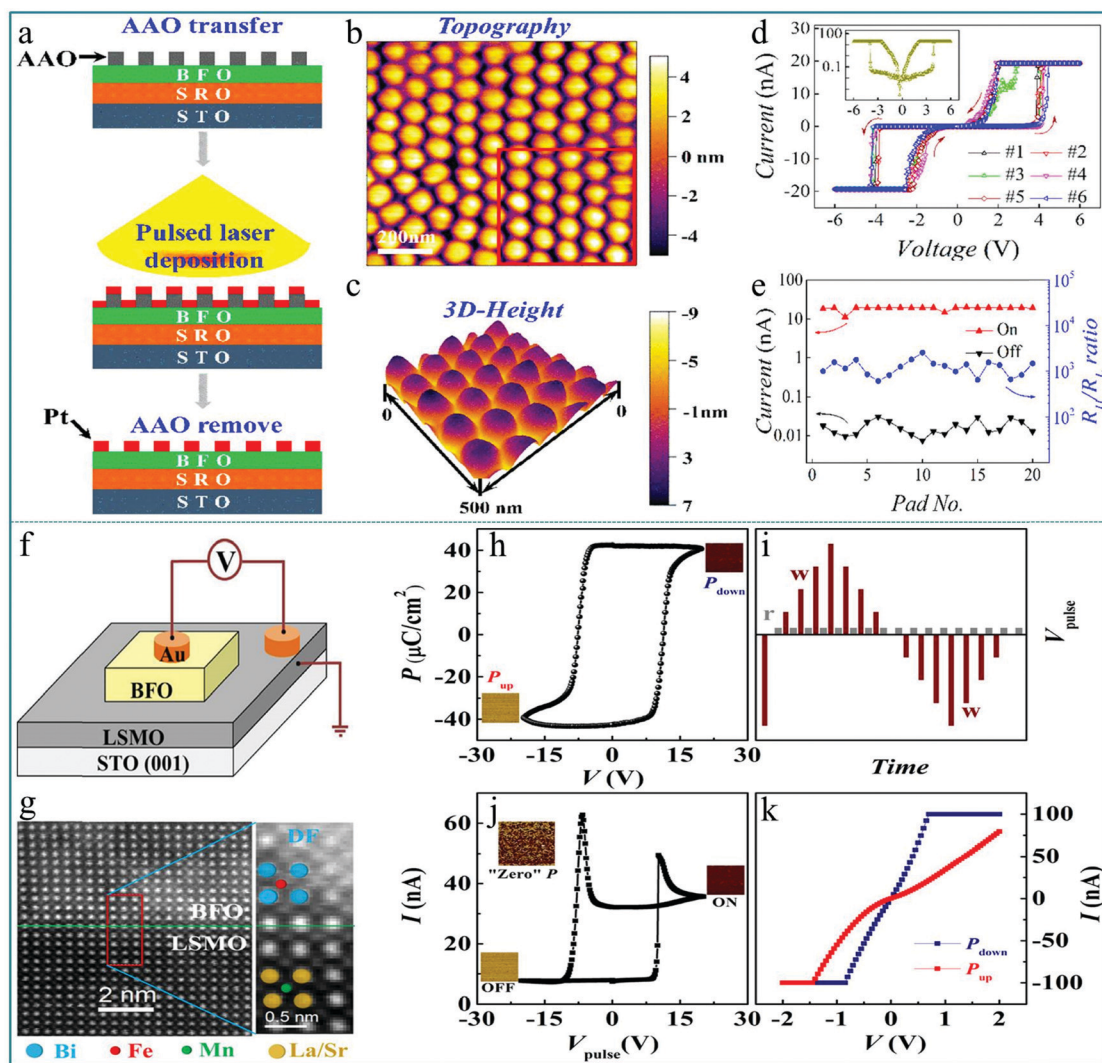


**Fig. 9** (a) Schematic flowchart illustrating the procedures of fabricating the Pt/BiFeO<sub>3</sub>/SrRuO<sub>3</sub> nanocapacitor arrays on a SrTiO<sub>3</sub> substrate; (b) 2D and (c) 3D topography images of the Pt nanodots; (d) *I*–*V* hysteresis loops measured for multiple cycles, and the inset shows the *I*–*V* hysteresis loop plotted on a semilogarithmic scale; (e) RS parameters measured for different nano capacitors. Panels a–e reproduced with permission.<sup>77</sup> Copyright 2016, American Chemical Society. (f) Schematic illustration of the measurement configuration of the sample; (g) typical STEM-HAADF image of the BiFeO<sub>3</sub>/La<sub>0.6</sub>Sr<sub>0.4</sub>MnO<sub>3</sub> interface showing the good epitaxial properties of the heterostructure; (h) remnant *P*–*V* hysteresis loop of the heterostructure with *f* = 5 kHz at room temperature; (i) schematic pulse train for the *I*–*V* pulse loop; (j) steady-state current measured as a function of 100 μs writing pulses using the pulse train shown in part (i); the corresponding domain structures measured by the out of plane piezoelectric AFM are shown in the middle right, bottom left, and top left insets for the LRS (ON), HRS (OFF), and zero polarized states, respectively; (k) *I*–*V* curves measured after applying *V*<sub>p</sub> = ±20 V. Panels f–k reproduced with permission.<sup>78</sup> Copyright 2015, American Chemical Society.

heterostructure, the *I*–*V* pulse is measured with the testing pulses composed of a series of write-pulses (0 V → 20.0 V → –20.0 V → 0 V) with different amplitudes and a read-pulse (0.3 V) following each write-pulse as shown in Fig. 9i. With the heterostructure prepolarized upward by a pulse (amplitude: –20.0 V), the nonvolatile RS phenomenon of the heterostructure is demonstrated by the clear hysteretic *I*–*V* curve (Fig. 9j). To investigate the origin of the low resistance state (LRS) or “ON” state and the high resistance state (HRS) or “OFF” state, the *I*–*V* curves at the fully downward and upward polarization states were further measured, as shown in Fig. 9k, in which a standard bipolar RS behavior with a clear HRS (red line) and

LRS (dark blue line) was observed, which is relative to the upward polarization and downward polarization of the device. In a word, the above findings are helpful for us to understand the effects of interfaces and the ferromagnetism of ferroelectric domain walls (DWs) in multiferroic heterostructures on the nonvolatile RS characteristics. This interface coupling is directly related to the electron spin coupling by ferroelectric polarization. Therefore, this work may give a possibility for combining the RS device with spintronics. In fact, many devices based on the spin of electrons and molecules have been developed, such as spin diodes and spin photovoltaic devices. They have completely new device functions that are extremely

different from those of traditional electronic devices. Such devices might have great potential applications in spintronics.

It is well known that the ferroelectric properties of ferroelectric materials originate from the spontaneous polarization of electrons in the ferroelectric domains,<sup>79</sup> and the spontaneous magnetization of electrons in the magnetic domains makes the material exhibit magnetism.<sup>80</sup> Therefore, the macroscopic performance of multiferroic materials comes from the rotation or movement of microscopic ferroelectric domains and magnetic domains. In addition, molecular electronics uses functional molecular materials to construct various electronic components in circuits, such as molecular wires, switches, diodes, field effect transistors, memory devices, *etc.*<sup>81–85</sup> The target of studying molecular electronic devices is to use single molecules, supramolecules or molecular clusters to replace silicon-based semiconductor transistors and other solid electronic components to assemble logic circuits. In particular, the molecules of ferroelectric materials are rearranged under the action of an externally applied voltage, so that the polarization moment of ferroelectric polarization in a certain direction in the crystal is not equal to zero, thereby presenting a polarized electric field in that direction.<sup>86–88</sup> Molecular memory devices are the basic memory element of all electronic devices, which is also an important part of molecular storage and logic devices. Therefore, molecular memory devices are becoming an important research direction for the development of electronic devices in the future.

Electron-type RS behaviour featured by continuous SET/RESET process enables the neuromorphic computing system with high computing precision and avoids the conductance clamping, thus, it is favorable to establish the electron-type RS system by controlling the proportion of charged domain walls in the ferroelectric or ferromagnetic ABO<sub>3</sub> perovskites. The reversible RS behavior between stable, nanoscale, strongly charged domain walls (sCDWs) and the corresponding nano domains in an epitaxial BiFeO<sub>3</sub> (BFO) thin film was reported by Xiaoqing Pan's group.<sup>89</sup> In this research, the RS was performed upon 20 nm thick (001)<sub>P</sub> oriented BFO single crystalline films. A bias was applied between a tungsten surface probe and the La<sub>0.7</sub>Sr<sub>0.3</sub>MnO<sub>3</sub> (LSMO) bottom electrode (Fig. 10a). Fig. 10a presents a schematic diagram of the change of the domain walls (DWs) in the functional layer corresponding to the writing and erasing processes. Interestingly, the bulk domains possess a rhombohedral-like perovskite structure with polarization pointing along the body diagonal of the BiFeO<sub>3</sub> lattice (Fig. 10b). The polarization near the strongly charged domain wall has rotated in the direction normal to the BFO/LSMO interface, which can form a tetragonal-like perovskite structure. This structural change was also reproduced by phase-field simulation of the sCDWs' configuration although the sCDW was inclined (Fig. 10c). On the other hand, the system can be stable without a sCDW under the simulated result (Fig. 10d). This work indicates that the ultrahigh-density information storage can be realized based on the sCDW, which has laid a good experimental foundation for the development of multifunctional molecular memory devices based on multiferroic perovskite materials.

Based on the aforementioned research on tetragonal-like perovskite BiFeO<sub>3</sub> (T-BFO), the photoelectric properties of multiferroic materials have attracted widespread attention. In particular, the photovoltaic effect of BiFeO<sub>3</sub> shows its unique potential applications.<sup>91</sup> Since the bandgap width of BiFeO<sub>3</sub> is about 2.0–3.0 eV, BiFeO<sub>3</sub> is expected to achieve good visible light photovoltaic and photocatalytic effects, suggesting that BiFeO<sub>3</sub> can be used in the research of solar water splitting to produce hydrogen. Thus, BiFeO<sub>3</sub> has good application prospects in the preparation of new energy.<sup>92–94</sup> In previous reports, it was generally believed that the photovoltaic effect of BiFeO<sub>3</sub> is attributed to the interface energy barrier (interface effect), ferroelectric polarization (body effect), and the defect concentration gradient under an applied electric field.<sup>95</sup> In order to better present these effects, a single crystal film prepared by the epitaxy method is crucial. A typical experiment should be mentioned in which a well-ordered microarray of epitaxial tetragonal BiFeO<sub>3</sub> (T-BFO) films on the single-crystal (001)-LaAlO<sub>3</sub> substrate with a 10 nm thick La<sub>0.67</sub>Sr<sub>0.33</sub>MnO<sub>3</sub> (LSMO) buffer layer was deposited by PLD.<sup>90</sup> This single-crystal (001)-LaAlO<sub>3</sub> substrate provides a key factor for the preparation of single-crystal T-BFO films. In the micro-array, each cell was designed as a square with various side lengths and gap widths, as shown in Fig. 10e. To study the ferroelectric photovoltaic effect of the Au/Cr(Ti)/T-BFO/LSMO structure, a combined measurement system integrating a scan probe microscope (SPM) was used, as sketched in Fig. 10f. The rapid photovoltaic response to incident light provides a feasible way to develop a unique technology for information memory and logical computing. In order to build an array of memory devices, a sandwich structure based on the Au/Cr/T-BFO/LSMO microarray was proposed, as shown in Fig. 10g. Each intersection of the device represents a logic state, which can achieve good information processing through logic operations. In addition, a RS device using the presented tunable ferroelectric photovoltaic effect of Au/Cr/T-BFO/LSMO was also developed, as shown in Fig. 10h. For a given cell (such as B device unit) with the P<sub>down</sub> state, its logic state can be reversibly switched between the ON and OFF states by controlling the incident laser, and then it can be read out by detecting the corresponding V<sub>OC</sub> (J<sub>SC</sub>). Therefore, this work is greatly meaningful for deeply understanding the photovoltaic process of BiFeO<sub>3</sub>-based devices at the microscale and provides a feasible approach for developing information memory and in-memory devices using the ferroelectric photovoltaic effect.

In addition to BiFeO<sub>3</sub>, BaTiO<sub>3</sub> was also reported as an important multiferroic material in the ABO<sub>3</sub> system with a wide range of applications.<sup>96–100</sup> BaTiO<sub>3</sub> has a large dielectric constant and a small dielectric loss, and it is one of the widely used materials in electronic insulating ceramic materials. The spontaneous polarization of BaTiO<sub>3</sub> mainly comes from the ion displacement polarization of Ti<sup>4+</sup> and the electron displacement polarization of O<sup>2–</sup>. In the field of ceramics, BaTiO<sub>3</sub> is mainly used as an insulation layer in electronic ceramics, thermistors, capacitors, electronic components, and in the reinforcement of some composite materials. Furthermore, the

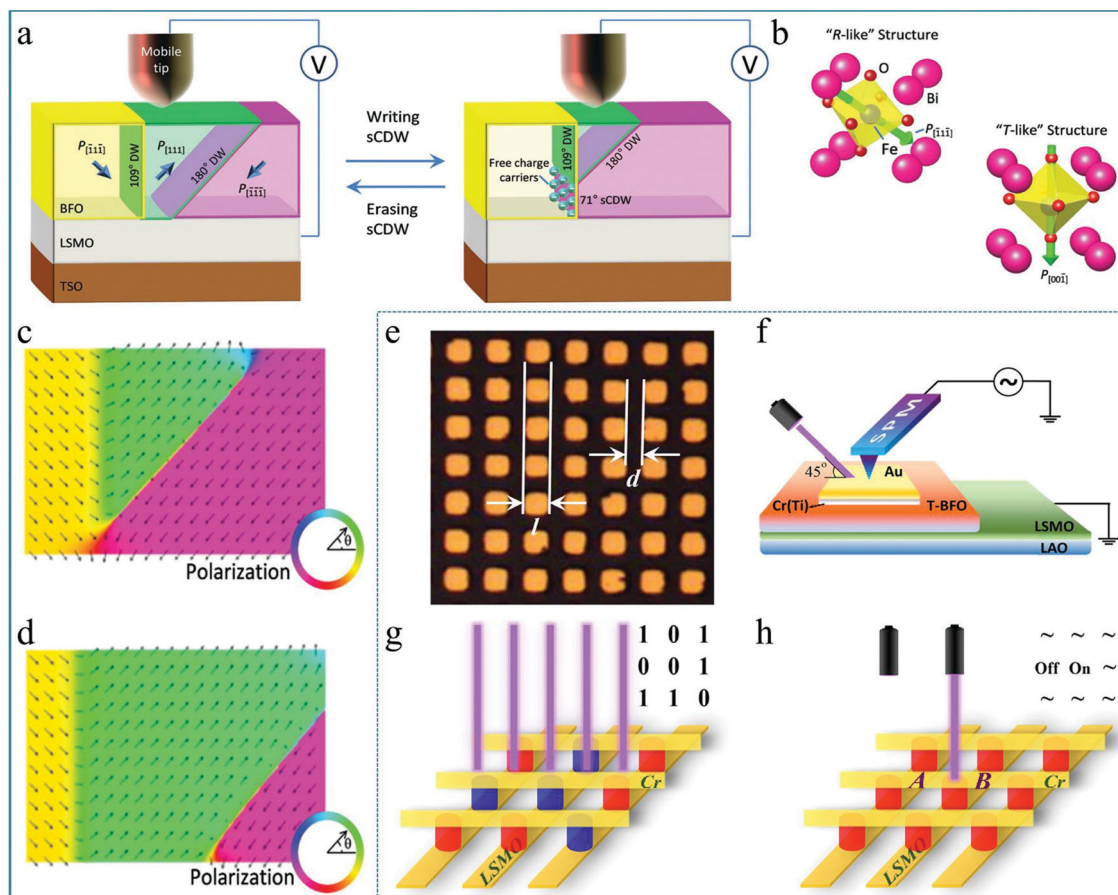


**Fig. 10** (a) Schematic of the experimental set-up; (b) atomic models of the R-like structure of the domains and the T-like structure of the sCDW in  $\text{BiFeO}_3$ , in which the polarizations are shown by green arrows; (c) phase-field simulation of the polarization distribution in the plane of the image of the stable domain structure with a sCDW in a  $\text{BiFeO}_3$  film; (d) simulated polarization distribution in the plane of the image of the stable domain structure of the system without a sCDW where the arrows mark the polarization orientations. Panels a–d reproduced with permission.<sup>89</sup> Copyright 2016, Wiley-VCH. (e) Optical image of the microarray derived from Au/Ti (or Cr)/T-BFO/LSMO, in which the side length of each square electrode is  $l = 2.5, 5, 10$ , and  $20 \mu\text{m}$  and the gap between the squares is  $d = 1.5, 5, 5$ , and  $5 \mu\text{m}$ ; (f) setup for measuring the local photovoltaic effect; (g) data storage and (h) logic switching microdevice prototype designed based on the Au/Cr/T-BFO/LSMO microarray. The yellow bars represent electrodes (LSMO and Cr); the red and blue columns represent the  $P_{\text{down}}$  state and  $P_{\text{up}}$  state, respectively, of the T-BFO films. Panels e–h reproduced with permission.<sup>90</sup> Copyright 2017, American Chemical Society.

multiferroic perovskite-type  $\text{BaTiO}_3$  has also been used in energy storage and catalysis research,<sup>101–105</sup> and it can present more characteristics through element doping.  $\text{BaTiO}_3$  as one of the important members of the  $\text{ABO}_3$  family also exhibits great potential application in the neuromorphic computing system because its spontaneous polarization features are possibly used to simulate the physical biodynamic process.

Zhibo Yan *et al.* fabricated a RS memory device using 5 at% Co-doped  $\text{BaTiO}_3$  (BTCO) as a functional layer, which demonstrated a unipolar RS characteristic.<sup>106</sup> Fig. 11a depicts a schematic drawing of the measurement configuration, in which Au works as the top electrode and Pt works as the bottom electrode. Fig. 11b shows the typical  $I$ - $V$  characteristics of the memory cell, displaying an obvious set and reset process appearing in the same voltage area (positive voltage region or negative voltage region), which is confirmed as a unipolar RS effect. The SEM image of the cross-sectional profile of the as-prepared BTCO thin film is shown in Fig. 11c, showing that the thickness of the BTCO layer is  $\sim 400 \text{ nm}$ . Finally, to verify

the inhomogeneous conduction of the memory cell and therein the filament model, an Au top electrode was prepared to set the memory cell into the LRS, then the electrode was cut into two parts ( $TE-I$  and  $TE-II$ ) using the probe tip, and the resistances between the bottom electrode and  $TE-I$  or  $TE-II$  were measured, as shown in Fig. 11d. It shows multiple logic states by selecting contacts with different electrodes. The data obtained above confirm that the multiferroic perovskite  $\text{BaTiO}_3$  can offer a good opportunity for developing RRAM devices with more promising functionalities. Furthermore, Nathalie Jedrecy *et al.* prepared a RS device based on the multiferroic  $\text{BaTiO}_3/\text{La}_{0.75}\text{Sr}_{0.25}\text{MnO}_3$  (BTO/LSMO) system.<sup>107</sup> The hysteretic  $I$ - $V$  curves of the Au/BTO/LSMO structure show an obvious bipolar RS behavior, as shown in Fig. 11e. It can be confirmed that Ba and Ti ions in LSMO are diffused from the observation of the high-resolution STEM image in Fig. 11f. Therefore, this study confirmed the important role of ion exchange and redox processes in the heterojunction interface in RS devices.



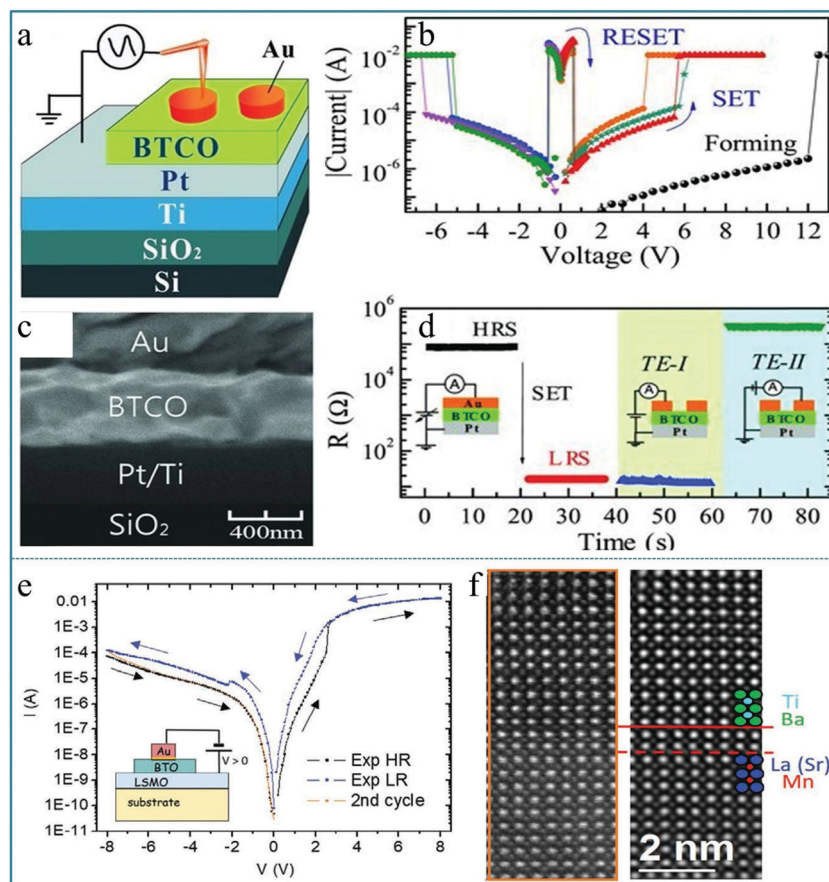


**Fig. 11** (a) A schematic drawing of the measurement configuration; (b) typical  $I$ - $V$  characteristics of the device; (c) cross-sectional SEM image of a memory cell; (d) resistances measured for various configurations, in which the top electrode (TE) was cut into TE-I and TE-II by the probe tip after the cell was switched from a HRS to a LRS. Panels a–d reproduced with permission.<sup>106</sup> Copyright 2011, Wiley-VCH. (e) The  $I$ - $V$  hysteresis curve in a logarithmic form, and the inset shows the Au/BTO/LSMO structure; (f) the high resolution raw (left) and filtered (right) STEM images. Panels e and f reproduced with permission.<sup>107</sup> Copyright 2021, Wiley-VCH.

At present, the perovskite-type  $\text{LaMnO}_3$  is used for various energy storage and magnetic devices, and has become a widely studied functional material.<sup>108–113</sup>  $\text{LaMnO}_3$  is a typical ferromagnetic material, and it has a wide range of applications in spin valves, magnetic read heads and exchange bias devices.<sup>114–117</sup> In particular,  $\text{LaMnO}_3$  exhibits a good exchange bias dependence on direction in a heterojunction superlattice.<sup>118</sup> These characteristics make  $\text{LaMnO}_3$  an advanced functional material in the preparation of spintronic devices. The ferromagnetic property originating from  $\text{LaMnO}_3$  endows the  $\text{LaMnO}_3$ -based memristor with enriched spin electron effects, such as electron spin transport, coupling and resonance. Utilizing these advantages, the RS behaviours elaborately modulated by signal parameters (voltage magnitude) in a computing system can efficiently simplify the external circuit, and thus cutoff the hardware cost.

It should be mentioned that Andrés Gómez *et al.* prepared a RS device with  $\text{BaTiO}_{3-\delta}/\text{La}_{0.7}\text{Sr}_{0.3}\text{MnO}_3/\text{SrTiO}_3/\text{Si}$  structure by a relatively complicated process and measured the RS characteristics.<sup>119</sup> It was found that the ferroelectric polarization can be reversed upon a mechanical load in the as-prepared RS device. Thus, a mechanically controlled multilevel device was further designed. Fig. 12a shows the complex epitaxial

heterostructures grown in three different stages. The SEM image confirms this multi-layer structure device (Fig. 12b). The measurements of electron energy-loss spectroscopy (EELS) with atomic resolution shows some cation intermixing is restricted in the interface, which is in agreement with the contrast, as shown in Fig. 12c. This special interface is usually an important factor for heterojunction devices. Next, the charge transport and RS behavior of the  $\text{BaTiO}_{3-\delta}$  film were investigated. The test configuration is shown in Fig. 12d, in which the CAFM tip works as the top electrode and  $\text{La}_{0.7}\text{Sr}_{0.3}\text{MnO}_3$  works as the bottom electrode. By setting a bias voltage of  $-6.0$  V on the  $\text{La}_{0.7}\text{Sr}_{0.3}\text{MnO}_3$  bottom electrode, the device was set into a LRS while a  $+6.0$  V bias switched the device to a HRS (Fig. 12e), implying that a bipolar RS effect with obvious asymmetry can be implemented in the as-fabricated RS device. Fig. 12f shows the mapping diagram of the  $\text{BaTiO}_3$  film with a thickness of 45 nm. It can be seen that the RS device can be driven by electric polarization (right) and mechanical loading force (left), and the resistance state can be changed between LRS and HRS. Finally, the authors summarize the configurations in which the system can be switched internally between HRS and LRS upon application of those external stimuli.<sup>119</sup> Therefore, this

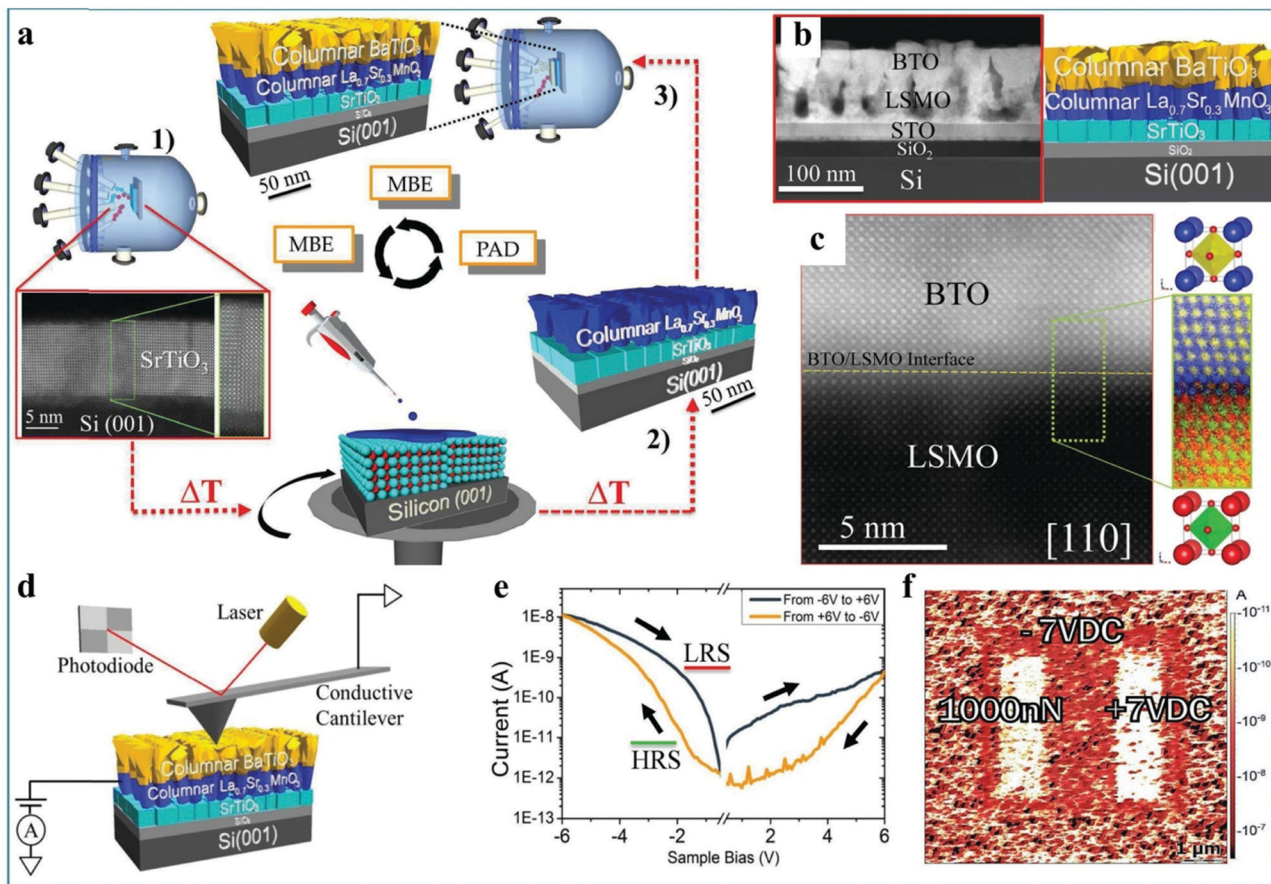


**Fig. 12** (a) Schematic diagram illustrating a new preparation approach combining molecular beam epitaxy (MBE) and polymer assisted deposition (PAD). (b) Low magnification Z-contrast image of a porous epitaxial BaTiO<sub>3-δ</sub>/La<sub>0.7</sub>Sr<sub>0.3</sub>MnO<sub>3</sub>/SrTiO<sub>3</sub>/Si (001) multilayer along the [110] Si axis (left panel), corresponding to the sketch of the heterostructure (right panel). (c) High resolution Z-contrast image of the BaTiO<sub>3-δ</sub>/La<sub>0.7</sub>Sr<sub>0.3</sub>MnO<sub>3</sub> interface (yellow dashed line) along the Si [110]-crystallographic direction, and higher resolution Z-contrast image of the coherent interface between BaTiO<sub>3-δ</sub> and La<sub>0.7</sub>Sr<sub>0.3</sub>MnO<sub>3</sub> layers. (d) Schematic of the CAFM system used for nanoscale electrical measurements. (e) The bipolar RS characteristic of epitaxial columnar BaTiO<sub>3-δ</sub>/La<sub>0.7</sub>Sr<sub>0.3</sub>MnO<sub>3</sub>/SrTiO<sub>3</sub>/Si (001) films. (f) Mapping of the electrical current of the 45 nm thick BaTiO<sub>3</sub> film shows the piezo-driven RS effect between a LRS and a HRS domain by electrical poling (right) and mechanical loading force (left). All panels reproduced with permission.<sup>119</sup> Copyright 2017, Wiley-VCH.

work indicates that perovskite-type heterojunctions have great potential applications in multistate RS devices due to the special performance of the interface layer, which provides an innovative pathway toward the design and integration of nonvolatile mechanoelectrically controlled multilevel RS devices. The mechanoelectrical RS performance has potential applications in information memory and sensor applications.

SrTiO<sub>3</sub> (STO) is one of the most extensively studied perovskite materials with multiferroic properties in the family of multiferroic materials, and it exhibits many intriguing physical and chemical properties.<sup>120–123</sup> SrTiO<sub>3</sub> has very good thermal stability, and thus it can be used in electronic ceramic materials and in the manufacture of diamonds.<sup>124–128</sup> SrTiO<sub>3</sub> is a center-symmetric paraelectric dielectric material with a perovskite structure at room temperature, and it has a very large dielectric constant at low temperatures.<sup>129</sup> In addition, SrTiO<sub>3</sub> has a band gap of 3.2 eV and shows good photocatalytic activity.<sup>130</sup> Many reports have confirmed that SrTiO<sub>3</sub> has unique oxidation–reduction catalytic activity, and it has been widely used in the

fields of photocatalytic water splitting to produce hydrogen, photocatalytic degradation, photochemical batteries, and so on.<sup>131–133</sup> The SrTiO<sub>3</sub>-based memristor endowed with both nonvolatile and volatile RS behaviors triggered by the multiferroic-induced phase change exhibits multi-order states, which enables more faithful simulation of the synaptic plasticity.

At present, SrTiO<sub>3</sub> also presents many advantages in the research of RS devices.<sup>134–136</sup> Hyunsoo Lee *et al.* demonstrated a bipolar RS device based on Nb-doped SrTiO<sub>3</sub>.<sup>137</sup> During the experiment, the CAFM tip was used to contact the Pt nanodisk electrode on a Nb-doped SrTiO<sub>3</sub> (Nb:STO) single crystal under the condition of ultrahigh vacuum. By applying a bias of  $\pm 8.0$  V on the RS device, the *I*–*V* curves were obtained. In the process of testing, silver paste and indium with good conductivity were employed to make Ohmic contact between the Nb:STO single crystal and the bottom electrode, as shown in Fig. 13a. The results suggested that the RS device can be scaled down to the 10 nm range for high-density RRAM devices. In addition, Shuxiang Wu *et al.* reported a reversible RS behavior in a

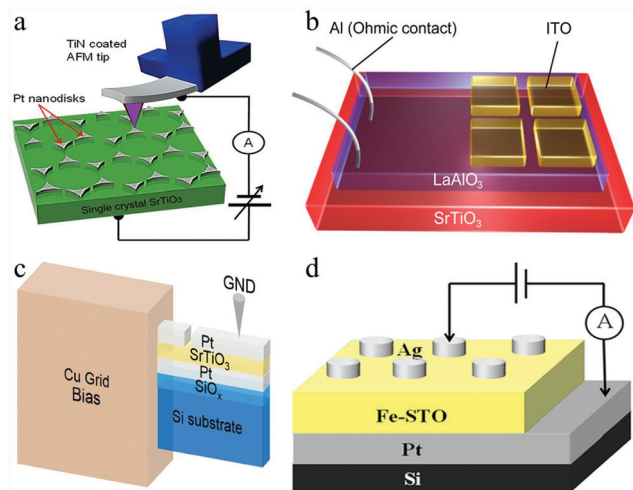


**Fig. 13** (a) Scheme for nanoscale bipolar RS phenomena on a triangular-shaped Pt nanodisks/Nb:STO single crystal Schottky junction; probing with CAFM in ultrahigh vacuum. Reproduced with permission.<sup>137</sup> Copyright 2013, American Chemical Society. (b) Schematic diagram of the transparent ITO/LAO/STO memristor. Reproduced with permission.<sup>138</sup> Copyright 2014, American Chemical Society. (c) Schematic of the TEM sample used for *in situ* *I*-*V* experiments. Reproduced with permission.<sup>139</sup> Copyright 2019, Wiley-VCH. (d) Schematic diagram of the Ag/Fe-SrTiO<sub>3</sub>/Pt memory cell. Reproduced with permission.<sup>140</sup> Copyright 2020, AIP Publishing.

transparent ITO/LaAlO<sub>3</sub>/SrTiO<sub>3</sub> (ITO/LAO/STO) structure device at room temperature.<sup>138</sup> To investigate the RS characteristics, wire-shaped Al electrodes were directly contacted with the electron gas and ITO as a counter electrode, as shown in Fig. 13b. This work shows that the LAO/STO heterostructure-based device features good electronic transparency, a high HRS/LRS resistance ratio, good endurance, and long retention of logic states, and is expected to be used in high-performance information processing technologies.

Further, Deok-Hwang Kwon *et al.* elucidated the mechanism of filament formation and observed its associated RS effect in a SrTiO<sub>3</sub> based special shaped structural device.<sup>139</sup> Fig. 13c shows a schematic diagram of the structure of the device. In the process of electronic testing, a bias was applied to the bottom electrode while grounding the Pt/Ir-coated W scanning tunneling microscope (STM) tip, which remained in contact with the top electrode of the device. In order to hinder the flow of DC current to the Cu grid through the top electrode, a focused ion beam (FIB) was used to cut off the top electrode near the grid. Thus, this work provides detailed insights into the origin and mechanisms of filament generation and rupture. In addition, many reports confirm that the doping of metal elements can effectively reduce the switching voltage of the device.<sup>141,142</sup> Xue Jiang *et al.* deposited Fe-doped SrTiO<sub>3</sub> (Fe-STO) films on a Si substrate by magnetron sputtering to build a RS device with Ag/Fe-STO/Pt structure as illustrated in Fig. 13d, and then investigated the effect of deposition temperature on the RS characteristics.<sup>140</sup> It was experimentally observed that the stability of the RS device was significantly improved as the deposition temperature increased. This work indicates that Fe doping can effectively improve the formation of oxygen vacancy

conductive filaments in highly crystalline SrTiO<sub>3</sub> films, resulting in a small switching voltage for the Ag/Fe-STO/Pt device. Therefore, such devices have potential applications in low-voltage RS memory devices.

More recently, the RS applications of composite multiferroic perovskite oxides, such as SrFeO<sub>x</sub>, SrTiO<sub>3</sub> and La<sub>2/3</sub>Sr<sub>1/3</sub>MnO<sub>3</sub>, have also attracted the attention of researchers.<sup>143–145</sup> The structure can change between limonite and perovskite when oxygen ions are diffused.<sup>146,147</sup> The memristive effect based on the structural phase change has led to the realization of phase-change memristors. As the name suggests, phase change memory is a kind of RS memory that uses the reversible conversion of conductivity in special materials between the crystalline state and the amorphous state as a logic state to store data. Moreover, phase change memory has the advantages of fast access speed and high reliability, and has broader application space and better developmental trends than other memories. Among all phase change materials studied, the reversible phase transformation between brownmillerite SrCoO<sub>2.5</sub> (BM-SCO) and perovskite SrCoO<sub>3</sub> (P-SCO) has important potential applications and has received widespread attention. Jie Zhang *et al.* prepared SrCoO<sub>3-δ</sub> films by the PLD technique and demonstrated a phase competition under different temperatures.<sup>148</sup> The summarization of *c*-axis lattice constants is shown in Fig. 14a, in which the dashed line indicates the theoretical *c*-axis lattice constant for the P-SCO film strained on LaAlO<sub>3</sub> substrates. In this figure, it can be divided into three areas due to the *c*-axis lattice constants compared with the theoretical parameter. Fig. 14b shows the temperature dependent Gibbs free energy of SrCoO<sub>2.5</sub> and SrCoO<sub>3</sub> by first principles calculations, in which the structure models of SrCoO<sub>3</sub> and SrCoO<sub>2.5</sub> are displayed in the left and right areas, respectively, and the arrows in the inset schematic diagrams indicate the trend of stabilizing the specific phase structure. Therefore, the conversion between BM-SCO and P-SCO is closely related to a large number of oxygen vacancies.

Hung-Yang Lo *et al.* deposited SrCoO<sub>x</sub> (SCO) on a niobium-doped SrTiO<sub>3</sub> (Nb-STO) substrate by PLD as the functional layer to prepare a RS device with Au as the top electrode and Nb-STO as the bottom electrode.<sup>149</sup> The schematic diagram of the device is shown in Fig. 14c; Fig. 14d shows the obvious bipolar RS behavior of the device. We can see that the RS device has a very stable property, and it can be circulated continuously for 100 cycles without any attenuation. Fig. 14e shows a retention time of 10<sup>4</sup> s for the Au/SCO/Nb-STO device. Further, the detailed information of the conductive filament can be directly derived from the STEM image in Fig. 14f and g. The color difference can indirectly reflect the structural changes of the material. Fig. 14h shows the EELS spectrum of the Co L-edge from the conductive filament. Fig. 14i shows the schematic diagram of the topotactic phase transformation behavior between BM-SCO and P-SCO under an applied voltage. This reversible change of the phase structure provides a good guarantee for the information processing of the phase change memory device. The work demonstrated the excellent RS properties of the Au/SCO/Nb-STO device and also provided a new



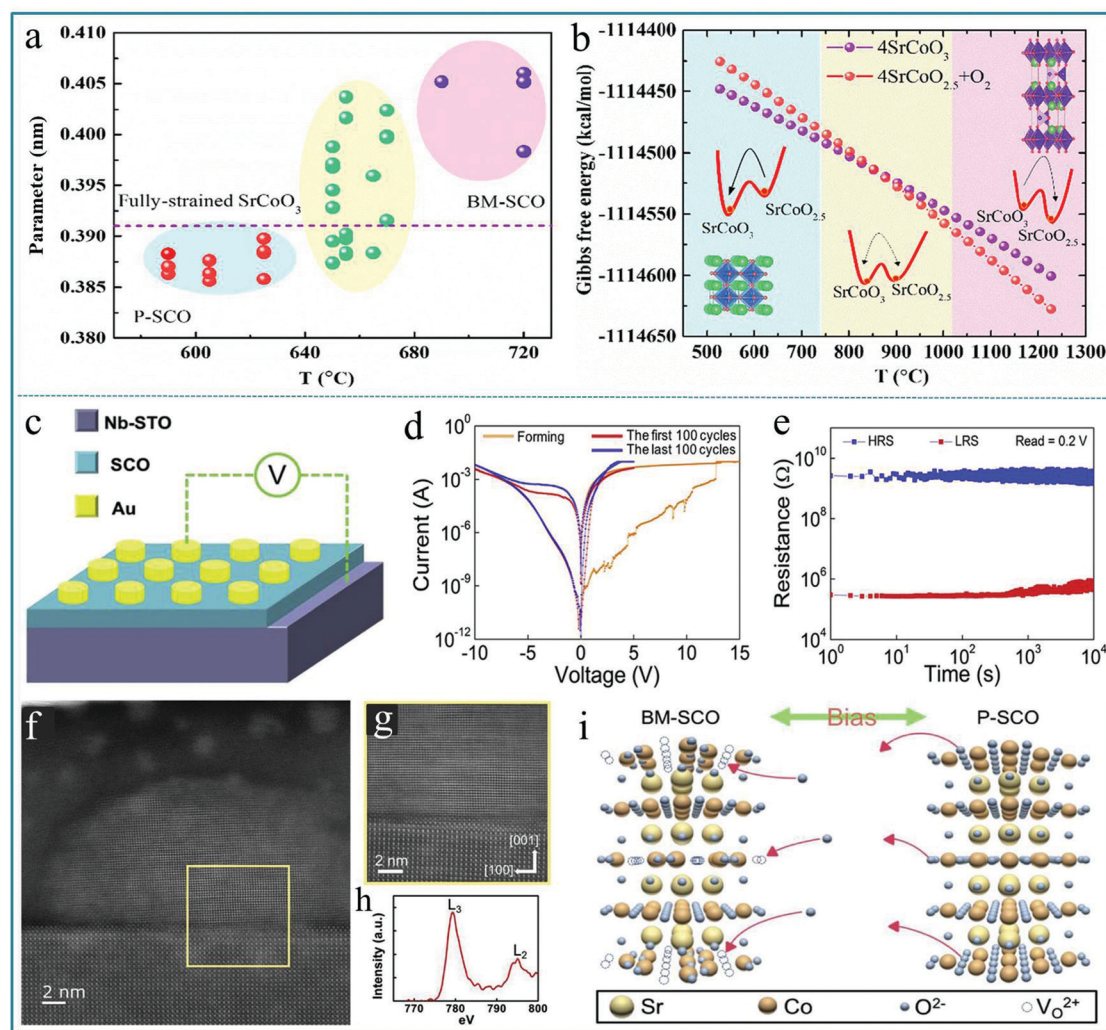


**Fig. 14** (a) Summarization of *c*-axis lattice constants; (b) temperature dependent Gibbs free energy of  $\text{SrCoO}_{2.5}$  and  $\text{SrCoO}_3$  by first principles calculations. Panels a and b reproduced with permission.<sup>148</sup> Copyright 2020, AIP Publishing. (c) The schematic diagram of devices, in which the bias was applied to the Au electrode and the Nb-STO electrode was grounded; (d) the electrical measurement of the RS behavior shows the typical Forming, Set, and Reset processes where the red and blue curves indicate the first and last 100 cycling tests, respectively; (e) the retention measurement of devices; (f) STEM image of the nanofilament region; (g) HR-STEM image of the interface between the P-SCO nanofilament and the STO electrode; (h) Co L-edge EELS spectrum of the nanofilament region; (i) the schematic diagram of the topotactic phase transformation between BM-SCO and P-SCO. Panels c–i reproduced with permission.<sup>149</sup> Copyright 2020, Elsevier.

aspect for selecting the dielectric layer material in RS devices. It can be believed that the complex oxides can be widely applied as effective functional materials of memory devices in the near future.<sup>150</sup>

With the development of research on multiferroic perovskite materials, some new materials are constantly being discovered. For example, the perovskite  $\text{AlFeO}_3$  has been studied as one of the potential multiferroic materials,<sup>151–153</sup> and it can be used for preparing information memory devices. It is confirmed that  $\text{AlFeO}_3$  is composed of oxygen octahedra and tetrahedra containing Al and Fe ions,<sup>154</sup> as shown in Fig. 15a. Its crystal has a non-centrosymmetric polar structure corresponding to the space group  $Pna2_1$ . Generally, the structure of  $\text{AlFeO}_3$  can be described as a combination of hexagonal close packing and cubic close packing of oxygen ions (Fig. 15b).  $\text{AlFeO}_3$  can usually

be successfully prepared by a high temperature solid phase method or an epitaxy method.<sup>154</sup> In addition to good ferroelectric properties,  $\text{AlFeO}_3$  exhibits obvious ferromagnetic properties with a Néel temperature of 317 K.<sup>154</sup> This special combination makes multiferroic perovskite  $\text{AlFeO}_3$  have many special physical properties, and it is expected that some components with multiple physical properties can be used in multifunctional electronic devices. Badari Narayana Rao *et al.* prepared  $\text{Al}_x\text{Fe}_{2-x}\text{O}_3$  ( $0.5 \leq x \leq 1$ ) thin films,<sup>155</sup> in which ferrimagnetism, ferroelectricity, and magnetoelectric coupling were simultaneously observed. The schematic of the orientation relationship between film domains and the substrate is shown in Fig. 15c. Fig. 15d shows the room temperature hysteresis loops ( $M-H$ ) of  $\text{Al}_x\text{Fe}_{2-x}\text{O}_3$  with  $x = 0.5, 0.8$  and  $0.9$ , indicating the ferrimagnetism of  $\text{Al}_x\text{Fe}_{2-x}\text{O}_3$ . Fig. 15e graphically

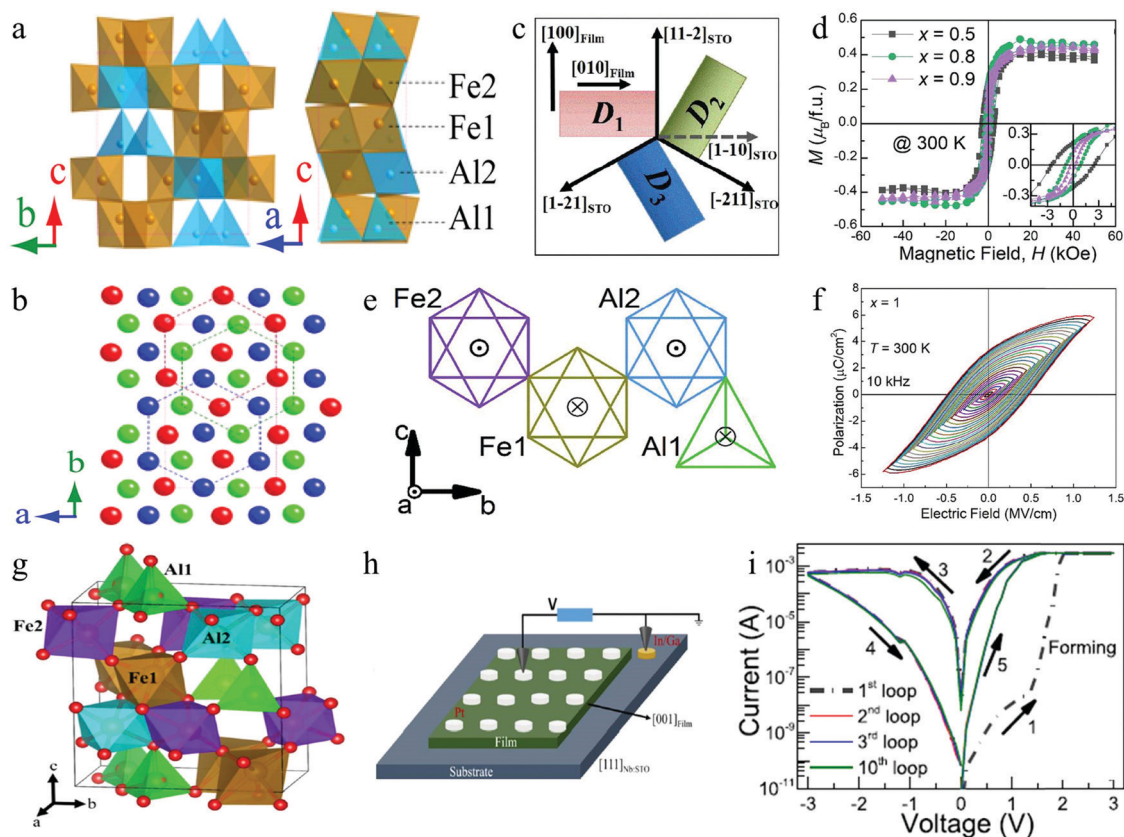


**Fig. 15** (a) Crystal structure of  $\text{AlFeO}_3$ ; (b) close-packed oxygen layers projected along the  $c$ -axis. Panels a and b reproduced with permission.<sup>154</sup> Copyright 2014, AIP Publishing. (c) Schematic of the orientation relationship between film domains and the substrate; (d) room temperature hysteresis loops ( $M-H$ ) with different compositions; (e) schematic of the direction of magnetic moments of  $\text{Fe}^{3+}$  ions at each site; (f)  $P-E$  hysteresis loops of  $\text{AlFeO}_3$  ( $x = 1$ ) at 10 kHz with increasing maximum electric fields. Panels c–f reproduced with permission.<sup>155</sup> Copyright 2020, Royal Society of Chemistry. (g) Model of the orthorhombic crystal structure of the  $\text{AlFeO}_3$  film; (h) schematic of the  $\text{Pt}/\text{AlFeO}_3/\text{Nb:STO}$  heterostructure; (i)  $I-V$  loops of the heterostructure show the RS behavior. Panels g–i reproduced with permission.<sup>156</sup> Copyright 2020, American Chemical Society.

shows the magnetic moment direction of  $\text{Fe}^{3+}$  ions at each position in a unit cell, in which  $\odot$  indicates that the spin orientation of  $\text{Fe}^{3+}$  is outside the paper plane and  $\otimes$  indicates that the spin orientation is within the paper plane. It can be seen that Fe2, Al2 and Fe1 correspond to the octahedral oxygen coordination sites, while Al1 corresponds to the tetrahedral coordination site. Fig. 15f shows the polarization vs. electric-field ( $P-E$ ) hysteresis curves of the  $\text{AlFeO}_3$  ( $x = 1$ ) sample with increasing electric field. Therefore, this study confirms that  $\text{Al}_x\text{Fe}_{2-x}\text{O}_3$  ( $0.5 \leq x \leq 1$ ) is a potential multiferroic perovskite material, which can simultaneously exhibit ferromagnetism and ferroelectricity at room temperature.

Importantly, Badari Narayana Rao *et al.* reported the multi-level RS characteristics of the  $\text{Pt}/\text{AlFeO}_3/\text{Nb-doped SrTiO}_3$  (111) heterostructure.<sup>156</sup> In this research, they carried out a systematic study to characterize and understood the switching process in the as-prepared RS device. A schematic of the crystal structure of the perovskite  $\text{AlFeO}_3$  is shown in Fig. 15g. The structure schematic of the RS device is shown in Fig. 15h, in which the Pt electrode with a diameter of 100  $\mu\text{m}$  was deposited on the  $\text{AlFeO}_3$  film. Fig. 15i shows a typical bipolar  $I-V$  plot obtained from the  $\text{Pt}/\text{AlFeO}_3/\text{Nb-doped SrTiO}_3$  heterostructure device,

which clearly shows the presence of two resistance states (HRS and LRS) and the reversible transition between HRS and LRS. Finally, the mechanism of the Fe-redox process through the participation of oxygen vacancies and oxygen ions was proposed. Therefore, the multilevel RS can be realized in the  $\text{Pt}/\text{AlFeO}_3/\text{Nb-doped SrTiO}_3$  heterostructure device. Indeed, the multilevel RS characteristics are attractive for high-density nonvolatile memories and neuromorphic computing.<sup>157–160</sup> These results should inspire further research in order to achieve attractive RS properties with potential applicability in intelligent systems.

It is known that perovskite oxides are prone to generate oxygen vacancies due to the lack of oxygen during the preparation process,<sup>161</sup> so it is generally considered that the oxygen vacancies are a major cause of the RS effect in perovskite oxide thin films with rich oxygen vacancies.<sup>162–164</sup> Zhong-tang Xu *et al.* prepared  $\text{LaMnO}_3$  (LMO) films with different concentrations of oxygen vacancies on a  $\text{SrTiO}_3/\text{Nb}$  (0.8 wt%) (SNT0) substrate by adjusting the oxygen pressure during the deposition process using vacuum deposition technology.<sup>165</sup> Fig. 16a–c displays the cross-sectional annular-bright-field (ABF) micrographs, in which some obvious changes can be seen at the



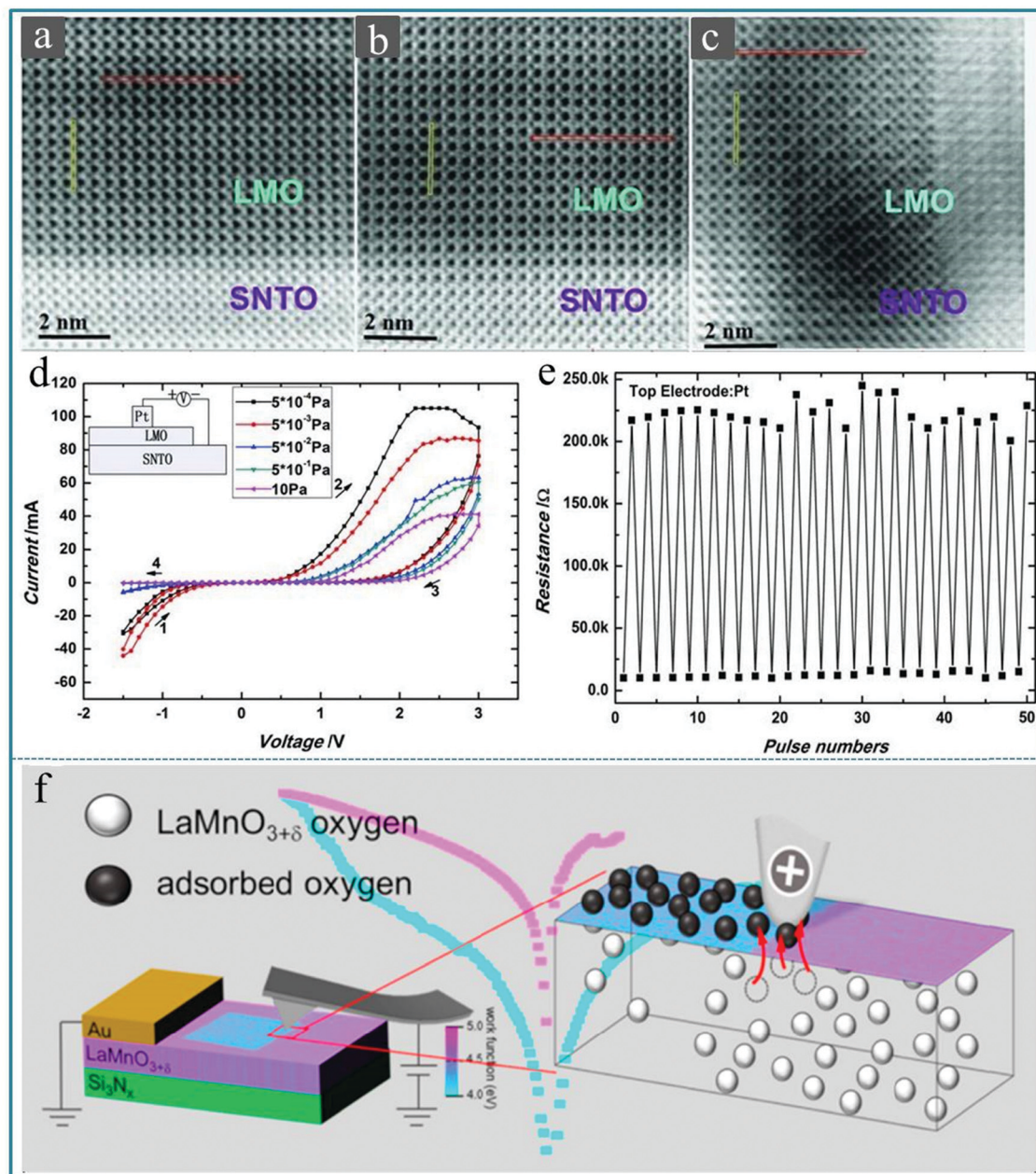


**Fig. 16** (a–c) Annular-bright-field (ABF) micrographs of the LMO/SNT0 interfaces along the [001] axis corresponding to oxygen pressures of 10,  $5 \times 10^{-1}$ , and  $5 \times 10^{-2}$  Pa, respectively, in which La is represented by the darkest spots, whereas O is represented by the lightest spots. (d) Typical  $I$ – $V$  curves for Pt/LMO/SNT0 devices under oxygen pressures of 10,  $5 \times 10^{-1}$ ,  $5 \times 10^{-2}$ ,  $5 \times 10^{-3}$ , and  $5 \times 10^{-4}$  Pa. The direction of bias sweeping is indicated by arrows, and the inset shows the measurement configuration of the devices. (e) Pulse measurements of the Pt/LMO/SNT0 devices with a fabrication oxygen pressure of  $5 \times 10^{-4}$  Pa; the pulse condition for the HRS is +5.0 V with a pulse width of 1 ms and for the LRS it is –5.0 V with a pulse width of 1 ms, and the resistance was read out at 0.1  $\mu$ A. Panels a–e reproduced with permission.<sup>165</sup> Copyright 2012, Wiley-VCH. (f) Schematic diagram of the microscopic mechanisms of local interfacial RS in LaMnO<sub>3+δ</sub>. Reproduced with permission.<sup>166</sup> Copyright 2020, American Chemical Society.

LMO/SNT0 interface when the preparation condition was changed. Furthermore, a RS memory device with Pt/LMO/SNT0 structure was built using the as-prepared heterostructure. Fig. 16d displays the typical  $I$ – $V$  characteristics of the Pt/LMO/SNT0 device under various oxygen pressures. The inset of Fig. 16d exhibits the schematic setup for  $I$ – $V$  measurements, in which Pt works as the top electrode and SNT0 works as the bottom electrode. We can see that the resistance window of the

device in the positive voltage region gradually decreases as the oxygen pressure increases, which implies that the oxygen vacancy concentration can effectively affect the RS performance of the Pt/LMO/SNT0 device. Finally, to evaluate the stability of the Pt/LMO/SNT0 device for information storage applications, the endurance measurements were further performed for the as-fabricated Pt/LMO/SNT0 device under a stable oxygen pressure of  $5.0 \times 10^{-4}$  Pa. The device did not show significant



attenuation after 50 testing cycles, as shown in Fig. 16e. Therefore, it is a feasible method to control the concentration of oxygen vacancies in the perovskite oxide by controlling the oxygen pressure during the vacuum deposition process or the subsequent annealing treatment in the oxygen atmosphere of the sample, thereby controlling its RS memory performance. Furthermore, Benjamin Meunier *et al.* prepared a RS device using a perovskite  $\text{LaMnO}_{3+\delta}$  thin film with a thickness of 25 nm as a functional layer on the  $\text{SiN}_x/\text{SiO}_2/\text{Si}$  substrate by chemical vapor deposition (CVD).<sup>166</sup> It was found, based on conductive atomic force microscopy (c-AFM), that the resistance change would be triggered when the oxygen ions were adsorbed on the surface, as shown in Fig. 16f. This work provides a complete and comprehensive description of the physical mechanism involved in the interface resistance conversion on the surface of the  $\text{LaMnO}_{3+\delta}$  film based on the oxygen content.

It should be mentioned that single crystal  $\text{LaAlO}_3$  has the characteristics of good lattice matching to a variety of perovskite structure materials, and is usually used as a substrate material for preparing perovskite thin films.<sup>167</sup> The dielectric properties of  $\text{LaAlO}_3$  are favorable for low-loss microwave and dielectric resonance applications.<sup>168</sup> Generally,  $\text{LaAlO}_3$  has stable chemical properties and is insoluble in mineral acids at room temperature.<sup>169</sup>  $\text{LaAlO}_3$  usually has a hexagonal crystal structure at room temperature, and it will transform into a cubic structure when the temperature exceeds 400 °C.<sup>170,171</sup> Tom Wu' group reported the RS memory behavior of the  $\text{Pt}/\text{LaAlO}_3/\text{SrTiO}_3$  ( $\text{Pt}/\text{LAO}/\text{STO}$ ) device.<sup>172</sup> The structures of the memristor and FET are shown in Fig. 17a. It can be seen that the uppermost unit cell of LAO is discontinuous, which implies that there is a certain degree of transitional fluctuation in the thickness of the LAO layer (Fig. 17b). The interface between the LAO layer and the STO substrate is atomically flat, which is indicated by arrows in Fig. 17c. The  $I$ - $V$  curves of the  $\text{Pt}/\text{LAO}/\text{STO}$  device exhibit a significant RS feature in an applied voltage sweep from  $-4.0$  to  $4.0$  V, as shown in Fig. 17d. At the same time, Fig. 17e shows good endurance and consistent performance during more than 2000 operation cycles. Finally, it was proposed that the RS behavior may be caused by the drift of the charged oxygen vacancies across the LAO/STO interface led by the electric field and the gap states led by defects in the ultrathin LAO layer. Besides, Zhaomeng Gao *et al.* developed a ferroelectric memristor, in which the 2D electron gas resistance can be changed at the  $\text{LaAlO}_3/\text{SrTiO}_3$  heterointerface.<sup>173</sup> The schematic of the  $\text{Pt}/\text{BFO}/\text{LAO}/\text{STO}$  heterostructure device is shown in Fig. 17f. Fig. 17g shows an optical image of the  $\text{Pt}/\text{BFO}/\text{LAO}/\text{STO}$  device and the measurement pattern. This work confirmed that the  $\text{ABO}_3$  perovskites heterojunction device exhibited intriguing properties, which can be respected to be used as nonvolatile memories and photodetectors in electronics. Therefore, it can be concluded that these metal-oxide-oxide heterojunctions with atomically smooth interfaces and controlled defect transmission have good RS memory behavior, which provides a development space for integrated logic and nanoelectronics for memory technology. Here, we

should note that the  $\text{LaAlO}_3/\text{SrTiO}_3$  heterojunction has many important applications, such as superconductivity, two-dimensional (2D) electron gas, spin-valve devices, *etc.*<sup>174–178</sup> These important applications stem from special interface effects of  $\text{LaAlO}_3/\text{SrTiO}_3$ . Therefore, the interface effect of the perovskite heterojunction is a very important research topic in material applications.

Finally, we should mention a special perovskite material  $\text{PbTi}_x\text{Zr}_{1-x}\text{O}_3$  (PZT), which is also the main component of piezoelectric ceramics. The piezoelectric properties of PZT not only change with the atomic ratio of Zr/Ti, but also change with different additives.<sup>179–182</sup> When the additive has the same valence as  $\text{Pb}^{2+}$  and  $\text{Zr}^{4+}$  ( $\text{Ti}^{4+}$ ) and the ionic radius is similar, it can form a replacement solid solution. When the additive is different from  $\text{Pb}^{2+}$  and  $\text{Zr}^{4+}$ , it can form  $\text{A}^{1+}\text{B}^{5+}\text{O}_3$  or  $\text{A}^{2+}\text{B}^{3+}\text{O}_3$  type compounds. In addition, PZT ceramics are usually sintered by  $\text{Pb}_3\text{O}_4$ ,  $\text{TiO}_2$ ,  $\text{ZrO}_2$  and a small amount of additives at high temperature.<sup>183–185</sup> Furthermore, PZT has a very wide range of applications. It can be used in ultrasonic transducers, underwater acoustic transducers, ceramic transformers, electroacoustic devices and pyroelectric detectors.<sup>186,187</sup> In particular, as a transparent ferroelectric material, PZT can also be used in photoelectric switches, image recognition, image display, photosensitive imaging, *etc.*<sup>188</sup> It also has obvious application advantages in RS devices.

Daniel Pantel *et al.* confirmed that the ferroelectric polarization direction and resistance state are closely related in the ferroelectric  $\text{Pb}(\text{Zr}_{0.2}\text{Ti}_{0.8})\text{O}_3$  (PZT) based RS devices prepared by the self-assembly method.<sup>189</sup> The preparation process of the metal-ferroelectric-metal (MFM) structure is sketched in Fig. 18a. Fig. 18b shows the perfect self-assembly of the spheres on the PZT surface into a single layer after metal deposition. At the same time, ordered metal nanostructures can be obtained by dissolving latex nanospheres in dichloromethane (Fig. 18c). In the test of the as-prepared ferroelectric nonvolatile memory device, a high resistance ratio of 1500 was obtained. In addition, Christoph Baeumer *et al.* proved that the degree of graphene doping and ferroelectric polarization have a two-way interdependence in the graphene/ $\text{PbZr}_{0.2}\text{Ti}_{0.8}\text{O}_3$  hybrid structure-based RS device,<sup>190</sup> as shown in Fig. 18d. In particular, the memory device prepared by using graphene/ $\text{PbZr}_{0.2}\text{Ti}_{0.8}\text{O}_3$  as the functional layer has good non-volatility, so it can be used for non-volatile memory. This indicates that the doping of graphene can promote the reversible ferroelectric polarization of the PZT film, and the ferroelectric polarization of the PZT film can in turn control the type and density of carriers in the graphene.<sup>190</sup> Therefore, it can be concluded from the above research works that perovskite-type PZT materials can be used in the preparation of RS devices for information memory applications. PZT is further expected to be prepared into a new type of multifunctional electronic device because it has multiple characteristics of piezoelectricity, ferroelectricity, transparency, *etc.*

### 3.2 The involved main mechanisms

It is well known that for any new physical phenomenon to be put into practical application a clear understanding of its mechanism is essential. The mechanism of the RS effect is

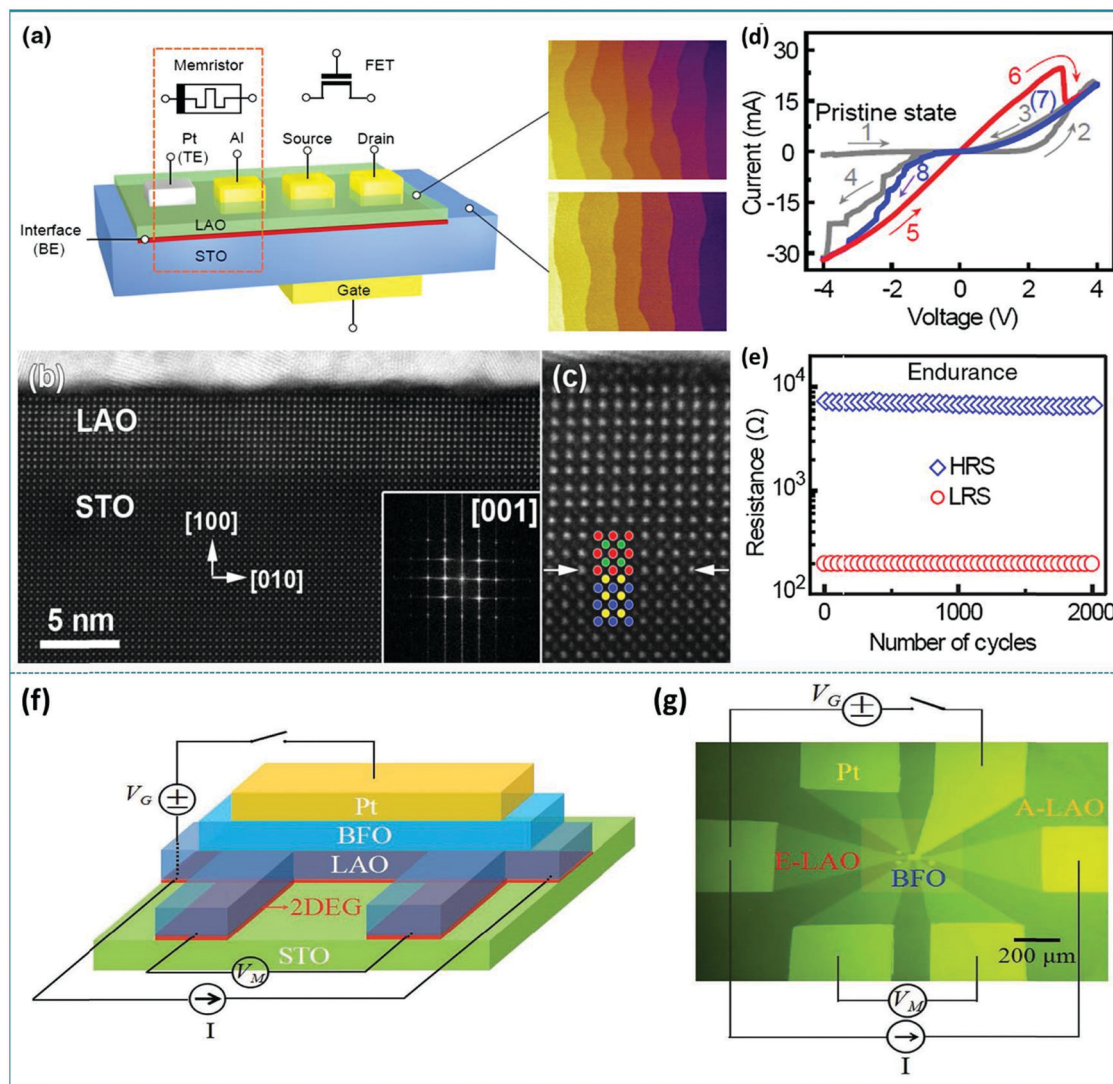


**Fig. 17** (a) Proposed scheme of integrating both the high performance memristor and FET at the oxide interfaces; (b) high-resolution high-angle annular dark-field scanning transmission-electron-microscopy (HAADF-STEM) images of a Pt/LAO/STO heterostructure; (c) high-resolution image of the LAO/STO interface, which is marked by arrows; (d) forming process (voltage sweeps 1–4) transforms the device into the switchable states (sweeps 5–8); the red and the blue lines represent the LRS and HRS, respectively, and the arrows mark the directions of the sweeping voltage; (e) the endurance data with a readout voltage of 0.2 V. Panels a–e reproduced with permission.<sup>172</sup> Copyright 2013, American Physical Society. (f) Schematic of the Pt/BFO/LAO/STO heterostructure; (g) the optical image of the Pt/BFO/LAO/STO structure and measurement. Panels f–g reproduced with permission.<sup>173</sup> Copyright 2018, Wiley-VCH.

often related to the formation of conductive filaments, the generation of Schottky barriers, the redox reaction of metal ions, ferroelectric polarization, *etc.*<sup>71–75</sup> However, the mechanisms of RS effects are often different due to the diverse material selection. Firstly, to understand the mechanism of the RS effect based on ABO<sub>3</sub>-type multiferroic perovskite materials, Sahwan Hong *et al.* proposed the switchable Schottky-to-Ohmic interfacial contacts between electrodes and BiFeO<sub>3</sub> nano-islands in a RS device with Pt/BiFeO<sub>3</sub>/SrRuO<sub>3</sub> structure.<sup>71</sup> The diagram of the physical mechanism is shown in Fig. 19a. It mainly explains the reversible change of the resistance states between HRS and LRS through the reversible transition of the interface barrier caused by the ferroelectric polarization reversal of the BiFeO<sub>3</sub> layer under an external bias, and the mechanism agrees very

well with the experimental data. Similar to the above report, Wanqiong Dai *et al.* explained the observed RS behavior in the La<sub>0.1</sub>Bi<sub>0.9</sub>FeO<sub>3</sub>/Nb-doped SrTiO<sub>3</sub> (LBFO/NSTO) heterostructure by using the influence of ferroelectric polarization on the width of the depletion region and the modulation effect of the Schottky barrier height of the LBFO/NSTO interface,<sup>191</sup> as shown in Fig. 19b. When a positive voltage pulse is applied to the Pt top electrode of the RS device, the polarization direction of the functional layer film is downward, and the generated positive electrode charge will be accumulated near the interface of the ferroelectric layer, thereby reducing the width of the depletion layer. When a negative voltage pulse is applied to the Pt top electrode of the RS device, a large number of carriers in the n-type semiconductor NSTO will be repelled by the

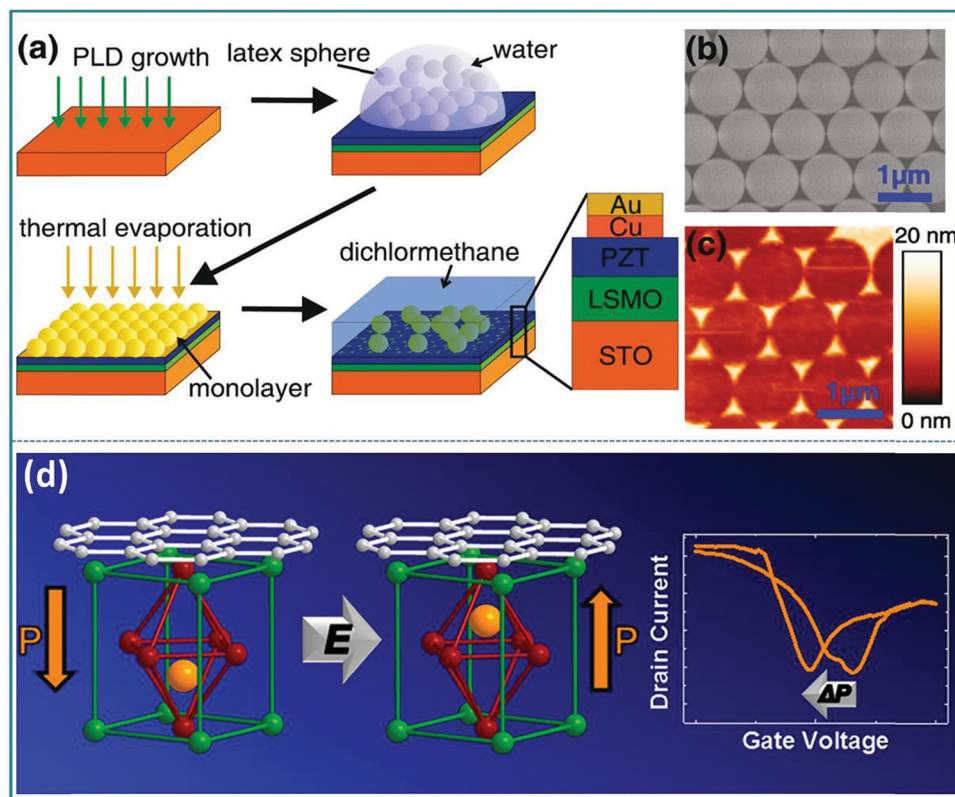


**Fig. 18** (a) Schematic of the nanosphere lithography (NSL) process adapted for nanoscale electrode preparation on PZT surfaces; (b) SEM image of a hexagonally close packed monolayer of polystyrene spheres; (c) the resulting Au-capped Cu nanoislands (by AFM) on top of a PZT surface. Panels a–c reproduced with permission.<sup>189</sup> Copyright 2011, American Chemical Society. (d) Tunable carrier type and density in graphene/PbZr<sub>0.2</sub>Ti<sub>0.8</sub>O<sub>3</sub> hybrid structures through ferroelectric switching. Reproduced with permission.<sup>190</sup> Copyright 2013, American Chemical Society.

negatively polarized accumulated charge, so that it can significantly increase the width of the depletion layer. Therefore, this work proves that it is possible to control the RS effect by adjusting the depletion width of the ferroelectric layer interface through ferroelectric polarization. Further, Lei Jin *et al.* attributed the variation in trap characteristics to changes in polarization ordering and trap densities, which were caused by the release of polarization domains and the generation of oxygen vacancies during the operation of the Au/BiFeO<sub>3</sub>/SrRuO<sub>3</sub> device.<sup>192</sup> As shown in Fig. 19c, most of the traps are empty at the beginning, leading to the device exhibit a low conductivity, which corresponds to HRS of the device. When a negative bias is applied on the top electrode of the device, the electrons can be captured by trap centers according to semiconductor theory. Thus, the Schottky barrier at the Au/BiFeO<sub>3</sub> interface is lowered, and hence, this device exhibits a highly conductive behavior and the resistance state is switched from HRS to LRS. Subsequently, the trapped carriers still remain after the applied bias is removed, so the LRS can be retained until a positive bias is applied to switch the Au/BiFeO<sub>3</sub>/SrRuO<sub>3</sub> device from LRS to HRS. In this way, this device can continuously complete the information processing between two resistance states (HRS and LRS) under an applied bias.

Moreover, Tiangui You *et al.* established a modifiable Schottky barrier height model in a BiFeO<sub>3</sub> memristor with

abundant movable oxygen vacancies, and further clarified the physical mechanism of RS memory.<sup>193</sup> As shown in Fig. 19d, the mechanism of the RS effect can be explained by adjusting the Schottky barrier of the BiFeO<sub>3</sub>/Pt interface, which means that the height of the Schottky barrier of the interface can be adjusted by applying an electric field to adjust the drift of the oxygen vacancies ( $V_o^{2+}$ ). Under the adjusted bias pulses,  $V_o^{2+}$  can act as a mobile donor and  $Ti^{4+}$  can act as a fixed donor in the BiFeO<sub>3</sub> functional layer. Therefore, the RS behavior can be continuously configured by adjusting the amplitude and length of the applied bias pulse, which makes it possible to achieve multilevel memory logic and improve the switching speed. Chandni Kumari *et al.* used a low-cost process to fabricate a resistive random access memory (RRAM) device based on BiFeO<sub>3</sub>, and further studied the influence of the Al top electrode on the RS characteristic and reliability.<sup>194</sup> The switching mechanism was clarified by the formation and fracture of oxygen vacancy conductive filaments and the participation of the AlO<sub>x</sub> thin layer on the Al/BiFeO<sub>3</sub> interface, as shown in Fig. 19e. It should be known that the conductive filament mechanism is a very recognized mechanism of the RS effect. It is rarely limited to the type of functional material, and has a very close relationship with the type of electrode material. Finally, we should mention that M. J. Han fabricated a RS device based on high-density self-assembled BiFeO<sub>3</sub> nano-islands grown



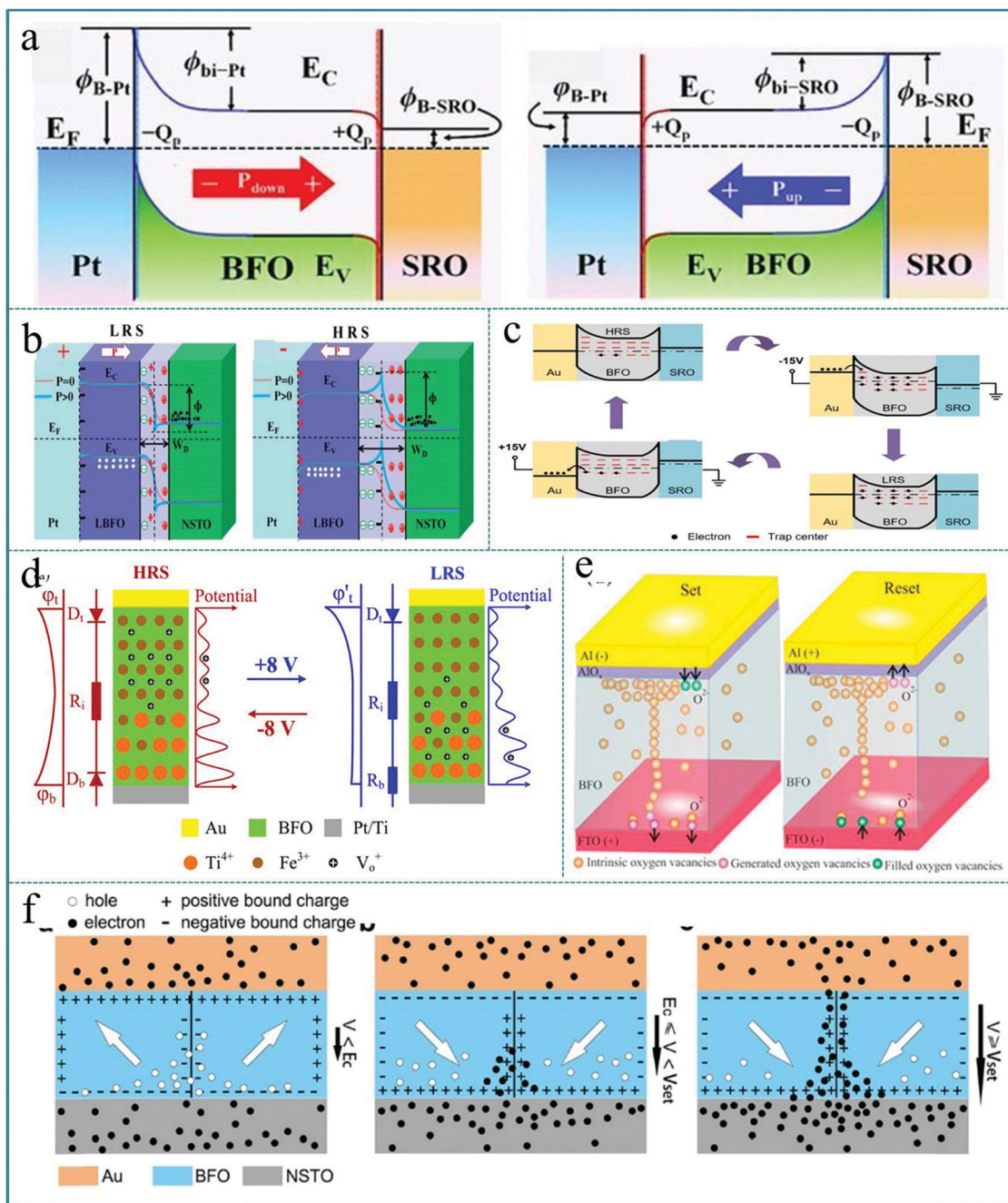


**Fig. 19** (a) Schematics of energy band diagrams of the Schottky-to-Ohmic interfacial contacts in Pt/BiFeO<sub>3</sub>/SrRuO<sub>3</sub> modulated by polarization orientations. Reproduced with permission.<sup>71</sup> Copyright 2013, Wiley-VCH. (b) Schematic of energy band diagrams of the Pt/La<sub>0.1</sub>Bi<sub>0.9</sub>FeO<sub>3</sub>/Nb-doped SrTiO<sub>3</sub> heterostructure at LRS and HRS. Reproduced with permission.<sup>191</sup> Copyright 2020, Royal Society of Chemistry. (c) Filling status of traps and the band diagram at the initial state of the device, negative voltage  $-15.0$  V (applied),  $-15.0$  V (removed), and  $+15.0$  V (applied). Reproduced with permission.<sup>192</sup> Copyright 2020 Elsevier. (d) Schematic representation of the distribution of mobile  $V_o^+$  (black circles) and fixed  $Ti^{4+}$  (orange circles) donors in the BiFeO<sub>3</sub> thin film for HRS and LRS. Reproduced with permission.<sup>193</sup> Copyright 2014, American Chemical Society. (e) Schematic of the AlO<sub>x</sub> assisted filament formation mechanism for set and reset states in Al/BiFeO<sub>3</sub>/FTO RRAM devices. Reproduced with permission.<sup>194</sup> Copyright 2020, AIP Publishing. (f) Schematics showing the charged domain wall mediated RS mechanism of Au/BiFeO<sub>3</sub>/Nb-doped SrTiO<sub>3</sub> heterojunctions. Reproduced with permission.<sup>195</sup> Copyright 2020, Elsevier.

on a Nb doped SrTiO<sub>3</sub> (0.7 wt%) (NSTO) substrate.<sup>195</sup> The RS property was induced by the formation and rupture of the conductive filament at the charged domain wall due to the change of charge carrier concentrations under the applied voltage.

Fig. 19f shows a schematic diagram of the charge distribution in a charged domain wall under different applied voltages. In this device, the NSTO substrate is an n-type semiconductor, which makes the electrons here as carriers. In this way, a large number

of electron carriers from the NSTO substrate will be effectively accumulated on the head-to-head charged domain wall. Therefore, this research provides us with a new way to improve the RS performance by adjusting the charged domain wall. In fact, because ferroelectric materials contain a large number of spontaneously polarized ferroelectric domains, the effect of the domain wall on nano-devices will stimulate new ideas in the construction of nanoscale electronic devices in future.

Anyway, the physical mechanism of the RS effect is currently inconclusive. In other words, there is no mechanism that can fully and profoundly explain all the observed RS behaviors.<sup>196–198</sup> Certainly, the RS mechanism of ABO<sub>3</sub> type multiferroic perovskite materials is still under extensive exploration. In the above discussion, we have only listed a few typical mechanisms. Therefore, in future research, the physical mechanism of the RS device is still a focus that needs to be further studied.<sup>199,200</sup>

#### 4. ABO<sub>3</sub> memristor-based synaptic device for neuromorphic computing

A synaptic device is an electrical device that can simulate the function of neurons for information transmission. According to the device structure, synaptic devices can be divided into synaptic transistors and synaptic memristors. Recently, the research of synaptic devices based on the memristive effect has received extensive attention. Neurons are the basic building blocks of the human brain, and synapse is the key part of transmitting information between neurons. Therefore, if we can develop electronic components with similar functions to biological synapses, it will be of great significance to realize artificial intelligence. Among all the known circuit elements, the memristor is a non-linear resistance device with information memory function, which has similar characteristics to the biological nerve synapse with nanometer size. Therefore, the memristive unit is one of the ideal electronic devices to realize synaptic function.<sup>201,202</sup> In the study of synaptic devices based on memristors, Sören Boyn *et al.* reported a synapse device based on ferroelectric tunnel heterojunctions and observed the spike-timing-dependent plasticity (STDP).<sup>203</sup> Among them, synaptic strength can be characterized through STDP based on the time and dependence of the electrical signals of neighboring neurons. Fig. 20a shows a memristive device with Pt/Co/BiFeO<sub>3</sub>/(Ca,Ce)MnO<sub>3</sub>/YAlO<sub>3</sub> (Pt/Co/BFO/CCMO/YAO) multilayer structure, and the resistance of the device strongly depends on the relative fraction of ferroelectric domains. In order to construct a neural network using the as-prepared sandwich memristive unit, the simulated neural network was built using a crossbar array of 9 × 5 ferroelectric memristors (Fig. 20b). In a typical crossbar structure, each cross section represents a device unit. Using this method, neural networks can be constructed. Fig. 20c shows that the image recognition rate of the neural network increases with the increase of the number of image presentations, reaching almost 100% for low noise levels and nearly 80% for high noise levels. These experimental results lay the experimental foundation for the realization of low-power

hardware for billions of reliable and predictable artificial synapses (such as deep neural networks) in artificial brain-based computers in the future,<sup>204,205</sup> which can be effectively applied to the intelligent recognition of images and information.

In recent research, Lei Liu *et al.* mimicked some biological synaptic functions based on a Pt/BiFeO<sub>3</sub>/HfO<sub>2</sub>/TiN memristor with an RS area of  $\sim 1.0 \times 1.0 \mu\text{m}^2$ .<sup>206</sup> Fig. 20d shows a stable bipolar RS behavior of HfO<sub>2</sub>-based memristors with and without the BiFeO<sub>3</sub> inserted layer. It is obvious that an enlarged resistance window can be achieved by adding the BiFeO<sub>3</sub> inserted layer into the functional layer. Fig. 20e schematically illustrates the similar synapse structure and transmission characteristic of a memristor. Indeed, the biosynaptic weight reflects the connection strength of neurons, which can be represented by the conductance or resistance of the memristor.<sup>207</sup> As shown in Fig. 20f, the conductance of the memristive device can be adjusted periodically by applying a voltage pulse, which is similar to the information transmission characteristic of a synapse. It is feasible to simulate the function of bio-synapse by adjusting the conductance of the memristor. This device can be applied to wearable systems and biomedical equipment. Therefore, this work proves that Pt/BiFeO<sub>3</sub>/HfO<sub>2</sub>/TiN memristors have potential applications in neuromorphic computing and artificial intelligence systems, opening up a new way for the integration of neural networks. Finally, it should be noted that Venkata Raveendra Nallagatla *et al.* studied the RS effect of the epitaxial brownmillerite SrFeO<sub>2.5</sub> (BM-SrFeO<sub>2.5</sub>) thin film by systematically controlling the oxygen concentration to realize synaptic learning.<sup>208</sup> This synaptic device exhibited either bipolar RS or complementary RS behaviors. Fig. 20g shows the synaptic device with Au/BM-SrFeO<sub>2.5</sub> (111)/SrRuO<sub>3</sub>/SrTiO<sub>3</sub> (111) structure which has out-of-plane-oriented oxygen-vacancy channels with the BM-SrFeO<sub>2.5</sub> insulating layer. The typical *I*-*V* curves are shown in Fig. 20h, indicating a low-power bipolar RS property under a current compliance (CC) of 10  $\mu\text{A}$  in the negative voltage region; the arrows in the figure indicate the direction of the applied voltage sweeps. The retention testing is shown in the inset of Fig. 20h, which presents a large switching window accompanied by a weak attenuation. This result implies that the RS device can be used in information processing and memory technology. Fig. 20i displays a schematic diagram of a bio-synapse, and the SrFeO<sub>x</sub>(111) RS device can be used to simulate the synaptic function. Fig. 20j shows the *I*-*V* curves under consecutive negative voltage sweeps (blue lines) and positive voltage sweeps (orange lines, after the negative voltage sweeps). Fig. 20k shows that the current of the RS device can be gradually increased by a consecutive potentiating electric pulse of  $-4.0 \text{ V ms}^{-1}$  and decreased by a depressing electric pulse of  $5.0 \text{ V ms}^{-1}$  under a read voltage of 0.5 V, indicating that the RS device can be useful for synaptic operations in smart applications.

Therefore, it can be confirmed that the memristor unit is an effective component to realize artificial intelligence hardware.<sup>209</sup> In the brain, the basic law of biological memory and learning is synaptic plasticity. Artificial synaptic devices are required to achieve synaptic weight adjustment with good stability and repeatability under appropriate excitability and pulse stimulation.



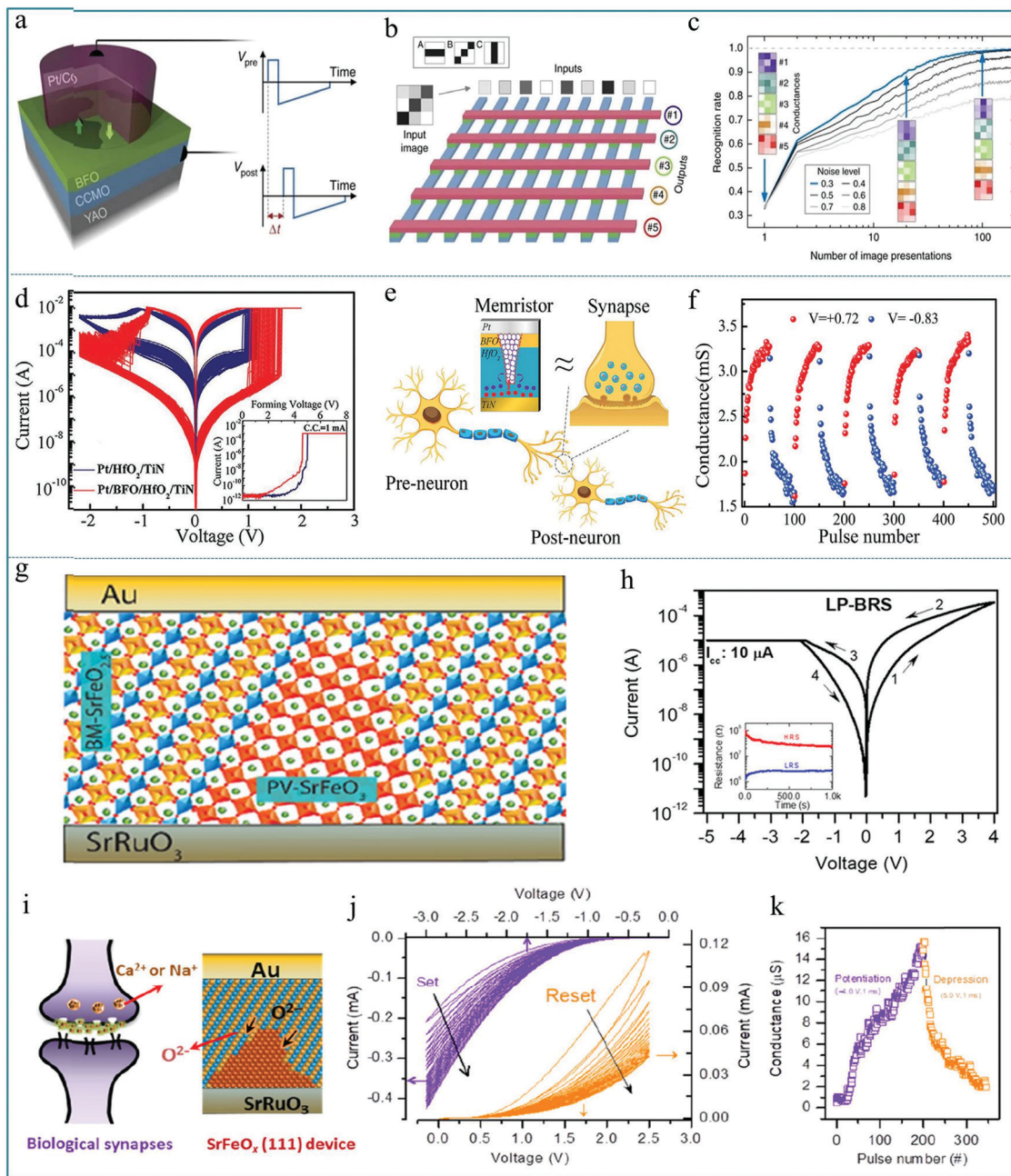


**Fig. 20** (a) Sketch of the ferroelectric memristor where a ferroelectric tunnel barrier of BiFeO<sub>3</sub> (BFO) is sandwiched between the bottom electrode of (Ca,Ce)MnO<sub>3</sub> (CCMO) and the top submicron pillar of Pt/Co, and YAO stands for YAlO<sub>3</sub>; (b) simulated spiking neural network comprising nine input neurons connected to five output neurons by an array of ferroelectric memristors, in which the inputs are noisy images of the patterns to be recognized: horizontal (A), diagonal (B) and vertical (C) bars in 3 × 3 pixel images; (c) recognition rate as a function of the number of presented images for different noise levels, in which the colored images are conductance maps of the memristors in each line and show their evolution for a noise level of 0.3 (blue line). Panels a–c reproduced with permission.<sup>203</sup> Copyright 2016, Nature Publishing Group. (d) 100 continuous *I*–*V* curves for HfO<sub>2</sub>-based memristors with and without the BiFeO<sub>3</sub> layer, and the inset shows the forming process. (e) Schematic diagram of the brain neural network and a Pt/BiFeO<sub>3</sub>/HfO<sub>2</sub>/TiN synaptic memristor; (f) the reproducible conductance modulation under repeated potentiation and depression pulses to mimic the change of synaptic weight in the biological synapse. Panels d–f reproduced with permission.<sup>206</sup> Copyright 2020, Wiley-VCH. (g) Schematic representation of the Au/BM-SrFeO<sub>2.5</sub> (111)/SrRuO<sub>3</sub>/SrTiO<sub>3</sub> (111) device with the PV-SrFeO<sub>3</sub> conductive path; (h) typical *I*–*V* curves of the device; (i) schematic representation of the bio-synapse and the conductive path formation. (j) *I*–*V* curves under consecutive negative voltage sweeps (blue lines) and positive voltage sweeps (orange lines, after the negative voltage sweeps). (k) Current in the synaptic device was gradually increased and decreased under the read voltage of 0.5 V. Panels g–k reproduced with permission.<sup>208</sup> Copyright 2020, American Chemical Society.

The condition for simulating the plasticity of biological nerve synapses is that the conductance (or resistance) of the artificial

synaptic device can be continuously adjusted. The resistance of the memristor can be changed with the amount of charge flowing



through it, and the resistance can be maintained after power failure state, so the memristor is considered to be an ideal device to simulate nerve synapses.<sup>210,211</sup> The synaptic devices reported so far are based on the principle of oxygen vacancy migration to realize the time-dependent synaptic plasticity (STDP) function of neuronal electrical pulse activity.<sup>212,213</sup> Therefore, the effect of this sequence of synaptic activity on synaptic information transmission is considered to be directly related to brain learning and memory functions.

Actually, neuromorphic computing is a process that mimics the information processing at biological synapses. The neuromorphic computing can realize high-efficiency massive parallel computing

to conquer the limitation of the Von Neumann bottleneck.<sup>214–219</sup> The physical mechanism of neuromorphic computing is based on the ion transport at the device interface to achieve efficient transfer and computation of information at the same location,<sup>220</sup> which is different from the logic circuit in digital systems.<sup>221</sup> Besides, neuromorphic computing is characterized by distributed memory and computational elements.<sup>222</sup> For the research and application of memristive devices, neuromorphic computing is a necessary step for memristors to be applied to artificial intelligence.<sup>223</sup> Many recent studies have effectively proved that the use of memristors in neuromorphic computing has practical significance and research foundation.<sup>224</sup>

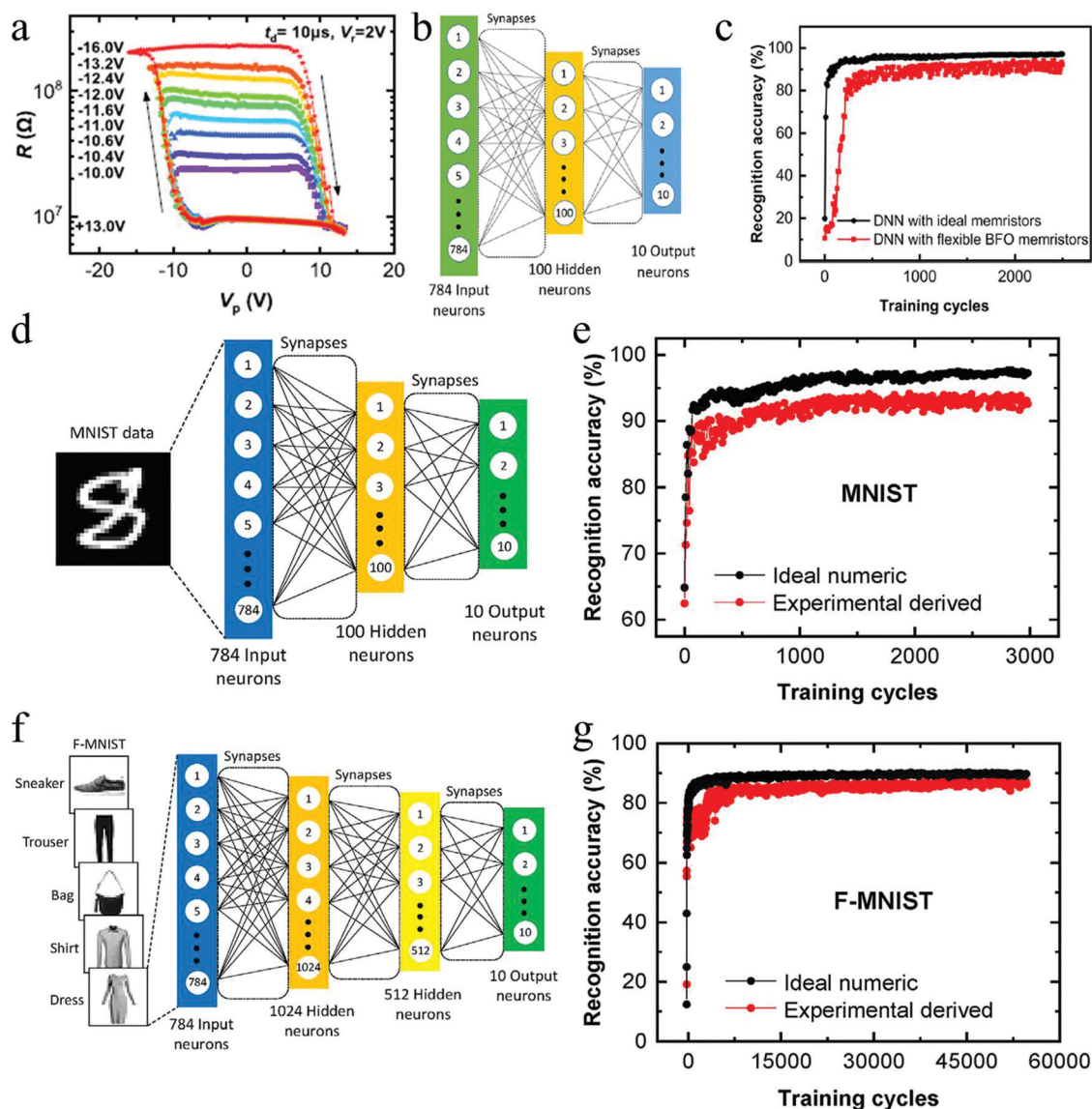


**Fig. 21** (a) Resistances as a function of  $V_p$  with  $t_d = 10 \mu s$ , in which the arrows indicate the sweeping directions of  $V_p$ ; (b) schematic diagram of a two-layer perceptron neural network; (c) simulation results based on the realistic device behavioral model and ideal synaptic devices. Panels a–c reproduced with permission.<sup>228</sup> Copyright 2020, American Chemical Society. (d) Schematic diagram of a two-layer perceptron neural network ( $784 \times 100 \times 10$ ) trained to clarify the  $28 \times 28$  MNIST pixel handwritten digits, and (e) the corresponding recognition accuracies for experimental and ideal synaptic devices; (f) schematic diagram of a three-layer neural network ( $784 \times 1024 \times 512 \times 10$ ) trained to clarify the  $28 \times 28$  FMNIST pixel images, and (g) the corresponding recognition accuracies based on experimental and ideal synaptic devices. Panels d–g reproduced with permission.<sup>230</sup> Copyright 2021, Elsevier.

In previous reports, it has been proved that the  $\text{BiFeO}_3$  single-crystal orientation films can be successfully prepared using appropriate technical means.<sup>225–227</sup> Haoyang Sun grew high-quality (111)-oriented  $\text{BiFeO}_3$  ferroelectric films on flexible mica substrates with  $\text{SrRuO}_3/\text{BaTiO}_3$  double buffer layers, and a ferroelectric memristive behavior with continuously tunable resistance states was observed.<sup>228</sup> The  $\text{BaTiO}_3$ ,  $\text{SrRuO}_3$ , and  $\text{BiFeO}_3$  films have a quasi-hexagonal structure. As shown in Fig. 21a, with the pulse duration  $t_d = 10 \mu\text{s}$ , the memristor is set to the LRS by an applied voltage of +13.0 V or the HRS by an applied voltage of –16.0 V. Then, using the as-prepared memristor device, a two-layer perceptron with 784 input neurons, 100 hidden neurons, and 10 output neurons was simulated, as shown in Fig. 21b. Fig. 21c shows the deep neural network (DNN) with a flexible  $\text{BiFeO}_3$  memristor, which can reach a pattern recognition accuracy of  $\sim 90\%$  after 1500 training cycles. Therefore, this study shows that it is feasible to prepare high-quality multiferroic perovskite films on flexible substrates. It also confirms that the flexible ferroelectric memristive devices have obvious advantages in non-volatile information processing and neuromorphic computing in advanced artificial intelligence systems.<sup>229</sup> Haoyang Sun *et al.* used an ultra-thin  $\text{BiFeO}_3$  ferroelectric barrier layer, a  $\text{ZnO}$  semiconductor layer and a  $\text{SrRuO}_3$  electrode to prepare a flexible ferroelectric tunnel junction (FTJ) memristor, and found that the FTJ memristor shows multistable memory behavior.<sup>230</sup> In this study, a perceptron neural network ( $784 \times 100 \times 10$ ) was constructed to recognize Modified National Institute of Standard and Technology (MNIST) handwritten digits, as shown in Fig. 21d. After 3000 training cycles, a high recognition accuracy of 92.8% can be achieved using this neural network (Fig. 21e). In addition to the two-layer artificial neural network that can be used to recognize handwritten digits, they further built a more complex three-layer perceptron neural network ( $784 \times 1024 \times 512 \times 10$ ) to recognize the Fashion-MNIST (F-MNIST) image dataset as shown in Fig. 21f. After 55 000 cycles, the neural network can still achieve an image recognition accuracy of 86.2%, as shown in Fig. 21g. This research may provide a new path for the development of nonvolatile memory and neuromorphic computing systems based on flexible FTJ memristors.

Furthermore, Yihao Yang *et al.* demonstrated a memristive ferroelectric tunnel junction (FTJ) synapse based on the multiferroic  $\text{BaTiO}_3/\text{CoFe}_2\text{O}_4$  composite.<sup>231</sup> Fig. 22a shows the schematic of the  $(\text{La}_{0.67}, \text{Sr}_{0.33})\text{MnO}_3$  (LSMO)/ $\text{BaTiO}_3$  (BTO)/ $\text{CoFe}_2\text{O}_4$  (CFO)/Nb:SrTiO<sub>3</sub> (Nb:STO) FTJ device. Fig. 22b shows the schematic of the piezoresponse force microscopy (PFM) measurements, in which the arrows inside the BTO layer represent polarizations. Fig. 22c shows that one can implement the neuromorphic computing by constructing a cross-node neural network based on the spin filter LSMO/BTO/CFO/Nb:STO memristive FTJ as an artificial synaptic unit, thereby realizing the long-term plasticity of each node of the brain-inspired intelligent recognition. Therefore, the memristive FTJ device provides a new approach toward neuromorphic computing with energy-efficiency, which further expands the broad scope of applications. Moreover, Rao *et al.* used epitaxy to prepare a high crystallinity  $\text{SrFeO}_x$  heterojunction and characterized the memristive

properties of the  $\text{Au}/\text{SrFeO}_x/\text{SrRuO}_3$  device.<sup>232</sup> Fig. 22d shows the schematic of a conductive filament induced RS device consisting of a brownmillerite  $\text{SrFeO}_{2.5}$  (BM-SFO) matrix and a perovskite  $\text{SrFeO}_3$  (PV-SFO) conductive filament, and Fig. 22e shows an interface effect induced RS device consisting of a PV-SFO matrix and a BM-SFO interfacial layer. The hysteresis-type  $I$ - $V$  characteristics are shown in Fig. 22f and g, in which it can be found that the RS effect induced by the conductive filament has a more obvious SET and RESET process, and it is usually accompanied by a larger HRS/LRS resistance ratio. In this work, they found that the  $\text{SrFeO}_x$  based memristive device exhibits an excellent synaptic function, which can be used to construct neuromorphic computing circuits.<sup>232</sup> Fig. 22h and i presents a simulation diagram of a three-layer neural network with a crossbar consisting of  $\text{SrFeO}_x$ -based synaptic memristors, which can effectively recognize images with accuracies of  $\sim 88\%$ , indicating that  $\text{SrFeO}_x$ -based synaptic memristors as building blocks have important potential applications in neuromorphic computing circuits.

## 5. Summary and outlook

Table 1 exhibits the comparison results of the typical  $\text{ABO}_3$ -based memristive devices in terms of the switching function layer, electrode schedule, cycling endurance, retention time, HRS/LRS ratio, and energy consumption. Among these features, the cycling endurance exceeds  $10^7$  for the  $\text{SrFeO}_x$ -based memristive device with  $\sim \text{pJ}$  energy consumption. Importantly, the oxygen-rich stoichiometry of  $\text{ABO}_3$  endows the memristor with a variety of RS behaviors to faithfully mimic the neuron networks. Electrode engineering as one of the most efficient methods to obtain the target RS behavior such as the binary, electron-type, and analog RS behavior was extensively investigated for application in T bits data storage and neuromorphic computing.<sup>233</sup> Although great progress has been made in  $\text{ABO}_3$ -based memristors in recent years, the sneak current issue has not been overcome because of the lack of an ideal  $\text{ABO}_3$  memristive cell. One possible solution is optimizing the preparation methods to develop a self-rectification  $\text{ABO}_3$ -based memristor or integrate the stable  $\text{ABO}_3$ -based memristor with back-to-back diodes to enlarge the memristor crossbar array.

The  $\text{ABO}_3$ -based memristor array has shown high capability in operating the convolutional neural network (CNN), which has been extensively applied in image processing, language recognition, automatic driving, and so on.<sup>234–237</sup> The  $\text{ABO}_3$ -based memristor array has shown great potential application in neuromorphic computing,<sup>238–242</sup> but the insufficient hashrate is also a bottleneck for complicated applications. One solution is constructing an analog-type  $\text{ABO}_3$ -based memristor with high precision and developing ultrahigh scale integration technologies (*i.e.*, nano imprint, directed self-assembly, DSA) to improve the capability of parallel computing.<sup>243–247</sup> Fig. 23 schematically demonstrates the  $\text{ABO}_3$ -based materials including  $\text{BiFeO}_3$ ,  $\text{BaTiO}_3$ ,  $\text{SrRuO}_3$ ,  $\text{LaMnO}_3$ , and  $\text{AlFeO}_3$  for the internal dynamic process to faithfully mimic our human brain. By constructing a

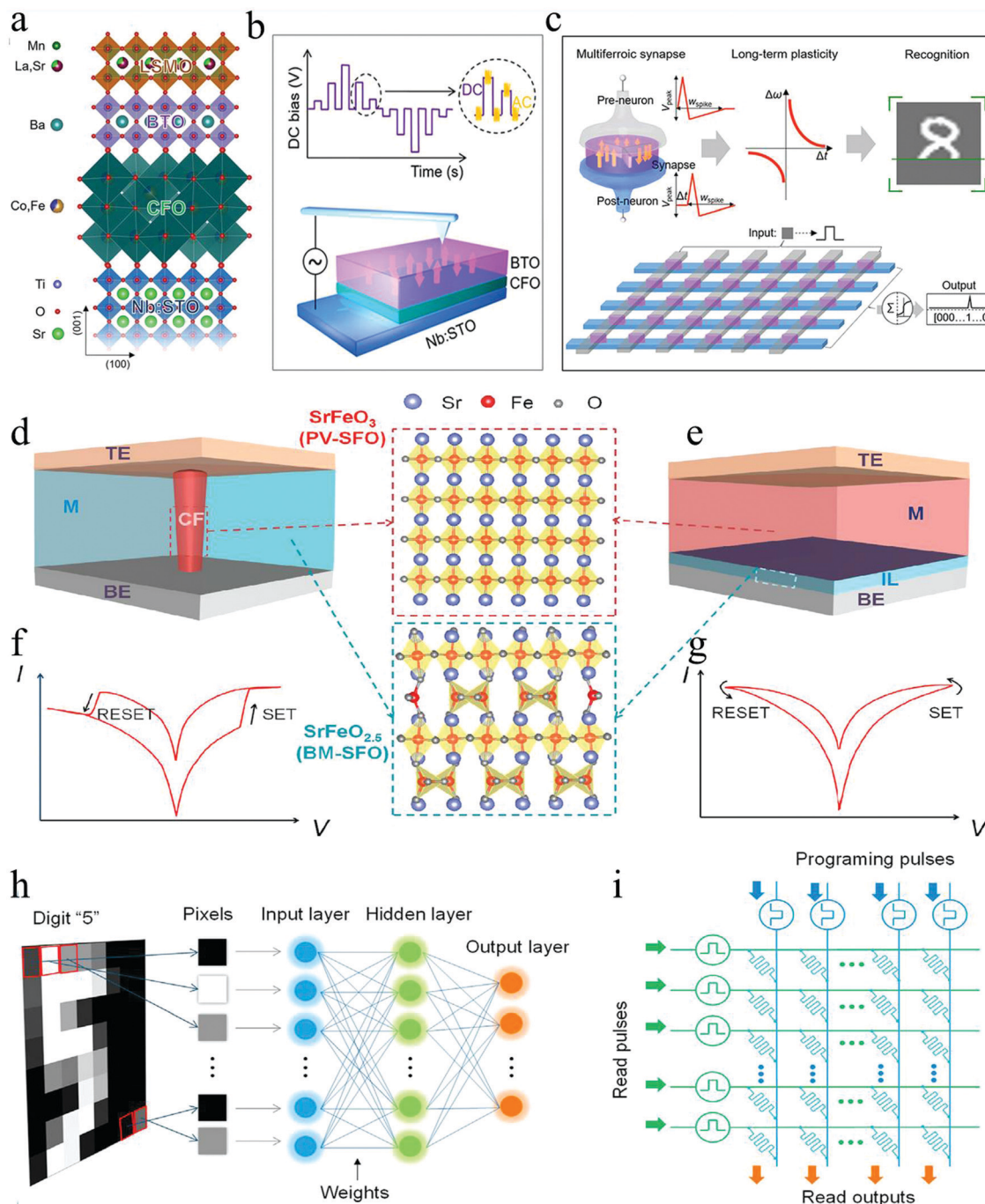


Fig. 22 (a) Schematic of the LSMO/BTO/CFO/Nb:STO FTJ; (b) schematic of the PFM measurements, in which the arrows inside the BTO layer represent polarizations; (c) schematic of the neuron simulation from long-term plasticity of the LSMO/BTO/CFO/Nb:STO multiferroic synapses to the recognition functionality in a crossbar network. Panels a–c reproduced with permission.<sup>231</sup> Copyright 2020, American Chemical Society. (d–g) Schematic of the different RS device structures and *I*–*V* characteristics; (h) schematic of a three layer neural network; (i) a crossbar consisting of SrFeO<sub>x</sub>-based synapses. Panels d–i reproduced with permission.<sup>232</sup> Copyright 2021, Elsevier.

large scale ABO<sub>3</sub>-based memristor array, the ABO<sub>3</sub>-based memristor array enables the high efficiency neuromorphic computing.

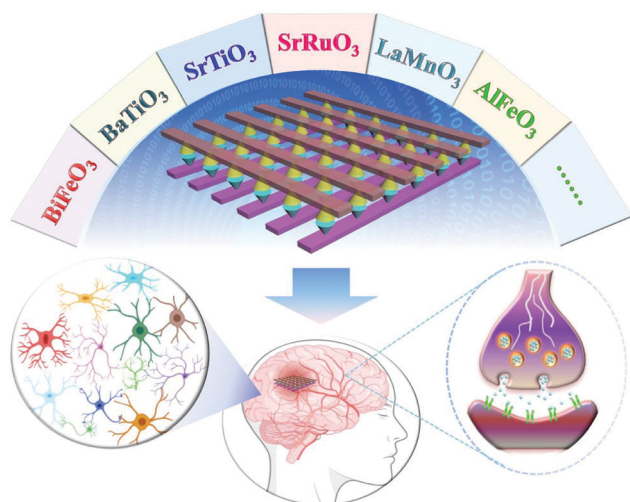
In addition, multiferroic perovskite materials also have potential for application in spintronic devices.<sup>248–252</sup> The interactive coupling of ferroelectric domains and magnetic domains makes electron spin more diversified. Besides, multiferroic

heterojunctions with both ferroelectric and ferromagnetic properties can achieve voltage-regulated magnetic properties or magnetic field-regulated ferroelectric properties through magnetoelectric coupling effects, which provides the possibility to generate spin currents. Therefore, the research of multiferroic perovskite materials in neuromorphic technology is



**Table 1** Comparison of the functional layer, top and bottom electrodes, endurance, retention, HRS/LRS ratio, and energy consumption of some representative ABO<sub>3</sub> multiferroic perovskite-based RS devices

Functional layer	Top electrode	Bottom electrode	Endurance (cycles)	Retention (s)	HRS/LRS ratio	Energy consumption	Ref.
BiFeO <sub>3</sub>	Pt	SrRuO <sub>3</sub>	—	10 <sup>3</sup>	753	—	71
BiFeO <sub>3</sub>	SrRuO <sub>3</sub>	Nb-Doped SrTiO <sub>3</sub>	15	—	593	—	72
BiFeO <sub>3</sub>	Pt	SrRuO <sub>3</sub>	24	6 × 10 <sup>3</sup>	10 <sup>3</sup>	—	77
Co-Doped BaTiO <sub>3</sub>	Au	Pt	1 × 10 <sup>5</sup>	7 × 10 <sup>4</sup>	> 10 <sup>4</sup>	—	106
BaTiO <sub>3</sub>	Au	La <sub>0.75</sub> Sr <sub>0.25</sub> MnO <sub>3</sub>	—	—	~18	—	107
BaTiO <sub>3</sub>	Conductive cantilever of AFM	La <sub>0.7</sub> Sr <sub>0.3</sub> MnO <sub>3</sub>	—	—	—	—	119
Nb-Doped SrTiO <sub>3</sub>	Pt	Nb-Doped SrTiO <sub>3</sub>	36	—	—	—	137
LaAlO <sub>3</sub>	ITO	SrTiO <sub>3</sub>	2 × 10 <sup>3</sup>	4 × 10 <sup>4</sup>	~10 <sup>2</sup>	—	138
SrTiO <sub>3</sub>	Pt	Pt	—	—	—	—	139
Fe-Doped SrTiO <sub>3</sub>	Ag	Pt	2.5 × 10 <sup>3</sup>	—	~10 <sup>5</sup>	—	140
SrCoO <sub>x</sub>	Au	Nb-Doped SrTiO <sub>3</sub>	100	1 × 10 <sup>4</sup>	> 10 <sup>3</sup>	—	149
AlFeO <sub>3</sub>	Pt	Nb-Doped SrTiO <sub>3</sub>	1 × 10 <sup>4</sup>	1 × 10 <sup>4</sup>	~10 <sup>2</sup>	—	156
LaMnO <sub>3</sub>	Pt	Nb-Doped SrTiO <sub>3</sub>	50	—	~18	—	165
LaMnO <sub>3+δ</sub>	Conductive cantilever of AFM	Au	—	—	—	—	166
LaAlO <sub>3</sub>	Pt	SrTiO <sub>3</sub>	2 × 10 <sup>3</sup>	4.32 × 10 <sup>4</sup>	~10 <sup>2</sup>	—	172
BiFeO <sub>3</sub> /LaAlO <sub>3</sub>	Pt	SrTiO <sub>3</sub>	—	—	~10 <sup>2</sup>	—	173
BiFeO <sub>3</sub> /HfO <sub>2</sub>	Pt	TiN	100	1 × 10 <sup>4</sup>	~10 <sup>4</sup>	—	206
SrFeO <sub>2.5</sub>	Au	SrRuO <sub>3</sub>	1 × 10 <sup>3</sup>	—	> 10	—	208
SrFeO <sub>x</sub>	Au	SrRuO <sub>3</sub>	1 × 10 <sup>7</sup>	—	> 10	~0.24 pJ per spike	232

**Fig. 23** The development from ABO<sub>3</sub>-type multiferroic perovskite materials to artificial intelligence applications.

expected to produce new physical phenomena and advanced applications.

Finally, it should be noted that multiferroic perovskite materials can also be used in the field of catalysis.<sup>253–257</sup> For example, multiferroic perovskite type Bi<sub>5</sub>CoTi<sub>3</sub>O<sub>15</sub> exhibits high electrocatalytic efficiency due to the synergistic effect of electron spin and ferroelectric polarization.<sup>258</sup> Thus, multiferroic perovskite materials have a wide range of potential applications in materials science, physics, chemistry, electronics, informatics, and computer science. And, the all-round research on this multifunctional perovskite material is expected to explore its powerful functions for better serving scientific and technological requirements in interdisciplinary fields.<sup>259,260</sup>

In summary, we have discussed in detail the research progress of ABO<sub>3</sub> multiferroic perovskite materials in the preparation of memristive devices, the realization of synaptic devices, the

construction of neural networks, and neuromorphic computing. Because the ABO<sub>3</sub> multiferroic perovskite materials have unique electron spin, transfer, polarization, and coupling behaviors, they show a very potential application in multifunctional electronics when combining their advantages of multiferroic properties with the memristive effect. These devices have already laid a scientific foundation for the manufacture of spin-moment-based multistate memristive memory devices. This domain wall feature in multiferroic perovskite materials generally improves the mutual controllability of the memristive effect and the electron spin effect. Therefore, it is expected to play more important applications in computer science, electronics, biomedicine, *etc.*

## Author contributions

B. Sun drafted this review and made detailed revisions. G. Zhou and L. Sun polished up English writing and grammar correction. H. Zhao, Y. Chen, F. Yang, and Y. Zhao made some discussions. Q. Song gave some useful suggestions and guidance. All authors gave their approval to the final version of the manuscript.

## Conflicts of interest

The authors declare no conflict of interest.

## Acknowledgements

The authors gratefully acknowledge financial support from the National Natural Science Foundation of China (Grant No. 11774293), the Sichuan Science and Technology Program (Grant No. 2020YJ0086), and the Fundamental Research Funds for the Central Universities (Grant No. 2682021CX076).

## References

- J. G. Simmons and R. R. Verderber, *Proc. R. Soc. A*, 1967, **301**, 77–102.
- L. Chua, *IEEE Trans. Circuit Theory*, 1971, **18**, 507–519.
- D. B. Strukov, G. S. Snider, D. R. Stewart and R. S. Williams, *Nature*, 2008, **453**, 80–83.
- X. Chen, N. Wu, J. Strozier and A. Ignatiev, *Appl. Phys. Lett.*, 2006, **89**, 063507.
- J. Choi, S. Park, J. Lee, K. Hong, D.-H. Kim, C. W. Moon, G. D. Park, J. Suh, J. Hwang, S. Y. Kim, H. S. Jung, N.-G. Park, S. Han, K. T. Nam and H. W. Jang, *Adv. Mater.*, 2016, **28**, 6562–6567.
- X. Zhu, J. Lee and W. D. Lu, *Adv. Mater.*, 2017, **29**, 1700527.
- Y. Wang, Z. Lv, Q. Liao, H. Shan, J. Chen, Y. Zhou, L. Zhou, X. Chen, V. A. L. Roy, Z. Wang, Z. Xu, Y.-J. Zeng and S.-T. Han, *Adv. Mater.*, 2018, **30**, 1800327.
- J. Choi, Q. V. Le, K. Hong, C. W. Moon, J. S. Han, K. C. Kwon, P.-R. Cha, Y. Kwon, S. Y. Kim and H. W. Jang, *ACS Appl. Mater. Interfaces*, 2017, **9**, 30764–30771.
- X. Guan, W. Hu, M. A. Haque, N. Wei, Z. Liu, A. Chen and T. Wu, *Adv. Funct. Mater.*, 2018, **28**, 1704665.
- L. Chua, *Semicond. Sci. Technol.*, 2014, **29**, 104001.
- G. Zhou, B. Sun, X. Hu, L. Sun, Z. Zou, B. Xiao, W. Qiu, B. Wu, J. Li, J. Han, L. Liao, C. Xu, G. Xiao, L. Xiao, J. Cheng, S. Zheng, L. Wang, Q. Song and S. Duan, *Adv. Sci.*, 2021, **8**, 2003765.
- G. Zhou, Z. Ren, L. Wang, B. Sun, S. Duan and Q. Song, *Mater. Horiz.*, 2019, **6**, 1877–1882.
- B. Sun, Y. Chen, M. Xiao, G. Zhou, S. Ranjan, W. Hou, X. Zhu, Y. Zhao, S. A. T. Redfern and Y. N. Zhou, *Nano Lett.*, 2019, **19**, 6461–6465.
- B. Sun, G. Zhou, T. Guo, Y. N. Zhou and Y. A. Wu, *Nano Energy*, 2020, **75**, 104938.
- S. Ranjan, B. Sun, G. Zhou, Y. A. Wu, L. Wei and Y. N. Zhou, *ACS Appl. Nano Mater.*, 2020, **3**, 5045–5052.
- M. Hu, C. E. Graves, C. Li, Y. Li, N. Ge, E. Montgomery, N. Davila, H. Jiang, R. S. Williams, J. J. Yang, Q. Xia and J. P. Strachan, *Adv. Mater.*, 2018, **30**, 1705914.
- P. M. Sheridan, F. Cai, C. Du, W. Ma, Z. Zhang and W. D. Lu, *Nat. Nanotechnol.*, 2017, **12**, 784–789.
- X. Yan, J. Zhao, S. Liu, Z. Zhou, Q. Liu, J. Chen and X. Y. Liu, *Adv. Funct. Mater.*, 2018, **28**, 1705320.
- Z. Wang, S. Joshi, S. E. Savel'ev, H. Jiang, R. Midya, P. Lin, M. Hu, N. Ge, J. P. Strachan, Z. Li, Q. Wu, M. Barnell, G.-L. Li, H. L. Xin, R. S. Williams, Q. Xia and J. J. Yang, *Nat. Mater.*, 2017, **16**, 101–108.
- Y. Wang, Z. Zhang, M. Xu, Y. Yang, M. Ma, H. Li, J. Pei and L. Shi, *ACS Appl. Mater. Interfaces*, 2019, **11**, 24230–24240.
- I. Boybat, M. L. Gallo, S. R. Nandakumar, T. Moraitis, T. Parnell, T. Tuma, B. Rajendran, Y. Leblebici, A. Sebastian and E. Eleftheriou, *Nat. Commun.*, 2018, **9**, 2514.
- B. Sun, S. Ranjan, G. Zhou, T. Guo, Y. Xia, L. Wei, Y. N. Zhou and Y. A. Wu, *Mater. Today Adv.*, 2021, **9**, 100125.
- M. A. Zidan, J. P. Strachan and W. D. Lu, *Nat. Electron.*, 2018, **1**, 22–29.
- Y. van de Burgt, A. Melianas, S. T. Keene, G. Malliaras and A. Salleo, *Nat. Electron.*, 2018, **1**, 386–397.
- Z. Wang, L. Wang, M. Nagai, L. Xie, M. Yi and W. Huang, *Adv. Electron. Mater.*, 2017, **3**, 1600510.
- P. Yao, H. Wu, B. Gao, J. Tang, Q. Zhang, W. Zhang, J. J. Yang and H. Qian, *Nature*, 2020, **577**, 641–646.
- S. Choi, J. H. Shin, J. Lee, P. Sheridan and W. D. Lu, *Nano Lett.*, 2017, **17**, 3113–3118.
- Q. Xia and J. J. Yang, *Nat. Mater.*, 2019, **18**, 309–323.
- Z.-H. Tan, R. Yang, K. Terabe, X.-B. Yin, X.-D. Zhang and X. Guo, *Adv. Mater.*, 2016, **28**, 377–384.
- P. Cheng, K. Sun and Y. H. Hu, *Nano Lett.*, 2016, **16**, 572–576.
- B. Sun, T. Guo, G. Zhou, J. Wu, Y. Chen, Y. N. Zhou and Y. A. Wu, *ACS Appl. Bio Mater.*, 2021, **4**, 1976–1985.
- J. H. Yoon, Z. Wang, K. M. Kim, H. Wu, V. Ravichandran, Q. Xia, C. S. Hwang and J. J. Yang, *Nat. Commun.*, 2018, **9**, 1–9.
- Z. Lv, Y. Wang, J. Chen, J. Wang, Y. Zhou and S.-T. Han, *Chem. Rev.*, 2020, **120**, 3941.
- W. Yi, K. K. Tsang, S. K. Lam, X. Bai, J. A. Crowell and E. A. Flores, *Nat. Commun.*, 2018, **9**, 1–10.
- X. Hu, W. Wang, B. Sun, Y. Wang, J. Li and G. Zhou, *J. Phys. Chem. Lett.*, 2021, **12**, 5377–5383.
- B. Sun, G. Zhou, K. Xu, Q. Yu and S. Duan, *ACS Mater. Lett.*, 2020, **2**, 1669–1690.
- M. K. Hota, M. K. Bera, B. Kundu, S. C. Kundu and C. K. Maiti, *Adv. Funct. Mater.*, 2012, **22**, 4493–4499.
- G. Kook, S. Jeong, M. K. Kim, S. Lee, N. Choi and H. J. Lee, *Adv. Mater. Technol.*, 2020, **5**, 1900991.
- C. Zhang, W. B. Ye, K. Zhou, H.-Y. Chen, J.-Q. Yang, G. Ding, X. Chen, Y. Zhou, L. Zhou, F. Li and S.-T. Han, *Adv. Funct. Mater.*, 2019, **29**, 1808783.
- X. He, J. Zhang, W. Wang, W. Xuan, X. Wang, Q. Zhang, C. G. Smith and J. Luo, *ACS Appl. Mater. Interfaces*, 2016, **8**, 10954–10960.
- W. Eerenstein, N. D. Mathur and J. F. Scott, *Nature*, 2006, **442**, 759–765.
- X. Yang, Z. Zhou, T. Nan, Y. Gao, G. M. Yang, M. Liu and N. X. Sun, *J. Mater. Chem. C*, 2016, **4**, 234–243.
- N. A. Spaldin and R. Ramesh, *Nat. Mater.*, 2019, **18**, 203.
- T. Kosub, M. Koppe, R. Hühne, P. Appel, B. Shields, P. Maletinsky, R. Hübner, M. O. Liedke, J. Fassbender, O. G. Schmidt and D. Makarov, *Nat. Commun.*, 2017, **8**, 13985.
- L. W. Martin and R. Ramesh, *Acta Mater.*, 2012, **60**, 2449–2470.
- C. A. F. Vaz, J. Hoffman, C. H. Ahn and R. Ramesh, *Adv. Mater.*, 2010, **22**, 2900–2918.
- M. Bibes and A. Barthélémy, *Nat. Mater.*, 2008, **7**, 425–426.
- X. Lu, Y. Kim, S. Goetze, X. Li, S. Dong, P. Werner, M. Alexe and D. Hesse, *Nano Lett.*, 2011, **11**, 3202–3206.
- J.-H. Lee, P. Murugavel, H. Ryu, D. Lee, J. Y. Jo, J. W. Kim, H. J. Kim, K. H. Kim, Y. Jo, M.-H. Jung, Y. H. Oh, Y.-W. Kim, J.-G. Yoon, J.-S. Chung and T. W. Noh, *Adv. Mater.*, 2006, **18**, 3125–3129.

- 50 T.-J. Park, G. C. Papaefthymiou, A. J. Viescas, A. R. Moodenbaugh and S. S. Wong, *Nano Lett.*, 2007, **7**, 766–772.
- 51 J. Ma, J. Hu, Z. Li and C.-W. Nan, *Adv. Mater.*, 2011, **23**, 1062–1087.
- 52 Y.-H. Chu, L. W. Martin, M. B. Holcomb and R. Ramesh, *Mater. Today*, 2007, **10**, 16–23.
- 53 Y. Wang, D. Gray, D. Berry, J. Gao, M. Li, J. Li and D. Viehland, *Adv. Mater.*, 2011, **23**, 4111–4114.
- 54 C. Israel, N. D. Mathur and J. F. Scott, *Nat. Mater.*, 2008, **7**, 93–94.
- 55 P. Zhao, Z. Zhao, D. Hunter, R. Suchoski, C. Gao, S. Mathews, M. Wuttig and I. Takeuchi, *Appl. Phys. Lett.*, 2009, **94**, 243507.
- 56 H. Greve, E. Woltermann, R. Jahns, S. Marauska, B. Wagner, R. Knöchel, M. Wuttig and E. Quandt, *Appl. Phys. Lett.*, 2010, **97**, 152503.
- 57 L. Zhang, C. M. Leung, S. W. Or and S. L. Ho, *J. Appl. Phys.*, 2013, **114**, 027016.
- 58 A. Hirohata and K. Takanashi, *J. Phys. D: Appl. Phys.*, 2014, **47**, 193001.
- 59 H. Yan, Z. Feng, P. Qin, X. Zhou, H. Guo, X. Wang, H. Chen, X. Zhang, H. Wu, C. Jiang and Z. Liu, *Adv. Mater.*, 2020, **32**, 1905603.
- 60 L. Guo, X. Gu, X. Zhu and X. Sun, *Adv. Mater.*, 2019, **31**, 1805355.
- 61 P. Zheng, B. Sun, Y. Chen, H. Elshekh, T. Yu, S. Mao, S. Zhu, H. Wang, Y. Zhao and Z. Yu, *Appl. Mater. Today*, 2019, **14**, 21–28.
- 62 M. Overby, A. Chernyshov, L. P. Rokhinson, X. Liu and J. K. Furdyna, *Appl. Phys. Lett.*, 2008, **92**, 192501.
- 63 D. Kan, L. Pálová, V. Anbusathaiah, C. J. Cheng, S. Fujino, V. Nagarajan, K. M. Rabe and I. Takeuchi, *Adv. Funct. Mater.*, 2010, **20**, 1108–1115.
- 64 D. Mazumdar, V. Shelke, M. Iliev, S. Jesse, A. Kumar, S. V. Kalinin, A. P. Baddorf and A. Gupta, *Nano Lett.*, 2010, **10**, 2555–2561.
- 65 J.-G. Park, M. D. Le, J. Jeong and S. Lee, *J. Phys.: Condens. Matter*, 2014, **26**, 433202.
- 66 A. Sarkar, A. K. Singh, D. Sarkar, G. G. Khan and K. Mandal, *ACS Sustainable Chem. Eng.*, 2015, **3**, 2254–2263.
- 67 R. Moubah, O. Rousseau, D. Colson, A. Artemenko, M. Maglione and M. Viret, *Adv. Funct. Mater.*, 2012, **22**, 4814–4818.
- 68 M. Shang, C. Zhang, T. Zhang, L. Yuan, L. Ge, H. Yuan and S. Feng, *Appl. Phys. Lett.*, 2013, **102**, 062903.
- 69 R. Nechache, C. V. Cojocar, C. Harnagea, C. Nauenheim, M. Nicklaus, A. Ruediger, F. Rosei and A. Pignolet, *Adv. Funct. Mater.*, 2011, **23**, 1724–1729.
- 70 C. M. Fernández-Posada, A. Castro, J.-M. Kiat, F. Porcher, O. Peña, M. Alguero and H. Amorin, *Nat. Commun.*, 2016, **7**, 12772.
- 71 S. Hong, T. Choi, J. H. Jeon, Y. Kim, H. Lee, H.-Y. Joo, I. Hwang, J.-S. Kim, S.-O. Kang, S. V. Kalinin and B. H. Park, *Adv. Mater.*, 2013, **25**, 2339–2343.
- 72 L. Zhao, Z. Lu, F. Zhang, G. Tian, X. Song, Z. Li, K. Huang, Z. Zhang, M. Qin, S. Wu, X. Lu, M. Zeng, X. Gao, J. Dai and J.-M. Liu, *Sci. Rep.*, 2015, **5**, 9680.
- 73 J. B. Yi, H. Pan, J. Y. Lin, J. Ding, Y. P. Feng, S. Thongmee, T. Liu, H. Gong and L. Wang, *Adv. Mater.*, 2008, **20**, 1170–1174.
- 74 B. Chen, Q. Xu, X. Zhao, X. Zhu, M. Kong and G. Meng, *Adv. Funct. Mater.*, 2010, **20**, 3791–3796.
- 75 T. Shimizu, T. Xie, J. Nishikawa, S. Shingubara, S. Senz and U. Gösele, *Adv. Mater.*, 2007, **19**, 917–920.
- 76 Q. Wei, Y. Fu, G. Zhang, D. Yang, G. Meng and S. Sun, *Nano Energy*, 2019, **55**, 234–259.
- 77 Z. Lu, Z. Fan, P. Li, H. Fan, G. Tian, X. Song, Z. Li, L. Zhao, K. Huang, F. Zhang, Z. Zhang, M. Zeng, X. Gao, J. Feng, J. Wan and J. Liu, *ACS Appl. Mater. Interfaces*, 2016, **8**, 23963–23968.
- 78 L. Feng, S. Yang, Y. Lin, D. Zhang, W. Huang, W. Zhao, Y. Yin, S. Dong and X. Li, *ACS Appl. Mater. Interfaces*, 2015, **7**, 26036–26042.
- 79 D. Meier, M. Maringer, T. Lottermoser, P. Becker, L. Bohatý and M. Fiebig, *Phys. Rev. Lett.*, 2009, **102**, 107202.
- 80 R. Allenspach, M. Stampanoni and A. Bischof, *Phys. Rev. Lett.*, 1990, **65**, 3344.
- 81 A. C. Whalley, M. L. Steigerwald, X. Guo and C. Nuckolls, *J. Am. Chem. Soc.*, 2007, **129**, 12590–12591.
- 82 H. Jeong, D. Kim, D. Xiang and T. Lee, *ACS Nano*, 2017, **11**, 6511–6548.
- 83 J. Jiang, M. Kula, W. Lu and Y. Luo, *Nano Lett.*, 2005, **5**, 1551–1555.
- 84 W. Du, T. Wang, H.-S. Chu, L. Wu, R. Liu, S. Sun, W. K. Phua, L. Wang, N. Tomczak and C. A. Nijhuis, *Nat. Photonics*, 2016, **10**, 274–280.
- 85 P. C. Mondal, U. M. Tefashe and R. L. McCreery, *J. Am. Chem. Soc.*, 2018, **140**, 7239–7247.
- 86 K. Taniguchi, N. Abe, H. Sagayama, S. Ohtani, T. Takenobu, Y. Iwasa and T. Arima, *Phys. Rev. B: Condens. Matter Mater. Phys.*, 2008, **77**, 064408.
- 87 C. G. Duan, W. N. Mei, W. G. Yin, J. Liu, J. R. Hardy, S. Ducharme and P. A. Dowben, *Phys. Rev. B: Condens. Matter Mater. Phys.*, 2004, **69**, 235106.
- 88 C. Xin, Y. Sui, Y. Wang, Y. Wang, X. Wang, Z. Liu, B. Li and X. Liu, *RSC Adv.*, 2015, **5**, 43432–43439.
- 89 L. Li, J. Britson, J. R. Jokisaari, Y. Zhang, C. Adamo, A. Melville, D. G. Schlom, L.-Q. Chen and X. Pan, *Adv. Mater.*, 2016, **28**, 6574–6580.
- 90 Z. Lu, P. Li, J.-G. Wan, Z. Huang, G. Tian, D. Pan, Z. Fan, X. Gao and J.-M. Liu, *ACS Appl. Mater. Interfaces*, 2017, **9**, 27284–27289.
- 91 R. Zhao, N. Ma, J. Qi, Y. K. Mishra, R. Adelung and Y. Yang, *Adv. Electron. Mater.*, 2019, **5**, 1800791.
- 92 Y. H. You, Z. Wu, L. Zhang, Y. Ying, Y. Liu, L. Fei, X. Chen, Y. Jia, Y. Wang, F. Wang, S. Ju, J. Qiao, C.-H. Lam and H. Huang, *Angew. Chem., Int. Ed.*, 2019, **58**, 11779–11784.
- 93 J. Xie, C. Guo, P. Yang, X. Wang, D. Liu and C. M. Li, *Nano Energy*, 2017, **31**, 28–36.
- 94 G. Liu, S. K. Karuturi, H. Chen, D. Wang, J. W. Ager, A. N. Simonov and A. Tricoli, *Sol. Energy*, 2020, **202**, 198–203.



- 95 S. Irfan, Y. Shen, S. Rizwan, H. C. Wang, S. B. Khan and C. W. Nan, *J. Am. Ceram. Soc.*, 2017, **100**, 31–40.
- 96 R. V. K. Mangalam, M. Chakrabarti, D. Sanyal, A. Chakrabati and A. Sundaresan, *J. Phys.: Condens. Matter*, 2009, **21**, 445902.
- 97 L. Bocher, A. Gloter, A. Crassous, V. Garcia, K. March, A. Zobelli, S. Valencia, S. Enouz-Vedrenne, X. Moya, N. D. Marthur, C. Deranlot, S. Fusil, K. Bouzehouane, M. Bibes, A. Barthélémy, C. Colliex and O. Stéphan, *Nano Lett.*, 2012, **12**, 376–382.
- 98 J. Y. Son, J.-H. Lee, S. Song, Y.-H. Shin and H. M. Jang, *ACS Nano*, 2013, **7**, 5522–5529.
- 99 S. Banerjee, A. Datta, A. Bhaumik and D. Chakravorty, *J. Appl. Phys.*, 2011, **110**, 064316.
- 100 N. Sharma, A. Gaur and U. K. Gaur, *Ceram. Int.*, 2014, **40**, 16441–16448.
- 101 Z. Shen, X. Wang, B. Luo and L. Li, *J. Mater. Chem. A*, 2015, **3**, 18146–18153.
- 102 M. Niederberger, N. Pinna, J. Polleux and M. Antonietti, *Angew. Chem., Int. Ed.*, 2004, **43**, 2270–2273.
- 103 C.-F. Chen, G. King, R. M. Dickerson, P. A. Papin, S. Gupta, W. R. Kellogg and G. Wu, *Nano Energy*, 2015, **13**, 423–432.
- 104 L. A. Patil, D. N. Suryawanshi, I. G. Pathan and D. G. Patil, *Sens. Actuators, B*, 2014, **195**, 643–650.
- 105 Z. Wang, J. Lin, R. Wang and K. Wei, *Catal. Commun.*, 2013, **32**, 11–14.
- 106 Z. Yan, Y. Guo, G. Zhang and J.-M. Liu, *Adv. Mater.*, 2011, **23**, 1351–1355.
- 107 N. Jedrecy, V. Jagtap, C. Hebert, L. Becerra, D. Hrabovsky, A. Barbier and X. Portier, *Adv. Electron. Mater.*, 2021, **7**, 2000723.
- 108 P. M. Shafi, N. Joseph, A. Thirumurugan and A. C. Bose, *Chem. Eng. J.*, 2018, **338**, 147–156.
- 109 M. Gibert, M. Viret, A. Torres-Pardo, C. Piamonteze, P. Zubko, N. Jaouen, J.-M. Tonnerre, A. Mougin, J. Fowlie, S. Catalano, A. Gloter, O. Stéphan and J.-M. Triscone, *Nano Lett.*, 2015, **15**, 7355–7736.
- 110 H. Xu, S. Wan, B. Chen, C. Ma, F. Jin, Z. Guo, D. Lan, F. Chen and W. Wu, *Appl. Phys. Lett.*, 2017, **110**, 082402.
- 111 A. B. Shah, Q. M. Ramasse, X. Zhai, J. G. Wen, S. J. May, I. Petrov, A. Bhattacharya, P. Abbamonte, J. N. Eckstein and J.-M. Zuo, *Adv. Mater.*, 2010, **22**, 1156–1160.
- 112 J. Garcia-Barriocanal, J. C. Cezar, F. Y. Bruno, P. Thakur, N. B. Brookes, C. Utfeld, A. Rivera-Calzada, S. R. Giblin, J. W. Taylor, J. A. Duffy, S. B. Dugdale, T. Nakamura, K. Kodama, C. Leon, S. Okamoto and J. Santamaria, *Nat. Commun.*, 2010, **1**, 82.
- 113 J. Garcia-Barriocanal, F. Y. Bruno, A. Rivera-Calzada, Z. Sefrioui, N. M. Nemes, M. Garcia-Hernández, J. Rubio-Zuazo, G. R. Castro, M. Varela, S. J. Pennycook, C. Leon and J. Santamaria, *Adv. Mater.*, 2010, **22**, 627–632.
- 114 Q. Zhang and F. Saito, *J. Alloys Compd.*, 2000, **297**, 99–103.
- 115 S. L. Ye, W. H. Song, J. M. Dai, K. Y. Wang, S. G. Wang, C. L. Zhang, J. J. Du, Y. P. Sun and J. Fang, *J. Magn. Magn. Mater.*, 2002, **248**, 26–33.
- 116 Y. Wang and H. P. Cheng, *J. Phys. Chem. C*, 2013, **117**, 2106–2112.
- 117 X. R. Wang, C. J. Li, W. M. Lü, T. R. Paudel, D. P. Leusink, M. Hoek, N. Poccia, A. Vailionis, T. Venkatesan, J. M. D. Coey, E. Y. Tsymbal, A. Ariando and H. Hilgenkamp, *Science*, 2015, **349**, 716–719.
- 118 J. Zang, G. Zhou, Y. Bai, Z. Quan and X. Xu, *Sci. Rep.*, 2017, **7**, 10557.
- 119 A. Gómez, J. M. Vila-Fungueiriño, R. Moalla, G. Saint-Girons, J. Gázquez, M. Varela, R. Bachelet, M. Gich, F. Rivadulla and A. Carretero-Genevri, *Small*, 2017, **13**, 1701614.
- 120 X. Wang, Z. Wang, Q. Hu, C. Zhang, D. Wang and L. Li, *Solid State Commun.*, 2019, **289**, 22–26.
- 121 H. Ke, H. Zhang, J. Zhou, D. Jia and Y. Zhou, *Ceram. Int.*, 2019, **45**, 8238–8242.
- 122 M. Janousch, G. I. Meijer, U. Staub, B. Delley, S. F. Karg and B. P. Andreasson, *Adv. Mater.*, 2007, **19**, 2232–2235.
- 123 R. Muenstermann, T. Menke, R. Dittmann and R. Waser, *Adv. Mater.*, 2010, **22**, 4819–4822.
- 124 M. Kawasaki, K. Takahashi, T. Maeda, R. Tsuchiya, M. Shinohara, O. Ishiyama, T. Yonezawa, M. Yoshimoto and H. Koinuma, *Science*, 1994, **266**, 1540–1542.
- 125 T. Riste, E. J. Samuelsen, K. T. Otnes and J. Feder, *Solid State Commun.*, 1993, **88**, 901–904.
- 126 A. E. Paladino, *J. Am. Ceram. Soc.*, 1965, **48**, 476–478.
- 127 M. M. McGibbon, N. D. Browning, M. F. Chisholm, A. J. McGibbon, S. J. Pennycook, V. Ravikumar and V. P. Dravid, *Science*, 1994, **266**, 102–104.
- 128 W. Menesklou, H. J. Schreiner, K. H. Härdtl and E. Ivers-Tiffée, *Sens. Actuators, B*, 1999, **59**, 184–189.
- 129 A. Walkenhorst, C. Doughty, X. X. Xi, S. N. Mao, Q. Li, T. Venkatesan and R. Ramesh, *Appl. Phys. Lett.*, 1992, **60**, 1744–1746.
- 130 R. Konta, T. Ishii, H. Kato and A. Kudo, *J. Phys. Chem. B*, 2004, **108**, 8992–8995.
- 131 M. O. Olagunju, X. Poole, P. Blackwelder, M. P. Thomas, B. S. Guiton, D. Shukla, J. L. Cohn, B. Surnar, S. Dhar, E. M. Zahran, L. G. Bachas and M. R. Knecht, *ACS Appl. Nano Mater.*, 2020, **3**, 4904–4912.
- 132 Y. Kim, M. Watanabe, J. Matsuda, J. T. Song, A. Takagaki, A. Staykov and T. Ishihara, *Appl. Catal., B*, 2020, **278**, 119292.
- 133 C. W. Chang and C. Hu, *Chem. Eng. J.*, 2020, **383**, 123116.
- 134 H. Nili, S. Walia, S. Balendhran, D. B. Strukov, M. Bhaskaran and S. Sriram, *Adv. Funct. Mater.*, 2014, **24**, 6741–6750.
- 135 H. Nili, S. Walia, A. E. Kandjani, R. Ramanathan, P. Gutruf, T. Ahmed, S. Balendhran, V. Bansal, D. B. Strukov, O. Kavehei, M. Bhaskaran and S. Sriram, *Adv. Funct. Mater.*, 2015, **25**, 3172–3182.
- 136 Y. L. Chen, J. Wang, C. M. Xiong, R. F. Dou, J. Y. Yang and J. C. Nie, *J. Appl. Phys.*, 2012, **112**, 023703.
- 137 H. Lee, H. Kim, T. N. Van, D.-W. Kim and J. Y. Park, *ACS Appl. Mater. Interfaces*, 2013, **5**, 11668–11672.
- 138 S. Wu, L. Ren, J. Qing, F. Yu, K. Yang, M. Yang, Y. Wang, M. Meng, W. Zhou, X. Zhou and S. Li, *ACS Appl. Mater. Interfaces*, 2014, **6**, 8575–8579.

- 139 D.-H. Kwon, S. Lee, C. S. Kang, Y. S. Choi, S. J. Kang, H. L. Cho, W. Sohn, J. Jo, S.-Y. Lee, K. H. Oh, T. W. Noh, R. A. D. Souza, M. Martin and M. Kim, *Adv. Mater.*, 2019, **31**, 1901322.
- 140 X. Jiang, M. Wei, C. H. Chan, Y. Wang, R. Lai, J. Wang, J. Dai and X. Qiu, *Appl. Phys. Lett.*, 2020, **116**, 102101.
- 141 M. Kamran and M. Anis-ur-Rehman, *J. Alloys Compd.*, 2020, **822**, 153583.
- 142 X. Zhu, Y. Li, H. Zhang, L. Song, H. Zu, Y. Qin, L. Liu, Y. Li and F. Wang, *J. Alloys Compd.*, 2020, **830**, 154578.
- 143 J. Tian, H. Wu, Z. Fan, Y. Zhang, S. J. Pennycook, D. Zheng, Z. Tan, H. Guo, P. Yu, X. Lu, G. Zhou, X. Gao and J.-M. Liu, *Adv. Mater.*, 2019, **31**, 1903679.
- 144 H. Du, C.-L. Jia, A. Koehl, J. Barthel, R. Dittmann and R. Waser, *J. Mayer, Chem. Mater.*, 2017, **29**, 3164–3173.
- 145 L. Yao, S. Inkinen and S. van Dijken, *Nat. Commun.*, 2017, **8**, 14544.
- 146 B. Cui, P. Werner, T. Ma, X. Zhong, Z. Wang, J. M. Taylor, Y. Zhuang and S. S. P. Parkin, *Nat. Commun.*, 2018, **9**, 3055.
- 147 M. S. Saleem, B. Cui, C. Song, Y. Sun, Y. Gu, R. Zhang, M. U. Fayaz, X. Zhou, P. Werner, S. S. P. Parkin and F. Pan, *ACS Appl. Mater. Interfaces*, 2019, **11**, 6581–6588.
- 148 J. Zhang, D. Meng, H. Huang, H. Cai, Q. Huang, J. Wang, Y. Yang, X. Zhai, Z. Fu and Y. Lu, *AIP Adv.*, 2018, **8**, 025322.
- 149 H.-Y. Lo, C.-Y. Yang, G.-M. Huang, C.-Y. Huang, J.-Y. Chen, C.-W. Huang, Y.-H. Chu and W.-W. Wu, *Nano Energy*, 2020, **72**, 104683.
- 150 V. R. Nallagatla, J. Jo, S. K. Acharya, M. Kim and C. U. Jung, *Sci. Rep.*, 2019, **9**, 1188.
- 151 M. Gich, I. Fina, A. Morelli, F. Sánchez, M. Alexe, J. Gázquez, J. Fontcuberta and A. Roig, *Adv. Mater.*, 2014, **26**, 4645–4652.
- 152 Y. Jiang, Q. Mao, T. Ma, X. Liu, Y. Li, S. Ren and J. Sun, *Ceram. Int.*, 2021, **47**, 13884–13894.
- 153 G. M. Santos, I. B. Catellani, I. A. Santos, R. Guo, A. S. Bhalla, J. E. Padilha and L. F. Cótica, *Sci. Rep.*, 2018, **8**, 6420.
- 154 Y. Hamasaki, T. Shimizu, H. Taniguchi, T. Taniyama, S. Yasui and M. Itoh, *Appl. Phys. Lett.*, 2014, **104**, 082906.
- 155 B. N. Rao, S. Yasui, T. Katayama, A. Taguchi, H. Moriwake, Y. Hamasaki and M. Itoh, *J. Mater. Chem. C*, 2020, **8**, 706–714.
- 156 B. N. Rao, S. Yasui, Y. Han, Y. Hamasaki, T. Katayama, T. Shiraishi, T. Kiguchi and M. Itoh, *ACS Appl. Electron. Mater.*, 2020, **2**, 1065–1073.
- 157 M. Kumar, H.-S. Kim, D. Y. Park, M. S. Jeong and J. Kim, *ACS Appl. Mater. Interfaces*, 2018, **10**, 12768–12772.
- 158 A. A. Minnekhanov, A. V. Emelyanov, D. A. Lapkin, K. E. Nikiruy, B. S. Shvetsov, A. A. Nesmelov, V. V. Rylkov, V. A. Demin and V. V. Erokhin, *Sci. Rep.*, 2019, **9**, 10800.
- 159 S. Ge, Y. Wang, Z. Xiang and Y. Cui, *ACS Appl. Mater. Interfaces*, 2018, **10**, 24620–24626.
- 160 S. K. Hwang, J. M. Lee, S. Kim, J. S. Park, H. I. Park, C. W. Ahn, K. J. Lee, T. Lee and S. O. Kim, *Nano Lett.*, 2012, **12**, 2217–2221.
- 161 R.-A. Eichel, *Phys. Chem. Chem. Phys.*, 2011, **13**, 368–384.
- 162 K. Shibuya, R. Dittmann, S. Mi and R. Waser, *Adv. Mater.*, 2010, **22**, 411–414.
- 163 J. J. Yang, M. D. Pickett, X. M. Li, D. A. A. Ohlberg, D. R. Stewart and R. S. Williams, *Nat. Nanotechnol.*, 2008, **3**, 429–433.
- 164 R. Waser, R. Dittmann, G. Staikov and K. Szot, *Adv. Mater.*, 2009, **21**, 2632–2663.
- 165 Z.-T. Xu, K.-J. Jin, L. Gu, Y.-L. Jin, C. Ge, C. Wang, H.-Z. Guo, H.-B. Lu, R.-Q. Zhao and G.-Z. Yang, *Small*, 2012, **8**, 1279–1284.
- 166 B. Meunier, D. Pla, R. Rodriguez-Lamas, M. Boudard, O. Chaix-Pluchery, E. Martinez, N. Chevalier, C. Jiménez, M. Burriel and O. Renault, *ACS Appl. Electron. Mater.*, 2019, **1**, 675–683.
- 167 A. E. Lee, C. E. Platt, J. F. Burch, R. W. Simon, J. P. Goral and M. M. Al-Jassim, *Appl. Phys. Lett.*, 1990, **57**, 2019–2021.
- 168 A. Tebano, E. Fabbri, D. Pergolesi, G. Balestrino and E. Traversa, *ACS Nano*, 2012, **6**, 1278–1283.
- 169 H. Chen, A. M. Kolpak and S. Ismail-Beigi, *Adv. Mater.*, 2010, **22**, 2881–2899.
- 170 C. M. Foster, Z. Li, M. Buckett, D. Miller, P. M. Baldo, L. E. Rehn, G. R. Bai, D. Guo, H. You and K. L. Merkle, *J. Appl. Phys.*, 1995, **78**, 2607–2622.
- 171 Z. Li, S. Zhang and W. E. Lee, *J. Eur. Ceram. Soc.*, 2007, **27**, 3201–3205.
- 172 S. Wu, X. Luo, S. Turner, H. Peng, W. Lin, J. Ding, A. David, B. Wang, G. V. Tendeloo, J. Wang and T. Wu, *Phys. Rev. X*, 2013, **3**, 041027.
- 173 Z. Gao, X. Huang, P. Li, L. Wang, L. Wei, W. Zhang and H. Guo, *Adv. Mater. Interfaces*, 2018, **5**, 1701565.
- 174 S. Gariglio, N. Reyren, A. D. Caviglia and J. M. Triscone, *J. Phys.: Condensed Matter*, 2009, **21**, 164213.
- 175 C. W. Bark, D. A. Felker, Y. Wang, Y. Zhang, H. W. Jang, C. M. Folkman, J. W. Park, S. H. Baek, H. Zhou, D. D. Fong, X. Q. Pan, E. Y. Tsymlal, M. S. Rzechowski and C. B. Eom, *Proc. Natl. Acad. Sci. U. S. A.*, 2011, **108**, 4720–4724.
- 176 A. Joshua, J. Ruhman, S. Pecker, E. Altman and S. Ilani, *Proc. Natl. Acad. Sci. U. S. A.*, 2013, **110**, 9633–9638.
- 177 A. G. Swartz, S. Harashima, Y. Xie, D. Lu, B. Kim, C. Bell, Y. Hikita and H. Y. Hwang, *Appl. Phys. Lett.*, 2014, **105**, 032406.
- 178 A. McCollam, S. Wenderich, M. K. Kruize, V. K. Guduru, H. J. A. Molegraaf, M. Huijben, G. Koster, D. H. A. Blank, G. Rijnders, A. Brinkman, H. Hilgenkamp, U. Zeitler and J. C. Maan, *APL Mater.*, 2014, **2**, 022102.
- 179 T. R. Shrout and S. J. Zhang, *J. Electroceram.*, 2007, **19**, 113–126.
- 180 K.-I. Park, J. H. Son, G.-T. Hwang, C. K. Jeong, J. Ryu, M. Koo, I. Choi, S. H. Lee, M. Byun, Z. L. Wang and K. J. Lee, *Adv. Mater.*, 2014, **26**, 2514–2520.
- 181 T. Furukawa, K. Ishida and E. Fukada, *J. Appl. Phys.*, 1979, **50**, 4904–4912.
- 182 Y. Qi, J. Kim, T. D. Nguyen, B. Lisko, P. K. Purohit and M. C. McAlpine, *Nano Lett.*, 2011, **11**, 1331–1336.
- 183 J. Fukushima, K. Kodaira and T. Matsushita, *J. Mater. Sci.*, 1984, **19**, 595–598.

- 184 Q.-L. Zhao, G.-P. He, J.-J. Di, W.-L. Song, Z.-L. Hou, P.-P. Tan, D.-W. Wang and M.-S. Cao, *ACS Appl. Mater. Interfaces*, 2017, **9**, 24696–24703.
- 185 G.-T. Hwang, V. Annapureddy, J. H. Han, D. J. Joe, C. Baek, D. Y. Park, D. H. Kim, J. H. Park, C. K. Jeong, K.-I. Park, J.-J. Choi, D. K. Kim, J. Ryu and K. J. Lee, *Adv. Energy Mater.*, 2016, **6**, 1600237.
- 186 N. Chamankar, R. Khajavi, A. A. Yousefi, A. Rashidi and F. Golestanifard, *Ceram. Int.*, 2020, **46**, 19669–19681.
- 187 G. Tan, K. Maruyama, Y. Kanamitsu, S. Nishioka, T. Ozaki, T. Umegaki, H. Hida and I. Kanno, *Sci. Rep.*, 2019, **9**, 1–6.
- 188 J. He, X. Guo, J. Yu, S. Qian, X. Hou, M. Cui, Y. Yang, J. Mu, W. Geng and X. Chou, *Nanotechnol.*, 2020, **31**, 155503.
- 189 D. Pantel, S. Goetze, D. Hesse and M. Alexe, *ACS Nano*, 2011, **5**, 6032–6038.
- 190 C. Baeumer, S. P. Rogers, R. Xu, L. W. Martin and M. Shim, *Nano Lett.*, 2013, **13**, 1693–1698.
- 191 W. Dai, Y. Li, C. Jia, C. Kang, M. Li and W. Zhang, *RSC Adv.*, 2020, **10**, 18039–18043.
- 192 L. Jin, H. Zhu, D. Chu, Y. Yang, C. Wang, N. Xie, Z. Huang and J. Liu, *Microelectron. Reliab.*, 2020, **108**, 113638.
- 193 T. You, N. Du, S. Slesazek, T. Mikolajick, G. Li, D. Bürger, I. Skorupa, H. Stöcker, B. Abendroth, A. Beyer, K. Volz, O. G. Schmidt and H. Schmidt, *ACS Appl. Mater. Interfaces*, 2014, **6**, 19758–19765.
- 194 C. Kumari, I. Varun, S. P. Tiwari and A. Dixit, *AIP Adv.*, 2020, **10**, 025110.
- 195 M. J. Han, Y. L. Tang, Y. J. Wang, Y. L. Zhua, J. Y. Ma, W. R. Geng, Y. P. Feng, M. J. Zou, N. B. Zhang and X. L. Ma, *Acta Mater.*, 2020, **187**, 12–18.
- 196 M. J. Sánchez, *Appl. Phys. Lett.*, 2007, **91**, 252101.
- 197 T. Zhang, J. Yin, Y. Xia, W. Zhang and Z. Liu, *J. Appl. Phys.*, 2013, **114**, 134301.
- 198 F. Zhuge, B. Hu, C. He, X. Zhou, Z. Liu and R.-W. Li, *Carbon*, 2011, **49**, 3796–3802.
- 199 J. Jiang, Z. L. Bai, Z. H. Chen, L. He, D. W. Zhang, Q. H. Zhang, J. A. Shi, M. H. Park, J. F. Scott, C. S. Hwang and A. Q. Jiang, *Nat. Mater.*, 2018, **17**, 49–56.
- 200 S. H. Jo and W. Lu, *Nano Lett.*, 2008, **8**, 392–397.
- 201 X. Zhu and W. D. Lu, *ACS Nano*, 2018, **12**, 1242–1249.
- 202 C. Du, W. Ma, T. Chang, P. Sheridan and W. D. Lu, *Adv. Funct. Mater.*, 2015, **25**, 4290–4299.
- 203 S. Boyn, J. Grollier, G. Lecerf, B. Xu, N. Locatelli, S. Fusil, S. Girod, C. Carrétero, K. Garcia, S. Xavier, J. Tomas, L. Bellaiche, M. Bibes, A. Barthélémy, S. Saïghi and V. Garcia, *Nat. Commun.*, 2017, **8**, 14736.
- 204 D. B. Strukov and R. S. Williams, *Proc. Natl. Acad. Sci. U. S. A.*, 2009, **106**, 20155–20158.
- 205 Y. LeCun, Y. Bengio and G. Hinton, *Nature*, 2015, **521**, 436–444.
- 206 L. Liu, W. Xiong, Y. Liu, K. Chen, Z. Xu, Y. Zhou, J. Han, C. Ye, X. Chen, Z. Song and M. Zhu, *Adv. Electron. Mater.*, 2020, **6**, 1901012.
- 207 J. Zhou, N. Liu, L. Zhu, Y. Shi and Q. Wan, *IEEE Electron. Dev. Lett.*, 2014, **36**, 198–200.
- 208 V. R. Nallagatla, J. Kim, K. Lee, S. C. Chae, C. S. Hwang and C. U. Jung, *ACS Appl. Mater. Interfaces*, 2020, **12**, 41740–41748.
- 209 L. Zhou, S. Yang, G. Ding, J. Q. Yang, Y. Ren, S. R. Zhang, J. Y. Mao, Y. Yang, Y. Zhou and S. T. Han, *Nano Energy*, 2019, **58**, 293–303.
- 210 S. Kim, C. Du, P. Sheridan, W. Ma, S. Choi and W. D. Lu, *Nano Lett.*, 2015, **15**, 2203–2211.
- 211 J. Lee, J.-H. Ryu, B. Kim, F. Hussain, C. Mahata, E. Sim, M. Ismail, Y. Abbas, H. Abbas, D. K. Lee, M.-H. Kim, Y. Kim, C. Choi, B.-G. Park and S. Kim, *ACS Appl. Mater. Interfaces*, 2020, **12**, 33908–33916.
- 212 J.-Q. Yang, R. Wang, Z.-P. Wang, Q.-Y. Ma, J.-Y. Mao, Y. Ren, X. Yang, Y. Zhou and S.-T. Han, *Nano Energy*, 2020, **74**, 104828.
- 213 K. Wang, L. Li, R. Zhao, J. Zhao, Z. Zhou, J. Wang, H. Wang, B. Tang, C. Lu, J. Lou, J. Chen and X. Yan, *Adv. Electron. Mater.*, 2020, **6**, 1901342.
- 214 B. Sun, S. Ranjan, G. Zhou, T. Guo, C. Du, L. Wei, Y. N. Zhou and Y. A. Wu, *ACS Appl. Electron. Mater.*, 2021, **3**, 2380–2388.
- 215 J. Wang, F. Qian, S. Huang, Z. Lv, Y. Wang, X. Xing, M. Chen, S.-T. Han and Y. Zhou, *Adv. Intell. Syst.*, 2021, **3**, 2000180.
- 216 G. Zhou, B. Sun, L. Wang, Z. Ren, C. Xu, B. Wu, P. Li, Y. Yao and S. Duan, *Chem. Commun.*, 2019, **55**, 9915–9918.
- 217 W. Huang, X. Xia, C. Zhu, P. Steichen, W. Quan, W. Mao, J. Yang, L. Chu and X. Li, *Nano-Micro Lett.*, 2021, **13**, 85.
- 218 G. Zhou, Z. Ren, L. Wang, J. Wu, B. Sun, A. Zhou, G. Zhang, S. Zheng, S. Duan and Q. Song, *Nano Energy*, 2019, **63**, 103793.
- 219 T. Guo, B. Sun, S. Ranjan, Y. Jiao, L. Wei, Y. N. Zhou and Y. A. Wu, *ACS Appl. Mater. Interfaces*, 2020, **12**, 54243–54265.
- 220 G. Cao, P. Meng, J. Chen, H. Liu, R. Bian, C. Zhu, F. Liu and Z. Liu, *Adv. Funct. Mater.*, 2020, **31**, 2005443.
- 221 M. Zhao, B. Gao, J. Tang, H. Qian and H. Wu, *Appl. Phys. Rev.*, 2020, **7**, 011301.
- 222 J. Torrejon, M. Riou, F. A. Araujo, S. Tsunegi, G. Khalsa, D. Querlioz, P. Bortolotti, V. Cros, K. Yakushiji, A. Fukushima, H. Kubota, S. Yuasa, M. D. Stiles and J. Grollier, *Nature*, 2017, **547**, 428.
- 223 E. Chicca, F. Stefanini, C. Bartolozzi and G. Indiveri, *Proc. IEEE*, 2014, **102**, 1367–1388.
- 224 G. Indiveri and S. C. Liu, *Proc. IEEE*, 2015, **103**, 1379–1397.
- 225 W. Ratcliff II, D. Kan, W. Chen, S. Watson, S. Chi, R. Erwin, G. J. McIntyre, S. C. Capelli and I. Takeuchi, *Adv. Funct. Mater.*, 2011, **21**, 1567–1574.
- 226 J. Wang, J. B. Neaton, H. Zheng, V. Nagarajan, S. B. Ogale, B. Liu, D. Viehland, V. Vaithyanathan, D. G. Schlom, U. V. Waghmare, N. A. Spaldin, K. M. Rabe, M. Wuttig and R. Ramesh, *Science*, 2003, **299**, 1719–1722.
- 227 R. K. Vasudevan, Y.-C. Chen, H.-H. Tai, N. Balke, P. Wu, S. Bhattacharya, L. Q. Chen, Y.-H. Chu, I.-N. Lin, S. V. Kalinin and V. Nagarajan, *ACS Nano*, 2011, **5**, 879–887.
- 228 H. Sun, Z. Luo, L. Zhao, C. Liu, C. Ma, Y. Lin, G. Gao, Z. Chen, Z. Bao, X. Jin, Y. Yin and X. Li, *ACS Appl. Electron. Mater.*, 2020, **2**, 1081–1089.
- 229 C. Li, D. Belkin, Y. Li, P. Yan, M. Hu, N. Ge, H. Jiang, E. Montgomery, P. Lin, Z. Wang, W. Song, J. P. Strachan,



- M. Barnell, Q. Wu, R. S. Williams, J. J. Yang and Q. Xia, *Nat. Commun.*, 2018, **9**, 2385.
- 230 H. Sun, Z. Luo, C. Liu, C. Ma, Z. Wang, Y. Yin and X. Li, *J. Materiomics*, 2021, DOI: 10.1016/j.jmat.2021.04.009.
- 231 Y. Yang, Z. Xi, Y. Dong, C. Zheng, H. Hu, X. Li, Z. Jiang, W.-C. Lu, D. Wu and Z. Wen, *ACS Appl. Mater. Interfaces*, 2020, **12**, 56300–56309.
- 232 J. Rao, Z. Fan, L. Hong, S. Cheng, Q. Huang, J. Zhao, X. Xiang, E.-J. Guo, H. Guo, Z. Hou, Y. Chen, X. Lu, G. Zhou, X. Gao and J.-M. Liu, *Mater. Today Phys.*, 2021, **18**, 100392.
- 233 B. Sun, T. Guo, G. Zhou, S. Ranjan, Y. Jiao, L. Wei, Y. N. Zhou and Y. A. Wu, *Mater. Today Phys.*, 2021, **18**, 100393.
- 234 Y. Zhai, Y. Zhou, X. Yang, F. Wang, W. Ye, X. Zhu, D. She, W. D. Lu and S.-T. Han, *Nano Energy*, 2020, **67**, 104262.
- 235 D. Ielmini and S. Ambrogio, *Nanotechnol.*, 2019, **31**, 092001.
- 236 E. J. Fuller, S. T. Keene, A. Melianas, Z. Wang, S. Agarwal, Y. Li, Y. Tuchman, C. D. James, M. J. Marinella, J. J. Yang, A. Salleo and A. A. Talin, *Science*, 2019, **364**, 570–574.
- 237 C. Bartolozzi, *Science*, 2018, **360**, 966–967.
- 238 P. A. Merolla, J. V. Arthur, B. E. Shi and K. A. Boahen, *IEEE Trans. Circuits Syst.*, 2007, **54**, 301–311.
- 239 F. Walter, F. Röhrbein and A. Knoll, *Neural Networks*, 2015, **72**, 152–167.
- 240 P. Merolla, J. Arthur, R. Alvarez, J. M. Bussat and K. Boahen, *IEEE Trans. Circuits Syst.*, 2013, **61**, 820–833.
- 241 M. Kang, Y. Lee and M. Park, *Electronics*, 2020, **9**, 1069.
- 242 T. F. De Lima, B. J. Shastri, A. N. Tait, M. A. Nahmias and P. R. Prucnal, *Nanophotonics*, 2017, **6**, 577–599.
- 243 B. Liu, Z. Liu, I.-S. Chiu, M. F. Di, Y. R. Wu, J.-C. Wang, T.-H. Hou and C.-S. Lai, *ACS Appl. Mater. Interfaces*, 2018, **10**, 20237–20243.
- 244 B. C. Jang, S. Kim, S. Y. Yang, J. Park, J.-H. Cha, J. Oh, J. Choi, S. G. Im, V. P. Dravid and S.-Y. Choi, *Nano Lett.*, 2019, **19**, 839–849.
- 245 F. Zeng, Y. Guo, W. Hu, Y. Tan, X. Zhang, J. Feng and X. Tang, *ACS Appl. Mater. Interfaces*, 2020, **12**, 23094–23101.
- 246 Y. Pei, Z. Zhou, A. P. Chen, J. Chen and X. Yan, *Nanoscale*, 2020, **12**, 13531–13539.
- 247 K. Lu, Y. Li, W.-F. He, J. Chen, Y.-X. Zhou, N. Duan, M.-M. Jin, W. Gu, K.-H. Xue, H.-J. Sun and X.-S. Miao, *Appl. Phys. A: Mater. Sci. Process.*, 2018, **124**, 438.
- 248 T. Y. Cai, S. C. Liu, S. Ju, C. Y. Liu and G. Y. Guo, *Phys. Rev. Appl.*, 2017, **8**, 034034.
- 249 S. Fusil, V. Garcia, A. Barthélémy and M. Bibes, *Annu. Rev. Mater. Res.*, 2014, **44**, 91–116.
- 250 R. Nechache, C. Harnagea and F. Rosei, *Nanoscale*, 2012, **4**, 5588–5592.
- 251 F. Shao, Z. Ren, C. Lu, Y. Yang, Q. Zhan, Z. Li, J. Chen, Y. Wu, K. Meng, X. Xu, J. Miao and Y. Jiang, *ACS Appl. Nano Mater.*, 2020, **3**, 7516–7523.
- 252 H. Taz, B. Prasad, Y.-L. Huang, Z. Chen, S.-L. Hsu, R. Xu, V. Thakare, T. S. Sakthivel, C. Liu, M. Hettick, R. Mukherjee, S. Seal, L. W. Martin, A. Javey, G. Duscher, R. Ramesh and R. Kalyanaraman, *Sci. Rep.*, 2020, **10**, 1–10.
- 253 M. S. Sheikh, D. Ghosh, T. K. Bhowmik, A. Dutta, S. Bhattacharyya and T. P. Sinha, *Mater. Chem. Phys.*, 2020, **244**, 122685.
- 254 P. Jain, V. Ramachandran, R. J. Clark, H. D. Zhou, B. H. Toby, N. S. Dalal, H. W. Kroto and A. K. Cheetham, *J. Am. Chem. Soc.*, 2009, **131**, 13625–13627.
- 255 H. Singh and J. K. Rajput, *J. Mater. Sci.*, 2018, **53**, 3163–3188.
- 256 Q. Lin, J. Lin, X. Yang, Y. He, L. Wang and J. Dong, *Ceram. Int.*, 2019, **45**, 3333–3340.
- 257 G. He, X. Liu, R. Li, D. Zhai, Y. Liu, C. Xie, P. Hu, Q. Zhen, S. Bashir and J. Liu, *ACS Appl. Mater. Interfaces*, 2020, **12**, 9421–9433.
- 258 X. Li, H. Liu, Z. Chen, Q. Wu, Z. Yu, M. Yang, X. Wang, Z. Cheng, Z. Fu and Y. Lu, *Nat. Commun.*, 2019, **10**, 1–10.
- 259 R. Shen, J. Nie, K. Wang, Y. Xiang and B. Wang, *J. Mater. Sci.: Mater. Electron.*, 2021, **32**, 4196–4204.
- 260 J. Huang, H. Wang, Z. Qi, P. Lu, D. Zhang, B. Zhang, Z. He and H. Wang, *Nano Lett.*, 2021, **21**, 1032–1039.